

INVESTIGATION OF THE NEBULAR  
REMNANTS OF NOVAE

Valério A. R. M. Ribeiro  
Astrophysics Research Institute

A thesis submitted in partial fulfilment of the  
requirements of Liverpool John Moores University  
for the degree of Doctor of Philosophy.

January 2011

# Declaration

The work presented in this thesis was carried out at the Astrophysics Research Institute, Faculty of Science, Liverpool John Moores University. Unless otherwise stated, it is the original work of the author.

While registered as a candidate for the degree of Doctor of Philosophy, for which submission is now made, the author has not been registered as a candidate for any other award. This thesis has not been submitted in whole, or in part, for any other degree.

# Abstract

Classical and recurrent nova outbursts occur on the surface of a white dwarf in a close binary system. It is widely established that the outburst is due to a thermonuclear runaway. Their study provides a real-time laboratory for the understanding of a wide range of astrophysical phenomena. These include for example, mass transfer in close binary systems, nuclear powered outbursts, dust formation, mass loss from red giants, and many others. Recurrent novae have also been suggested as the progenitors of Type Ia Supernovae.

This thesis concentrates on investigating the nebular remnants of novae by studying both resolved imaging (where available) and spectroscopic evolution and combining this with detailed modelling. Such studies have wider implications for example in our understanding of the shaping of proto-Planetary Nebulae.

Here, using a morpho-kinematical code, the true 3D geometry, from which information such as the remnant's inclination angle and expansion velocity can be derived, of the recurrent nova RS Ophiuchi and classical novae V2491 Cygni, V2672 Ophiuchi and KT Eridani are established and related to other characteristics of each system. Each of the classical novae have also been suggested as a recurrent nova candidate. Furthermore, several enhancements to the modelling code were implemented prompted by the work described in this thesis.

The RS Oph work entailed detailed modelling of *Hubble Space Telescope* resolved imaging combined with ground-based spectroscopic observations. Here it was shown that the bipolar morphology of RS Oph consisted of two distinct components with an outer dumbbell and an inner hour glass overdensity, which were required to reproduce both the observed images and spectra. This morphology was suggested to arise due to the interaction between the pre-existing anisotropic red-giant wind and the ejecta. The observed asymmetry in the ACS/HRC image was shown to be due to the finite width and offset from the [O III] line's rest wavelength of the F502N filter. This in turn gave valuable information on the spatial orientation of the nebula. The inclination angle was derived to be

$39_{-10}^{+1}$  degrees, comparable with estimates of the inclination of the central binary. Furthermore, it was also suggested, when comparing two different epochs, that there was evidence for some deceleration of the inner hour glass while the outer dumbbell expanded linearly. This linear expansion is also confirmed with X-ray observations.

In the case of V2491 Cyg, V2672 Oph and KT Eri, no resolved imaging was available primarily due to their distances versus time since outburst. The modelling here concentrated on reproducing the  $H\alpha$  line profile at various outburst epochs to derive their true geometry.

V2491 Cyg, was explored using the first scientific results for the Liverpool Telescope prototype spectrograph. These were best-fit using a morphology with polar blobs and an equatorial ring with an inclination angle of  $80_{-12}^{+3}$  degrees and a maximum expansion velocity of the polar blobs of  $3100_{-100}^{+200}$  km s<sup>-1</sup> and for the equatorial ring of  $2700_{-100}^{+200}$  km s<sup>-1</sup>. Multi-epoch fitting showed that the line profile at later times consisted of a combination of  $H\alpha$  and [N II] emission. Furthermore, the derived inclination implies that eclipses should be observed for which a search is now underway. In addition, the amplitude versus time of decline from maximum relationship, at the inclination derived, may imply a recurrent nova nature of V2491 Cyg.

V2672 Oph's derived nebular morphology was that of polar blobs and an equatorial ring with an underlying prolate structure which seemed to reduce in relative density with time compared to the other components. The inclination of the system was suggested to be  $0\pm 6$  degrees and a maximum expansion velocity  $V_{\text{exp}} = 4800_{-800}^{+900}$  km s<sup>-1</sup>. The morphology found here is incompatible with that expected for a fast nova which may again lend support for a recurrent nova nature of V2672 Oph.

In KT Eri, optical spectroscopy, using a combination of second generation spectrograph on the Liverpool Telescope and those of more established observatories, and X-ray observations were compared to determine that the emergence of the

He II 4686Å line is related to the emergence of the super-soft source (SSS) phase in the X-ray. This could be a useful tool as a trigger for future X-ray observations. The SSS phase is an important phase for observations because it samples the continued extensive nuclear burning on the surface of the white dwarf following outburst. Morpho-kinematical modelling suggested that the morphology of the remnant was that of a dumbbell with a ratio between the major to minor axis of 4:1 with an inclination of  $58_{-7}^{+6}$  degrees and the maximum expansion velocity  $V_{\text{exp}} = 2800 \pm 200 \text{ km s}^{-1}$ .

Future enhancements to the modelling code are suggested. Furthermore, the results given here present sufficient scientific motivation to justify for example a renewed program of *Hubble Space Telescope* observations of nova remnants.

# Publications

## Refereed Journals:

Darnley, M. J., **Ribeiro, V. A. R. M.**, Bode, M. F. & Munari, U. 2010, A&A, submitted – *On the Progenitor System of the Nova V2491 Cygni*

**Ribeiro, V. A. R. M.**, Darnley, M. J., Bode, M. F., Munari, U., Harman, D. J., Steele, I. A., & Meaburn, J. 2010, MNRAS, in press – *The morphology of the expanding ejecta of V2491 Cygni (2008 N.2)*

Munari, U., **Ribeiro, V. A. R. M.**, Bode, M. F., & Saguner, T. 2011, MNRAS, 410, 525 – *Properties, evolution and morpho-kinematical modelling of the fast nova V2672 Oph (Nova Oph 2009), a clone of U Sco*

**Ribeiro, V. A. R. M.**, Bode, M. F., Darnley, M. J., Harman, D. J., Newsam, A. M., O'Brien, T. J., Bohigas, J., Echevarría, J. M., Bond, H. E., Chavushyan, V. H., Costero, R., Coziol, R., Evans, A., Eyres, S. P. S., León-Tavares, J., Richer, M. G., Tovmassian, G., Starrfield, S., & Zharikov, S. V. 2009, ApJ, 703, 1955 – *The Expanding Nebular Remnant of the Recurrent Nova RS Ophiuchi (2006). II. Modeling of Combined Hubble Space Telescope Imaging and Ground-based Spectroscopy*

## Conference Proceedings:

**Ribeiro, V. A. R. M.**, Bode, M. F., Darnley, M. J., Munari, U., & Harman, D. J. 2010, Asymmetric Planetary Nebulae 5, published by Ebrary, Palo Alto, California, USA. A. A. Zijlstra, I. McDonald and E. Lagadec (eds.), in press – *Exploring the Morphology of the Expanding Nebular Remnants of Novae*

**Ribeiro, V. A. R. M.**, Paulo, C. M., Besteiro, A. M. A. R., Geraldès, H., Maphossa, A. M., Nhanonbe, F. A., & Uaissine, A. J. R. 2009, in Valls-Gabaud, D. and Boksenberg, A. eds, Cambridge University Press, in press – *Introducing Astronomy into Mozambican Society*

Harman, D. J., Bode, M. F., Darnley, M. J., O'Brien, T. J., Bond, H. E., Star-

rfield, S., Evans, A., Eyres, S. P. S., **Ribeiro, V. A. R. M.**, & Echevarría, J. M. 2008, in Evans, A., Bode, M. F., O'Brien, T. J., Darnely, M. J. eds, RS Ophiuchi (2006) and the Recurrent Nova Phenomenon, Astronomical Society of the Pacific, 401, 246 – *Hubble Space Telescope Imaging of the Expanding Nebular Remnant of the 2006 Outburst of RS Ophiuchi*

# Acknowledgments

First and foremost I would like to thank my supervisory team, Prof. Mike Bode, Drs. Matt Darnley and Dan Harman for their scientific guidance, encouragement and support throughout these three long years. In the past three years I have also met and forged collaborations which have taught me a lot therefore, I would like to thank Ulisse Munari, Nye Evans, Wolfgang Steffen, Nico Koning, Tim O'Brien and Stewart Eyres in particular.

I would like to thank my fellow students, specially Clare Ivory and Matt Prescott for keeping me down to Earth. However, there are many more people I would like to thank and in the interest of not forgetting anyone, if you read this and are proud then I am thankful to you.

Last but not least I would like to thank my parents, António and Arcénia, and sisters, Ana and Mónica, for their love, support and understanding and my good friends, António Ferreira, Marko Kozarevic, John McKinney, Pedro Russo and Emilio Vergara for their friendship and support. Finally, to Carlos Alberto for introducing me to the stars in Chimoio, Mozambique.

# Contents

Declaration . . . . .	ii
Abstract . . . . .	iii
Publications . . . . .	vi
Acknowledgments . . . . .	viii
<b>Contents</b>	<b>ix</b>
List of Tables . . . . .	xiv
List of Figures . . . . .	xv
<b>1 Introduction</b>	<b>1</b>
1.1 A Brief History of Novae . . . . .	1
1.2 Classical Novae . . . . .	2
1.3 Dwarf Novae . . . . .	3
1.4 Symbiotic Novae . . . . .	4
1.5 Recurrent Novae . . . . .	4
1.6 Light Curves . . . . .	7
1.6.1 Initial rise . . . . .	8
1.6.2 Pre-maximum halt and final rise . . . . .	10

1.6.3	Initial decline and the transition phase . . . . .	10
1.6.4	Final decline and post-nova . . . . .	11
1.6.5	Maximum magnitude-rate of decline relationship . . . . .	11
1.7	Spectral Evolution . . . . .	12
1.7.1	Pre-maximum spectrum . . . . .	15
1.7.2	The principal spectrum . . . . .	15
1.7.3	Diffuse enhanced spectrum . . . . .	17
1.7.4	The Orion spectrum . . . . .	17
1.7.5	The nebular spectrum . . . . .	17
1.8	Nova Remnants . . . . .	17
1.9	This Work . . . . .	23
<b>2</b>	<b>Models of the Ejecta of Novae</b>	<b>25</b>
2.1	Introduction . . . . .	25
2.2	SHAPE . . . . .	27
2.2.1	Using SHAPE . . . . .	28
2.2.2	Rendering and distribution . . . . .	30
2.2.3	1D line profiles . . . . .	31
2.2.4	Testing against early models . . . . .	33
2.2.5	Optimizer module . . . . .	33
2.3	Contributions to SHAPE . . . . .	36
2.3.1	Doppler filter profile . . . . .	36
2.3.2	Other contributions . . . . .	37

2.4	Concluding Remarks . . . . .	37
<b>3</b>	<b>The Expanding Nebular Remnant of the Recurrent Nova RS Ophi- uchi</b>	<b>38</b>
3.1	Introduction . . . . .	38
3.2	Observations and Data Reduction . . . . .	41
3.2.1	Hubble Space Telescope imaging . . . . .	41
3.2.2	Ground-based spectroscopy . . . . .	42
3.2.3	Hubble Space Telescope data reduction . . . . .	43
3.3	Observational Results . . . . .	44
3.3.1	Hubble Space Telescope images . . . . .	44
3.3.2	Ground-based spectroscopy . . . . .	47
3.4	Modelling Procedure . . . . .	51
3.5	Modelling Results . . . . .	55
3.5.1	General structure . . . . .	55
3.5.2	System orientation . . . . .	58
3.5.3	System inclination . . . . .	60
3.5.4	Second epoch <i>HST</i> observations ( $t = 449$ days) . . . . .	61
3.6	Extended X-ray Emission . . . . .	64
3.7	Discussion . . . . .	66
<b>4</b>	<b>The Morphology of the Expanding Ejecta of Nova V2491 Cygni</b>	<b>69</b>
4.1	Introduction . . . . .	69
4.2	Observations and Data Reduction . . . . .	72

4.3	Observational Results . . . . .	75
4.4	Modelling . . . . .	76
4.4.1	Model assumptions . . . . .	81
4.4.2	Model parameters . . . . .	82
4.5	Modelling Results . . . . .	84
4.5.1	Early epoch observations ( $t = 25$ days) . . . . .	84
4.5.2	Later epoch observations ( $t = 108$ days) . . . . .	86
4.6	Discussion and Conclusions . . . . .	94
<b>5</b>	<b>The Morphology of the Expanding Ejecta of Nova V2672 Ophiuchi</b>	<b>97</b>
5.1	Introduction . . . . .	97
5.2	Modelling Procedure . . . . .	100
5.2.1	Initial information . . . . .	100
5.2.2	Modelling . . . . .	100
5.3	Results . . . . .	103
5.4	Discussion . . . . .	107
<b>6</b>	<b>Optical and X-ray Observations and Modelling of Nova KT Eridani</b>	<b>109</b>
6.1	Introduction . . . . .	109
6.2	Observations . . . . .	110
6.3	Observational Results . . . . .	112
6.4	Modelling Procedures . . . . .	124

6.4.1	Previous techniques . . . . .	126
6.4.2	Optimizer module technique . . . . .	126
6.5	Modelling Results . . . . .	126
6.5.1	Early epoch observations ( $t = 42.29$ days) . . . . .	126
6.5.2	Later observations ( $t = 63.13$ days) . . . . .	129
6.6	Discussion . . . . .	129
<b>7</b>	<b>Summary and Future Work</b>	<b>133</b>
7.1	Summary . . . . .	133
7.1.1	RS Ophiuchi . . . . .	134
7.1.2	V2491 Cygni . . . . .	135
7.1.3	V2672 Ophiuchi . . . . .	135
7.1.4	KT Eridani . . . . .	136
7.2	Conclusions . . . . .	136
7.3	Future work . . . . .	137
7.3.1	RS Ophiuchi . . . . .	137
7.3.2	V2672 Ophiuchi . . . . .	138
7.3.3	KT Eridani . . . . .	138
7.3.4	Further user suggestions to enhance SHAPE . . . . .	138
7.3.5	Spatially resolving remnants . . . . .	139
	<b>Bibliography</b>	<b>140</b>

# List of Tables

1.1	Known and candidate recurrent novae . . . . .	6
1.2	Novae speed classes . . . . .	8
1.3	Typical values of the MMRD constants . . . . .	12
3.1	Log of optical spectral observations for RS Oph . . . . .	42
4.1	Log of optical spectral observations for V2491 Cyg. . . . .	73
4.2	Derived radial velocity for each of the 5 components of the H $\alpha$ line in V2491 Cyg (see Figure 4.3 and text for details). . . . .	77
4.3	Derived FWHM velocity for each of the 5 components of the H $\alpha$ line in V2491 Cyg (see Figure 4.3 and text for details). . . . .	78
5.1	Results of Gaussian fitting to observed spectra of V2672 Oph . . . . .	101
5.2	Evolution of the implied density ratios for the different model com- ponents . . . . .	105
6.1	Log of optical spectral observations for KT Eri . . . . .	113
6.2	KT Eri integrated flux for the H $\alpha$ line . . . . .	121

# List of Figures

1.1	Ideal CN light curve . . . . .	9
1.2	Examples of novae of the “Fe II” spectral class . . . . .	13
1.3	Examples of novae of the “He/N” spectral class . . . . .	14
1.4	Hybrid nova LMC 1988 No. 2 . . . . .	16
1.5	DQ Her resolved imaging . . . . .	18
1.6	Definition of the inclination angle . . . . .	20
1.7	HR Del mean Balmer line profiles and computed models . . . . .	21
1.8	Schematic multi-frequency development of a nova outburst . . . . .	22
2.1	SHAPE graphical user interface . . . . .	29
2.2	Synthetic images and line profiles for a simple SHAPE model demonstrating a spherical structure with both volume and surface distributions produced with a <i>particle</i> and <i>mesh</i> rendering. . . . .	32
2.3	Comparison synthetic images and line profiles for a system with equatorial and tropical rings . . . . .	34
2.4	Comparison synthetic images and line profiles for a system with an equatorial ring and polar caps . . . . .	35

3.1	Raw and deconvolved <i>HST</i> images of RS Oph through the F502N filter at 155 and 449 days after outburst . . . . .	46
3.2	RS Oph Spectra on 2006 March 15 . . . . .	48
3.3	RS Oph Spectra on 2006 April 17 and 18 . . . . .	49
3.4	RS Oph Spectra on 2006 May 29 . . . . .	50
3.5	High resolution spectra of RS Oph during 2006 February, March, June and July . . . . .	52
3.6	<i>HST</i> ACS/HRC and WFPC2 F502N narrowband filter profile . . . . .	54
3.7	Dumbbell model spectra with surface distribution . . . . .	56
3.8	RS Oph model structure . . . . .	57
3.9	Best-fit model images and spectra results to the first epoch observation ( $t = 155$ days) . . . . .	59
3.10	$\Delta\mathcal{X}^2$ as a function of inclination angle, comparing the observed spectra with the synthetic spectra . . . . .	62
3.11	Second epoch <i>HST</i> ( $t = 449$ days) and model images comparing the observations with different remnant expansions rates . . . . .	63
3.12	<i>Chandra</i> image overlaid with the second epoch <i>HST</i> image . . . . .	65
3.13	<i>HST</i> WFPC2 raw image . . . . .	67
4.1	Optical light curve for V2491 Cyg from AAVSO data . . . . .	71
4.2	Meaburn spectroscopic observations of V2491 Cyg during days 5–31 after outburst . . . . .	74
4.3	Gaussian components best-fit to the observed $H\alpha$ line profile for V2491 Cyg on day 25 after outburst . . . . .	79
4.4	Spectral evolution of the high resolution $H\alpha$ line profile . . . . .	80

4.5	Remnant morphology as visualised in SHAPE . . . . .	83
4.6	Results of the best-fit model spectrum to the observed spectrum on day 25 after outburst . . . . .	85
4.7	Observed spectrum at 108 days after outburst with Model B line profile as a thin shell . . . . .	87
4.8	Observed spectrum at 108 days after outburst with Model B line profile subtracted . . . . .	88
4.9	Accretion disc synthetic line profiles for optically thin and optically thick emission lines covering a range of inclinations . . . . .	89
4.10	Fit to the observed line profile on day 108 after outburst compared with Model A . . . . .	92
4.11	Fit to the observed line profile on day 477 after outburst compared with Model A . . . . .	93
4.12	Amplitude-rate of decline relationship for classical novae . . . . .	96
5.1	Comparison between the photometric evolutions of V2672 Oph and U Sco . . . . .	99
5.2	Two-dimensional representation of the three-dimensional expand- ing structure of the V2672 Oph remnant . . . . .	102
5.3	Best-fit results of comparison between observed and model spectra	104
5.4	As Figure 5.3 . . . . .	106
6.1	KT Eri SMEI and LT SkyCamT light curve . . . . .	111
6.2	FRODOSpec blue arm spectra of KT Eri . . . . .	114
6.3	FRODOSpec red arm spectra of KT Eri . . . . .	115
6.4	FRODOSpec He II 4686Å enlarged image of KT Eri . . . . .	117

6.5	X-ray data and optical spectral evolution . . . . .	118
6.6	As Figure 6.5 for the region between days 60 and 80 after outburst	120
6.7	Comparison of the ratio of H $\alpha$ components with X-ray data . . .	122
6.8	FRODOSpec H $\alpha$ enlarged image of KT Eri . . . . .	123
6.9	KT Eri’s model structure as visualised in SHAPE . . . . .	125
6.10	KT Eri best-fit model results to the observed spectrum ( $t = 42.29$ days) . . . . .	127
6.11	KT Eri best-fit model results using the Optimizer module for a $1/r$ density distribution ( $t = 42.29$ days) . . . . .	128
6.12	Early epoch KT Eri best-fit model results using the Optimizer module for a $1/r^2$ and constant density distribution ( $t = 42.29$ days)	130
6.13	Later epoch KT Eri best-fit model results using the Optimizer module for a $1/r$ and $1/r^2$ density distribution ( $t = 63.13$ days) . .	131

# Chapter 1

## Introduction

### 1.1 A Brief History of Novae

The name nova originates from the Latin words “*stella nova*” which means *new star*. The Merriam-Webster dictionary defines a nova as a star that suddenly increases its light output tremendously and then fades away to its former obscurity in a few months or years. Novae have been observed as early as the 14th century BC by officials at the imperial Chinese court. However, it wasn’t until the twentieth century that the distinction between novae and supernovae became apparent, due primarily to the poorly known absolute magnitudes and remnants of supernovae (see Duerbeck 2008, for a discussion).

The study of novae provides a real-time laboratory for the understanding of other broader fields of astrophysics. For example, mass transfer in close binaries, nuclear-powered outbursts, mass loss from red giants, the evolution of supernova remnants, shaping of proto-Planetary Nebulae (pPNe) and the progenitors of Type Ia Supernovae (SNe). The latter is a particularly important area of investigation because the progenitors of these systems are not fully understood as to whether they arise from a double degenerate or single degenerate system (see, e.g., Livio 2000).

This Chapter will introduce some of the different classes of novae (Sections 1.2, 1.3 and 1.4) to set the scene for the recurrent nova (RN) phenomenon (Section 1.5), then introduce the canonical nova light curve (Section 1.6) and the spectral evolution (Section 1.7) before talking about nova remnants (Section 1.8) and finally introducing the work in this thesis (Section 1.9).

## 1.2 Classical Novae

Classical nova (CN) outbursts occur on one component of a close binary system. This binarity was first demonstrated by Walker (1954) who discovered that the nova DQ Her was an eclipsing binary. Later Kraft (1964) showed that all CNe almost certainly are in a binary system with a short orbital period.

Classical novae are a subset of Cataclysmic Variables (CVs), which are close binary systems with a late-type main sequence star (the secondary) transferring material via Roche lobe overflow to a companion star (the primary; Crawford & Kraft 1956). The primary is a compact object and in the case of CNe a white dwarf (WD; Gallagher & Starrfield 1978). The mass of the secondary in systems such as these, with a short orbital period  $P_{\text{orb}}$  and a Roche lobe-filling main sequence secondary, can be approximated as follows

$$M_2 / M_{\odot} \simeq 0.065 P_{\text{orb}}^{5/4} (\text{hours}), \quad (1.1)$$

where  $M_2$  is the mass of the secondary and  $M_{\odot}$  the mass of the Sun (Warner 1995b). The primary can have a wide range of masses up to the Chandrasekhar limit, but it is found to be above  $\sim 0.5 M_{\odot}$ . The binarity is evident through its imprint on the ejecta, due to the bipolar wind and/or anisotropic irradiation of the outburst material (e.g., Warner 2008).

The CN binary system is generally accepted to contain a carbon-oxygen (CO) or oxygen-neon (ONe) WD primary and a low mass secondary that has filled its Roche lobe, causing material to flow through the inner Lagrangian point into the

primary's lobe. A thin disc is formed around the WD due to the high angular momentum of the transferred material. Hydrodynamic studies show that this accretion from the secondary results in a growing layer of hydrogen-rich gas on the WD surface (e.g., Starrfield et al. 2008). The mass accretion rate for these systems are from  $\sim 10^{-9} M_{\odot} \text{ yr}^{-1}$  (Cassisi et al. 1998). Mixing can occur between the outer layers of the WD and the accreted hydrogen-rich envelope, allowing enrichment of CO or ONe nuclei to be included in the envelope. As more material is accreted on to the WD surface, the temperature and pressure of the material at the base of the envelope increases. Under degenerate conditions, the beginning of nuclear reactions within the accreted envelope can eventually lead to a thermonuclear runaway (TNR), which can eject some or all of the accreted envelope, including material that has been dredged up from the WD. By definition, a CN has had only one recorded outburst. However, they are thought to recur on timescales of tens of thousands of years (e.g., Yaron et al. 2005).

### 1.3 Dwarf Novae

Another subset of CVs are the Dwarf Novae (DNe). Their outburst is due to the release of gravitational potential energy caused by an increase in the rate of mass transfer through the disc. Dwarf nova outburst amplitudes are generally 2–5 mag with recurrence timescales from around 10 days to tens of years lasting from 2–20 days. Observations of the morphology of DNe light curves show three distinct subtypes; the Z Cam stars show long lasting standstills about 0.7 mag below maximum brightness; the SU UMa stars have occasional superoutbursts; and the U Gem stars are those that do not show any of the behaviour as the previous two systems (Warner 1995a).

## 1.4 Symbiotic Novae

Symbiotic Novae (sNe) are slowly eruptive variables showing simultaneously the absorption line features of a late-type giant and emission lines of H I, He I and other ions with ionization potentials  $> 20$  eV, which transforms to an A or F type continuum with further H I and He I absorption lines, or to pure nebular emission spectra, during eruption (Kenyon 1986). The slow outbursts of sNe appear to be typical of accreting WDs in wide binaries, which implies that the outbursts of CNe are accelerated by the interaction of the expanding WD envelope with its close binary companion (Kenyon & Truran 1983). There is no standard light curve for sNe; each object has its own individual one (Luthardt 1992). The outburst occurs due to the reignition of hydrogen burning on the surface of the WD and the ionisation of the stellar wind of the secondary (Kwok 1997).

There are two types of symbiotic stars; S-type (stellar), which contain normal M giants, and D-type (dusty) which contain heavily dust-reddened Mira variables (Warner 1995a). These two types have  $\dot{M}_{\text{wind}} \sim 10^{-8} - 10^{-7} M_{\odot} \text{ yr}^{-1}$  and  $10^{-6} - 10^{-5} M_{\odot} \text{ yr}^{-1}$ , respectively (Kenyon 1988). Accretion may be via Roche Lobe over flow or Bondi-Hoyle wind accretion (Kenyon 1988; Munari & Whitelock 1989). Kwok (1997) suggests that as the lower mass companion evolves up the asymptotic giant branch, a strong stellar wind develops creating a nebula surrounding the entire binary system. Some of the wind will be accreted by the WD, which reignites to become a hydrogen shell-burning star.

## 1.5 Recurrent Novae

As the name suggests, these are systems which have been observed in outburst more than once. They are not DNe and are more like CNe because the outburst is well understood to be due to a TNR. Therefore, any CN showing a second outburst is reclassified as a RN. However, there has been some observational evidence to support cases of CN which have RN characteristics.

Table 1.1 shows the known RNe and a few candidates. These candidates have only been observed in outburst once, but present tentative evidence for their recurrent nature. These include M31N 2007-12b, V2491 Cyg, V2672 Oph and KT Eri.

M31N 2007-12b has been suggested to be an extragalactic RN from optical and X-ray observations (Bode et al. 2009a). Optical spectroscopy obtained 5 days after outburst showed evidence of very high ejection velocities (FWHM  $H\alpha \simeq 4500 \text{ km s}^{-1}$ ) while X-ray data showed an early Super-Soft Source (SSS) implying  $M_{\text{WD}} \gtrsim 1.3 M_{\odot}$ . Furthermore, a progenitor candidate was found from archival *Hubble Space Telescope* (*HST*) observations with magnitude and colour very similar to the RN RS Oph at quiescence, while the outburst optical spectrum and the SSS behaviour are similar to the RN candidate V2491 Cyg.

V2491 Cyg is only the second CN to present pre-outburst X-ray emission (Ibarra & Kuulkers 2008; Ibarra et al. 2008, 2009). The first was V2487 Oph, which at the time of discovery was not known to be a RN (Hernanz & Sala 2002) and was found in outburst in 1900 after search of the Harvard College Observatory archival photographic collection (Pagnotta et al. 2009). V2672 Oph shows very similar photometric behaviour to the RN U Sco (Munari et al. 2011a). KT Eri has been suggested to present optical spectral similarities to the RN LMC 2009a (Bode et al. 2010). These systems will be discussed in greater detail in Chapters 4, 5 and 6, respectively.

Considering only the Galactic RNe in Table 1.1 (although some extragalactic objects have been included for completeness) these appear to fall into two groups:

- Those with long period binaries (V3890 Sgr, V745 Sco, RS Oph and T CrB). These systems have orbital periods of several hundred days, and contain a red giant secondary, similar to sNe (Anupama 2002). The systems in this group have very similar behaviour, both in outburst and at quiescence. They have a high frequency of eruption attributed to the high rate of mass transfer  $\dot{M}$  associated with the giant secondary (Warner 2008).

Table 1.1: Known and candidate recurrent novae. Those with only one recorded outburst are the candidate RNe and details are given in the text.

Name	Secondary	$P_{\text{orb}}$ (days)	Years of outburst	Ref
V3890 Sgr	M5 III	519.7	1962, 1990	1, 8
V745 Sco	M6 III	510	1937, 1989	1, 8
RS Oph	M2 III	455.72	1898, 1907, 1933, 1945, 1958, 1967, 1985, 2006	1, 2, 8
T CrB	M3 III	227.67	1866, 1946	1, 2, 8
U Sco	K2 IV	1.2305	1863, 1906, 1917, 1936, 1945, 1969, 1979, 1987, 1999, 2010	2, 3, 8, 9
LMC 2009#1		1.19	1971, 2009	14, 15
V394 CrA	K	0.7577	1949, 1987	4, 8
CI Aql	K-M IV	0.6184	1917, 1941, 2000	5, 6, 8
IM Nor		0.102	1920, 2002	2, 8
T Pyx		0.0762	1890, 1902, 1920, 1944, 1967	2, 8
V2487 Oph			1900, 1998	12
LMC 1990#2			1968, 1990	13
M31N 2007-12b	M III		2007	7
V2491 Cyg			2008	10
KT Eri			2009	16
V2672 Oph			2009	11

References: 1. Anupama & Mikołajewska (1999); 2. Warner (2008); 3. Anupama & Dewangan (2000); 4. Warner (1995a); 5. Kiss et al. (2001); 6. Mennickent & Honeycutt (1995); 7. Bode et al. (2009a); 8. Schaefer (2010); 9. Schaefer et al. (2010); 10. Nakano et al. (2008); 11. Nakano et al. (2009), 12. Pagnotta et al. (2009); 13. Shore et al. (1991); 14. Liller (2009), 15. Bode et al. (2009b), 16. Bode et al. (2010).

They are fast novae with a rate of decline of  $\sim 0.3$  mag/day (Anupama & Miłojewska 1999). The outburst spectrum has broad emission lines ( $v_{\text{exp}} \sim 4000$  km s $^{-1}$ ), which narrow with time, with the presence of intense coronal lines and other high excitation lines (Anupama & Miłojewska 1999).

- Those with short period binaries (U Sco, V394 CrA, T Pyx, CI Aql and IM Nor). They consist of an evolved main sequence or subgiant secondary and are similar to the CNe systems. The outburst and quiescent properties of U Sco and V394 CrA are very similar. In quiescence their spectra are dominated by He lines unlike normal novae (Warner 2008), while the outburst properties of T Pyx, CI Aql and IM Nor are similar (Anupama 2002). Some of these are among the fastest novae (U Sco and V394 CrA) which makes it possible that some of their previous outbursts went undetected. T Pyx also can be in a class of its own, with a slow decay ( $t_3 = 88$  days), showing oscillations in the transition region. T Pyx has an extremely large quiescent luminosity and it has been suggested that it is in a rapid and possibly terminal phase of evolution. It will end up either with an evaporation of the secondary or as a Type Ia SN if the WD reaches the Chandrasekhar mass (Knigge et al. 2000).

The much shorter inter-outburst period for RNe compared to CNe is predicted to be due to a combination of high WD mass and a high accretion rate (Starrfield et al. 1985; Yaron et al. 2005). These models lead to the ejection of smaller amounts of material at higher velocities than those for CNe (typically  $10^{-8}$  to  $10^{-6}$   $M_{\odot}$  and several thousand km s $^{-1}$ , respectively, for RNe).

## 1.6 Light Curves

Figure 1.1 shows an idealised CN light curve (McLaughlin 1939, 1960), from the initial rise to the final decline. The initial rise is quite fast, so often only when the

Table 1.2: Classification of nova light curves according to speed class.

Speed Class	$t_2$ (days)	$\dot{m}_V$ (mag day <sup>-1</sup> )
Very Fast	<10	>0.20
Fast	11-25	0.18-0.08
Moderately fast	26-80	0.07-0.025
Slow	81-150	0.024-0.013
Very slow	151-250	0.013-0.008

CN is near or at maximum is it observed. Payne-Gaposchkin (1957) introduced the concept of speed classes, listed in Table 1.2, which reflect the rate of decline from maximum light. The notation  $t_n$  is used to show the number of days,  $t$ , that a nova takes to fall by  $n$  magnitudes.

The light curve evolution of Figure 1.1 can be divided into different stages: initial rise, pre-maximum halt and final rise, initial decline and transition, and final decline and post-nova.

### 1.6.1 Initial rise

Detailed observations in this phase are rare due to the unpredictable nature of nova outbursts. Here the nova increases in brightness to within 2 magnitudes from maximum. This initial rise can take from 1–2 days in the fast CNe to several weeks in the slowest CNe.

However, instruments like the Solar Mass Ejection Imager (SMEI) on board the *Coriolis* satellite, which scans most of the sky every 102 minute orbit (Hick et al. 2007), detection and detailed observations of the initial rise have been made as demonstrated by Hounsell et al. (2010) for a sample of three CNe, KT Eri, V598 Pup and V1280 Sco, and one RN, RS Oph.

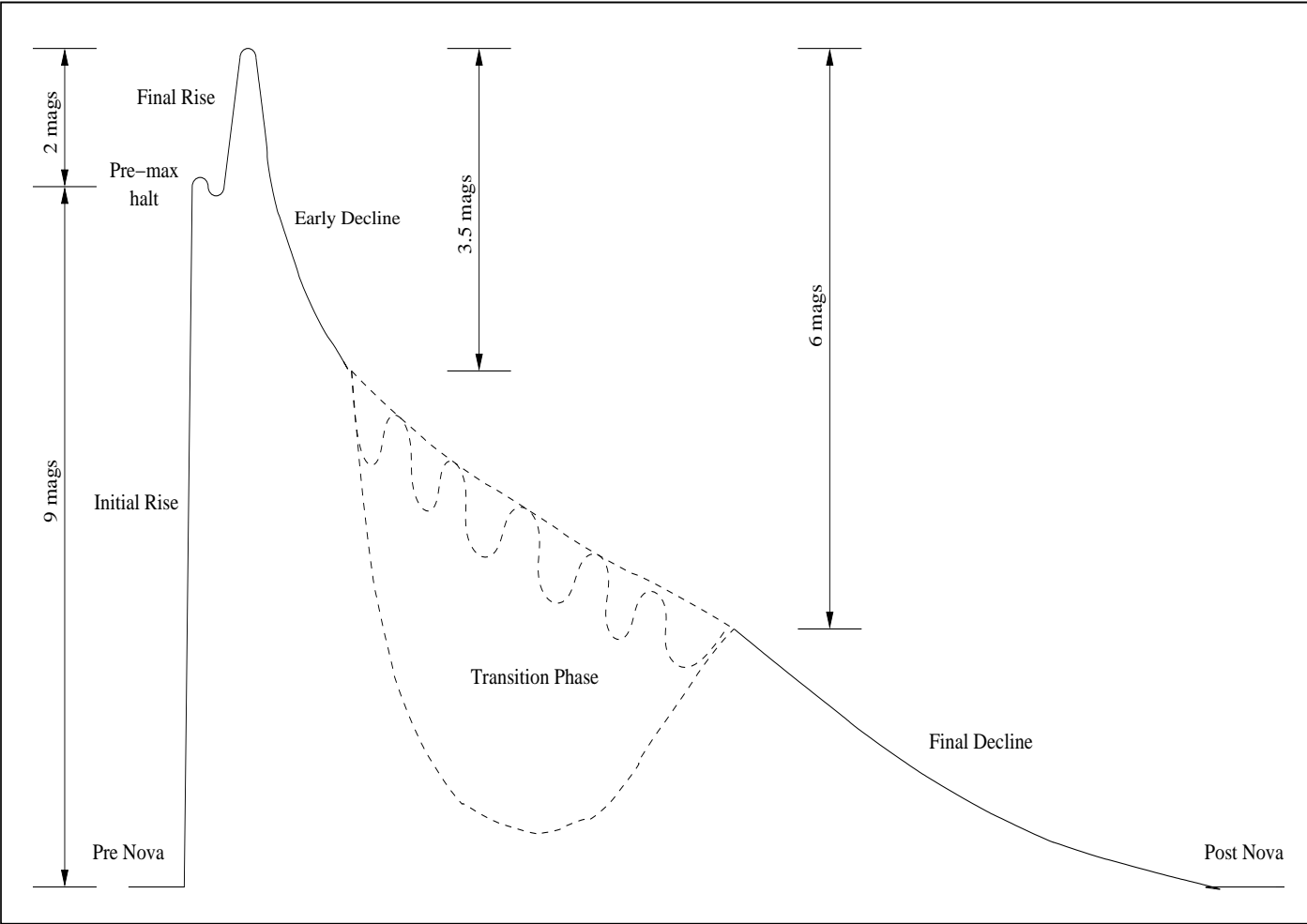


Figure 1.1: The idealised CN light curve (McLaughlin 1939, 1960).

### 1.6.2 Pre-maximum halt and final rise

Some CNe present a pause in the light curve after the initial rise, about 2 magnitudes below maximum (e.g., HR Del). This pause can be of a matter of hours in the fast CNe to a few days in the slowest. The CNe then brighten to maximum, taking 1–2 days for the fast CNe and several weeks for the slower CNe. The nova will remain at or around maximum brightness for only a few hours for the fast CNe and a few days for the slow CNe. Recent results by Hounsell et al. (2010) have sampled well the region of the pre-maximum halt for a few novae determining the duration of the halt. Notably for the RN RS Oph SMEI data were combined with those from the 2m robotic Liverpool Telescope (LT; Steele et al. 2004), using the SkyCamT providing two important photometric points to confirm the halt.

### 1.6.3 Initial decline and the transition phase

The initial decline from maximum brightness is often smooth. However, there are some exceptions to this (e.g., V705 Cas, DQ Her and GK Per). Slow CNe sometimes exhibit irregular light curves with variations in the brightness on time scales of 1–20 days with amplitudes of up to two magnitudes.

Between 3–4 magnitudes below maximum brightness CNe enter the transition phase, which can show different types behaviour:

- Some CNe fall into a minimum 7–10 magnitudes deep and lasting for months or even years (e.g., DQ Her, T Aur, LW Ser). Following this the CN will again brighten and then follow the normal decline. This minimum is observed due to the formation of dust in the gas ejected by the eruption (e.g., Hyland & Neugebauer 1970).
- Others start an oscillation within the transition phase, which can have an amplitude of 1.5 magnitudes. The reason for this happening is not yet

known (e.g., GK Per and V603 Aql).

- And most fast novae just go through this stage without any noticeable difference on the shape of the light curve (e.g., CP Pup, V1500 Cyg, V1668 Cyg).

#### 1.6.4 Final decline and post-nova

After the transition phase, the CN light curve shows a steady decline in brightness with small fluctuations. On the approach to the post-nova stage, the photometric and spectroscopic properties of the post-nova emerge.

#### 1.6.5 Maximum magnitude-rate of decline relationship

By studying CNe in M31, Hubble (1929) noticed that the brighter CNe (at maximum light) fade faster. Since all these lie approximately at the same distance the observations suggested a relationship between a nova speed class and its maximum magnitude. This correlation was later confirmed by McLaughlin (1945), who used absolute magnitudes derived from expansion parallaxes, interstellar line strengths and Galactic rotation, for Galactic CNe. This correlation, the Maximum Magnitude-Rate of Decline (MMRD), can be used as a distance indicator. The general form of the MMRD relationship is expressed as

$$M_\lambda = b_n \log t_n + a_n, \quad (1.2)$$

where  $M_\lambda$  is the absolute magnitude at a given waveband (e.g.,  $M_V$  for visual), and  $t_n$  is the time taken for the nova to decline by  $n$  magnitudes from maximum, typically  $n = 2$  or  $3$ . Typical values of  $a_n$  and  $b_n$  are given in Table 1.3.

Downes & Duerbeck (2000) showed that a linear relationship suffices to model the Galactic MMRD. They also derived a scatter of  $\sim 0.6$  mags.

Table 1.3: Typical values of MMRD constants

$M_\lambda$	$n$	$a_n$	$b_n$	Reference
V	2	$-10.70(\pm 0.30)$	$2.41(\pm 0.23)$	1
V	2	$-11.32(\pm 0.44)$	$2.55(\pm 0.32)$	2
V	3	$-11.99(\pm 0.56)$	$2.54(\pm 0.35)$	2

References: 1. Cohen (1985); 2. Downes & Duerbeck (2000).

## 1.7 Spectral Evolution

The emitted spectrum of novae following outburst is dictated by the evolution of the photosphere, wind, and surface nuclear reactions, which are all related (Williams 1992). These cause the excitation level of novae to be low initially, then increasing to the point where coronal emission lines can be observed, and then decreasing to low levels again (Williams 1990).

The optical spectra of novae show very strong Balmer emission lines. Therefore, classifying the spectral characteristics is best done with the non-Balmer emission lines. Williams (1992) classified the spectra of novae into two broad groups according to which of the non-Balmer emission lines are strongest within the interval 3500–7500 Å after the first few days following outburst. The group can be broadly classed as either “Fe II” or “He/N”.

The “Fe II” spectral class frequently present pronounced P Cyg absorption features in the Balmer and Fe II emission lines. The spectra develop more slowly, over timescales of weeks, and the emission lines tend to be narrower than in “He/N” novae. Furthermore, this group exhibits low ionisation transitions in the earliest phases of the spectral evolution (Figure 1.2). The first forbidden lines to appear are those of auroral transitions and low ionisation lines (Williams 1992).

In the “He/N” spectral class the strongest non-Balmer emission lines are almost always either He II 4686 Å, He I 5876 Å, N II 5679 Å or 5001 Å, or N III 4640 Å. The excitation levels are higher than the “Fe II” spectra and the line profiles are usually broader, with HWZI extending beyond 5000 km s<sup>-1</sup>. Usually the line intensity of He II 4686 Å becomes stronger than H $\beta$  (Figure 1.3, Williams 1992).

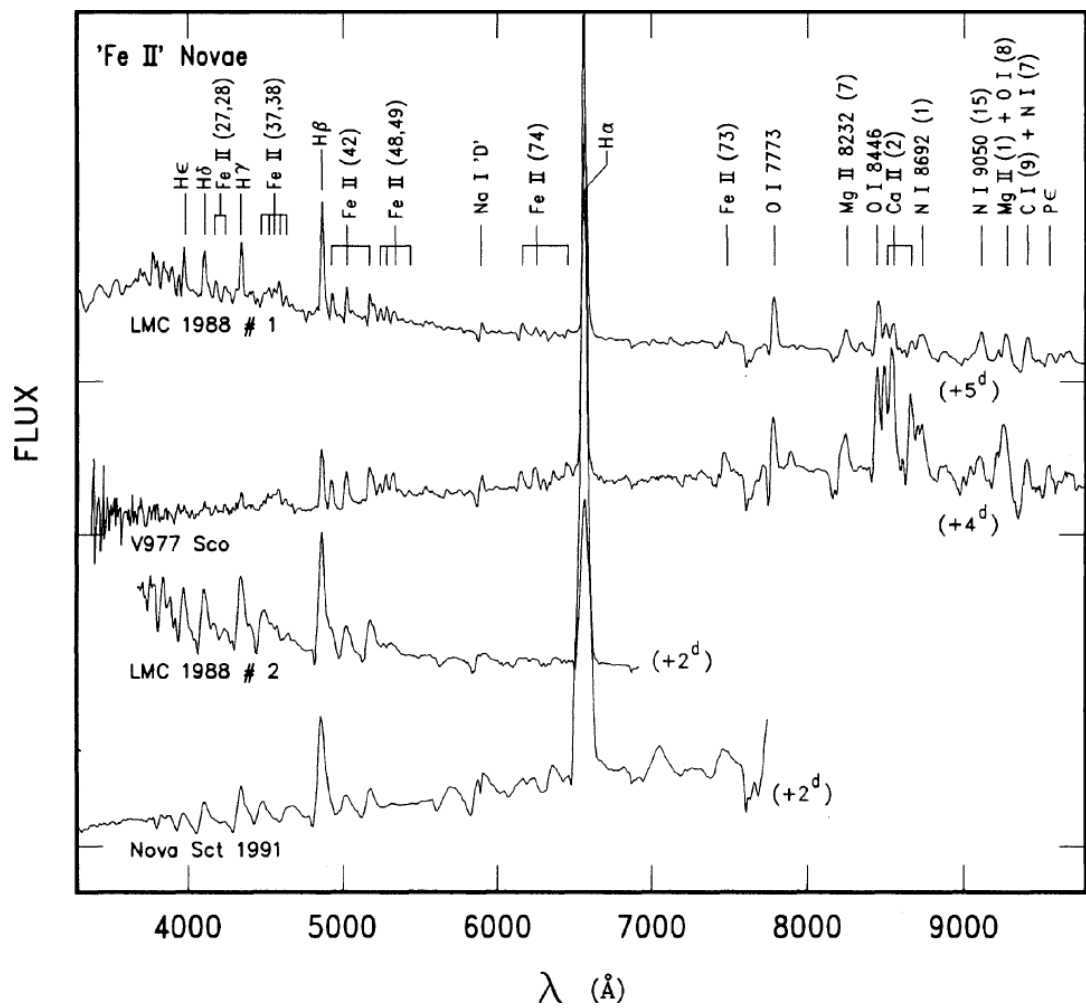


Figure 1.2: Example novae of the “Fe II” spectral class (from Williams 1992).



However, there are a few novae that present a hybrid character. Here the spectrum early after outburst evolves from a “Fe II” class to a “He/N” class before forbidden lines appear. However, some also show simultaneous emission from both classes (Figure 1.4, Williams 1992).

Discussed next is how the spectrum varies as the nova evolves during outburst all the way to the nebular stage.

### 1.7.1 Pre-maximum spectrum

There are few spectra available during the fast rise to maximum light. However, the pre-maximum halt and final rise (Figure 1.1) can provide good opportunities to observe the spectra. Here the spectra are of those of an optically thick expanding, cooling shell, with blueshifted broad absorption lines with occasionally a P Cyg emission component (McLaughlin 1960).

### 1.7.2 The principal spectrum

This appears at visual maximum with stronger and more blueshifted absorption lines than those of the pre-maximum spectrum. This strength resembles lines from A or F supergiant spectrum with enhanced CNO lines (Warner 1995a). The mean velocity of the absorption lines is related to the speed class. McLaughlin (1960) found that these can be represented by

$$\log v_{\text{prin}}(\text{km s}^{-1}) = 3.70 - 0.5 \log t_3(\text{d}) = 3.57 - 0.5 \log t_2(\text{d}). \quad (1.3)$$

P Cyg profiles that develop at or immediately after maximum brightness, with H I, Ca II, Na I and Fe II in the V band (Warner 1995a).

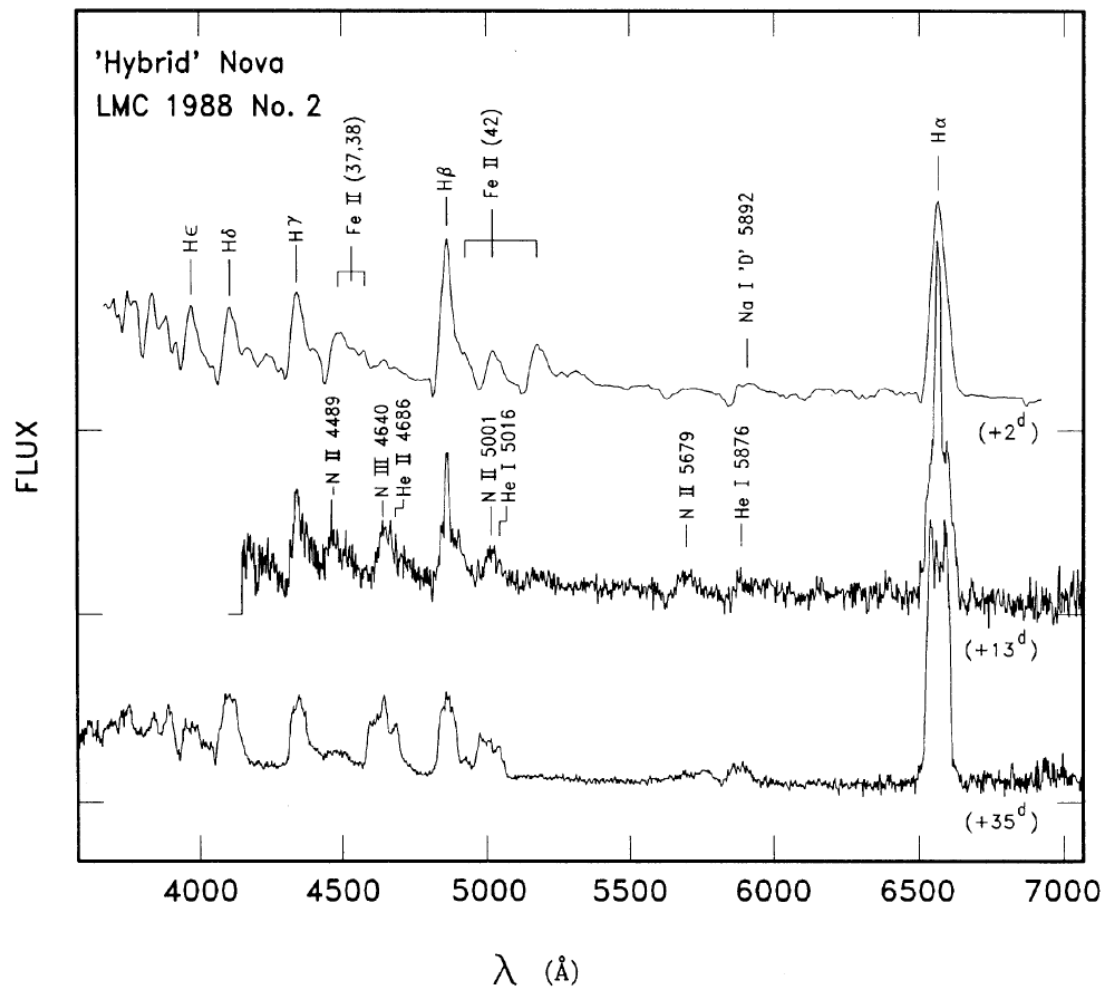


Figure 1.4: Spectral evolution of the hybrid nova LMC 1988 No. 2 (from Williams 1992).

### 1.7.3 Diffuse enhanced spectrum

In this phase the lines are broader than the principal spectrum and the peaks are blueshifted by about twice that of the principal spectrum. Expansion velocities derived are also related to the speed classes (McLaughlin 1960)

$$\log v_{de}(\text{km s}^{-1}) = 3.81 - 0.41 \log t_3(\text{d}) = 3.71 - 0.4 \log t_2(\text{d}). \quad (1.4)$$

P Cyg profiles are common here too but wider than in the principal spectrum.

### 1.7.4 The Orion spectrum

This appears 1–2 mag down from maximum light, displaced blueward by at least as much as the diffuse enhanced system and at first consists predominantly of He I, C II, [N II] and [O II] (H I line not always seen), then with [N III] and [N V] emissions, reaching its maximum strength at about the same time as the diffuse enhanced spectrum disappears (McLaughlin 1960).

### 1.7.5 The nebular spectrum

Here the [O I] and [N II] components of the principal spectrum are retained and then producing [O III] and [Ne III], strengthening relative to the H I, He I, He II, [N II], [N III] emission lines, evolving towards the spectrum of a PN.

## 1.8 Nova Remnants

A nova explosion ejects material at velocities of hundreds to thousands of kilometers per second. This is the material ultimately observed as an expanding shell around the nova (see, e.g., Figure 1.5). The observation and modelling of nova remnants are important for several reasons. For example, such results can be

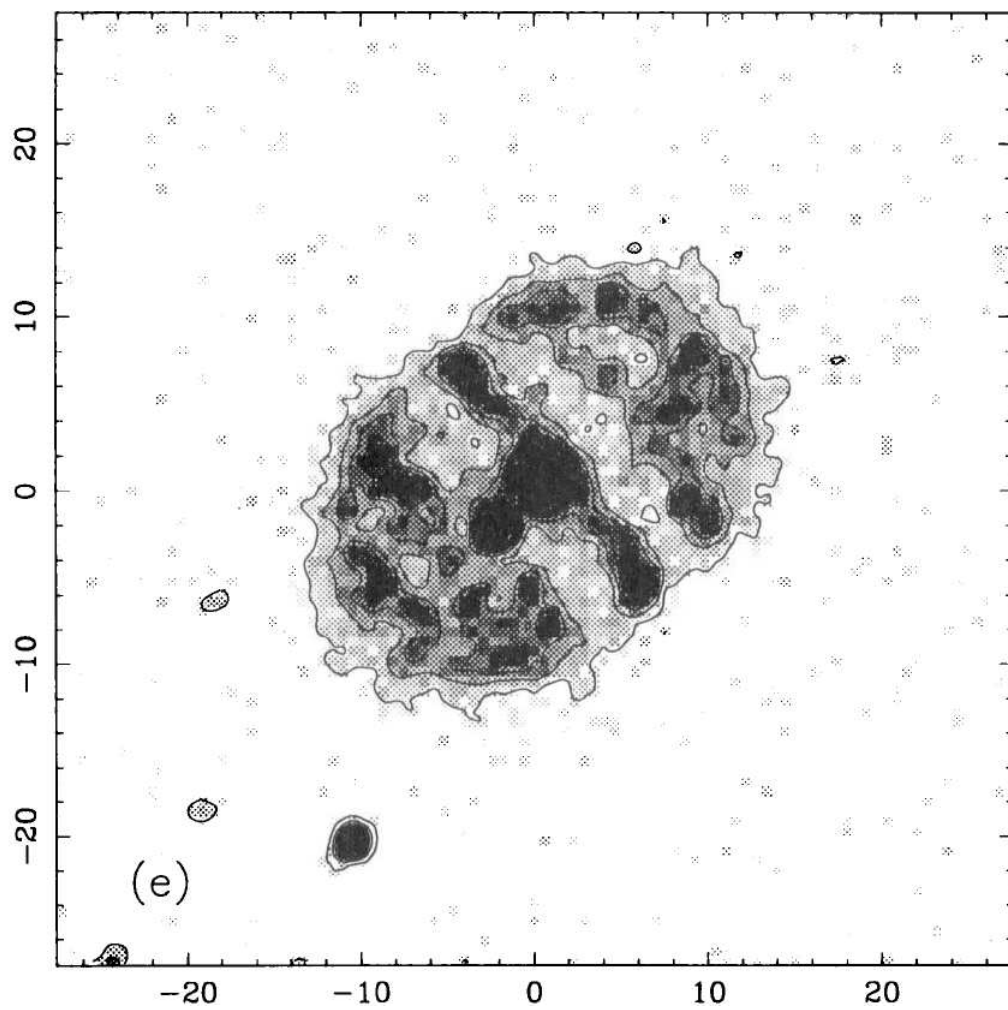


Figure 1.5: William Herschel Telescope [N II] rest-frame image of the resolved remnant of the CN DQ Her. The contour levels are set from the  $2\sigma$  level above the background brightness and then at  $3\sigma$  intervals. Up is north and east to the left. The axis labels are in arcsec (from Slavin et al. 1995).

used to infer the inclination angle,  $i$ , between the plane of the sky and the central binary orbital plane (so that for an inclination of  $90^\circ$  the system would be eclipsing – Figure 1.6). Furthermore, it can be used to determine the distance to the system using the expansion parallax method which allows for greater certainty than any other distance measurement technique. Determining the distance has important consequences for example for the derived energetics and ejected mass of the system.

Spectroscopy of spatially unresolved remnants has long been known to show evidence of organised structure (e.g., Hutchings 1972b). This allows for models of remnant geometry to be formulated and the existence of structure, such as equatorial and tropical rings and polar caps/blobs, to be inferred (see Figure 1.7; Bode 2002).

However, observations of resolved remnants are ultimately most useful to determine the physical characteristics and to gain insight into shaping mechanisms for nova remnants. To determine the angular size of an expanding nova remnant, it follows

$$\theta_r(t) = 0''.207 \left( \frac{v_{exp}}{10^3 \text{ km s}^{-1}} \right) \left( \frac{d}{\text{kpc}} \right)^{-1} (t - t_0), \quad (1.5)$$

where  $(t - t_0)$  is the time lapsed in years,  $d$  the distance and  $v_{exp}$  is the expansion velocity (Warner 1995a). Figure 1.8 shows the broad band spectral evolution of a typical nova and compares when this would become resolved with various telescopes.

Exploring the resolved remnants has also the added benefit that, if taken over two different epochs, the expansion parallax can be used to determine the distance to the nova, with consequences for exploring the MMRD and further understanding of the development of the nova remnant.

The shaping of the ejected material can happen due to several factors. These can be identified as that associated with the common-envelope phase during outburst, the presence of a magnetised WD, the spin of the WD and an asymmetric TNR (see, e.g., O’Brien & Bode 2008). The most widely accepted model involves

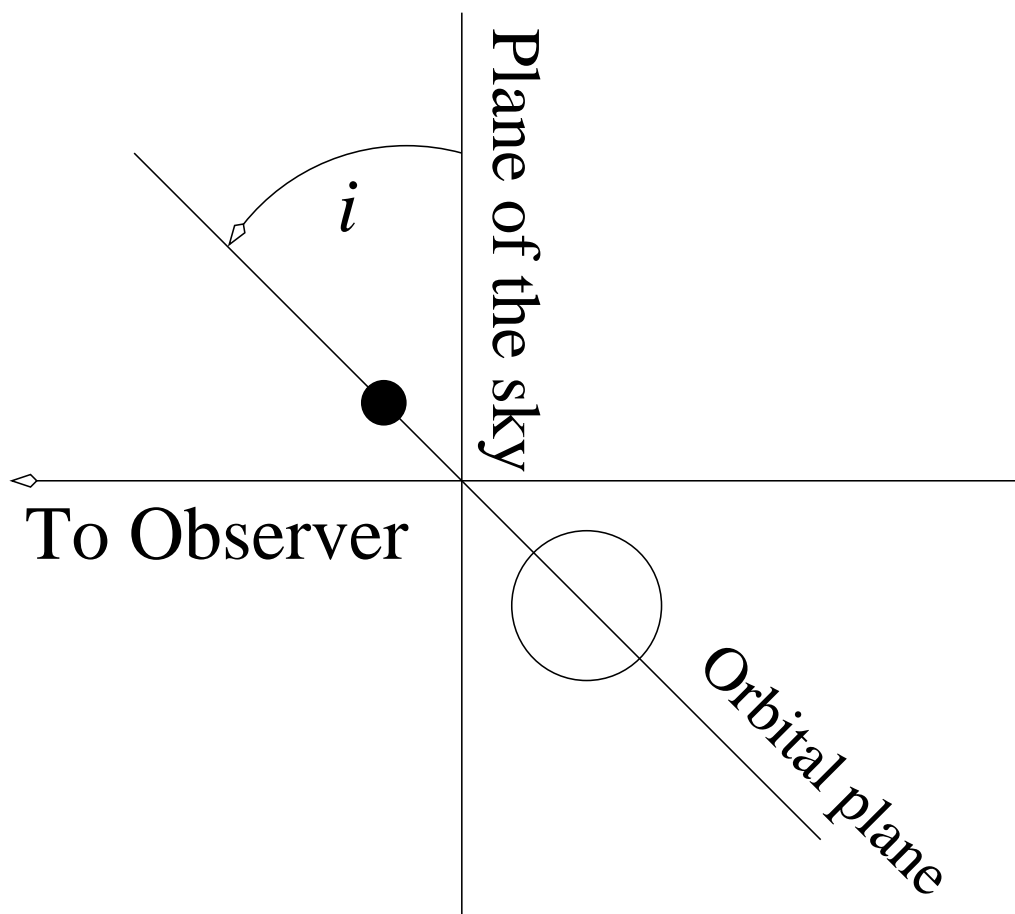


Figure 1.6: The inclination of the system,  $i$ , is defined as the angle between the plane of the sky and the central binary system's orbital plane.

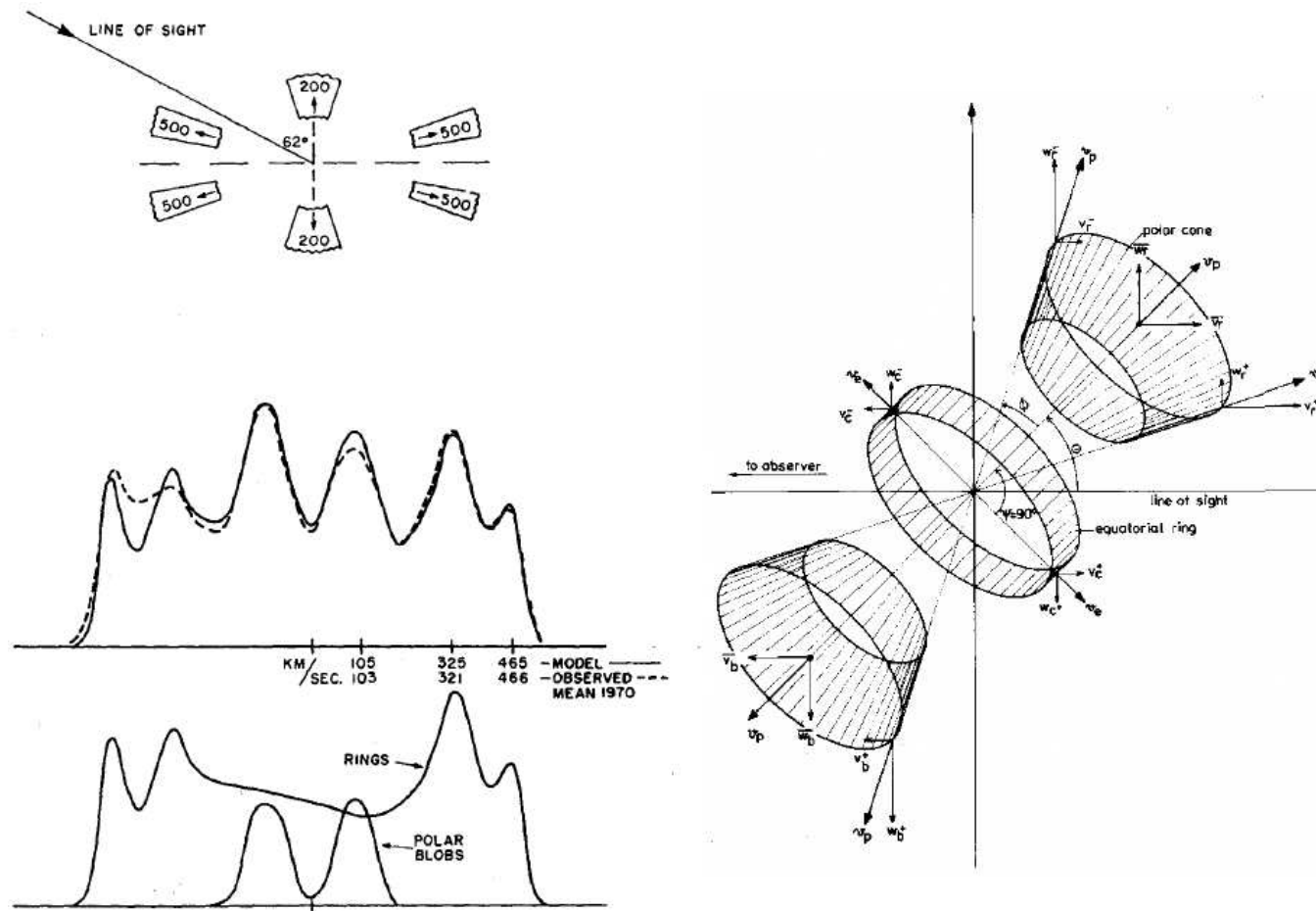


Figure 1.7: Mean Balmer line profiles in 1970 and computed model (left) for HR Del (from Hutchings 1972b) and model geometry of the same ejecta from high resolution spectroscopy 14-15 years after outburst (right; from Solf 1983). The line profile on the middle left show on the x-axis the velocity of the expanding components, where the 2 rings have maximum velocity of  $500 \text{ km s}^{-1}$  and the polar blobs  $200 \text{ km s}^{-1}$ .

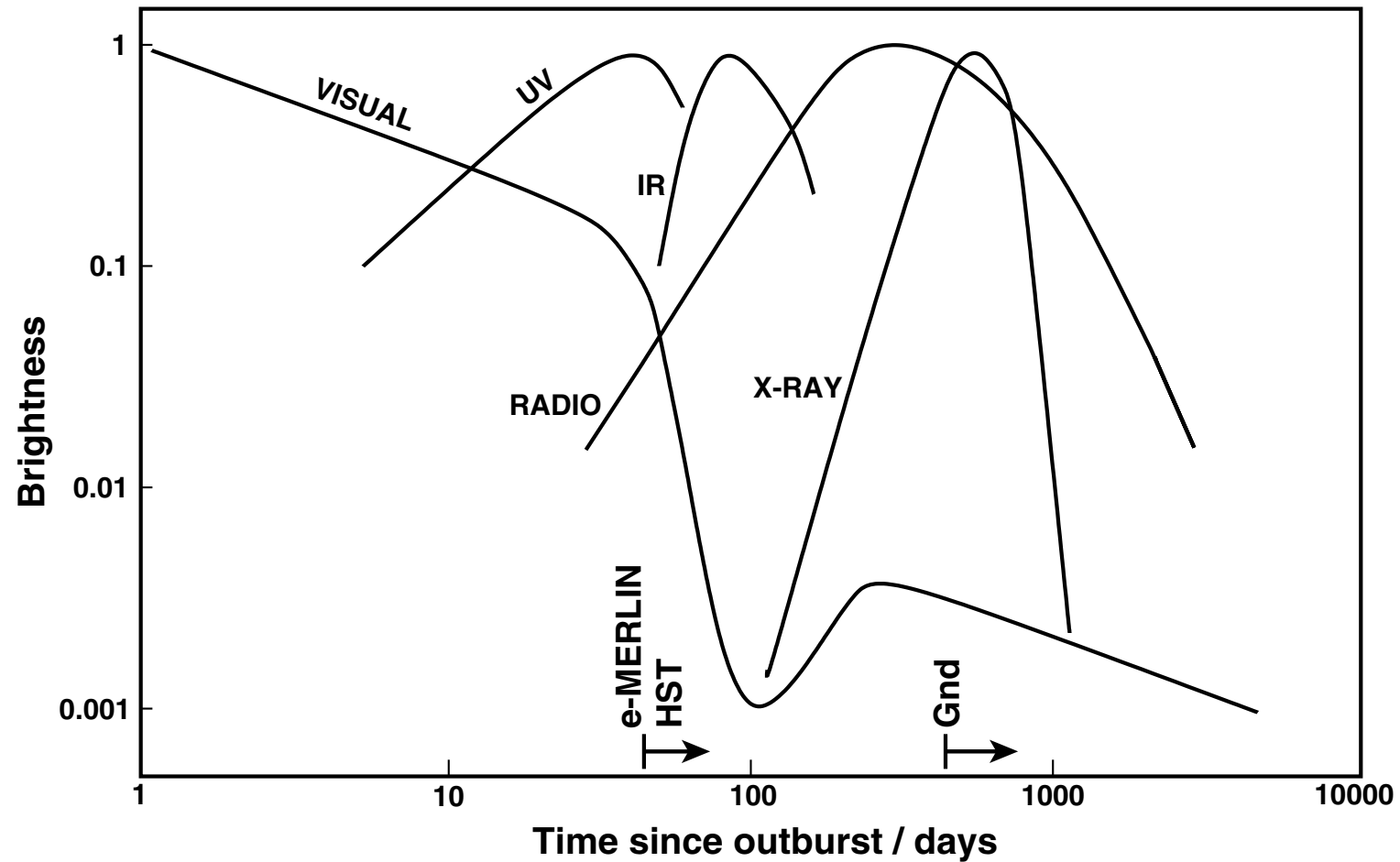


Figure 1.8: Schematic multi-frequency development of a nova outburst with times at which a remnant with expansion velocity of  $1000 \text{ km s}^{-1}$  and distance  $1 \text{ kpc}$  becomes spatially resolved in the radio (e-Merlin) or optically from space (*HST*), and on a conventional ground-based optical telescope (Gnd; from Bode & Evans 2008).

the common-envelope phase where the ejecta from the WD envelope engulf the secondary star within a matter of minutes following outburst. The secondary transfers energy and angular momentum to the ejecta (Livio et al. 1990; Lloyd et al. 1997). However, these models created oblate structures. Porter et al. (1998) incorporated the WD rotation into the calculations of the common-envelope phase producing the observed prolate remnants (e.g., Slavin et al. 1995).

## 1.9 This Work

There has been a long tradition of modelling the nova explosion to understand the basic physics and physical parameters. These include the evolution of the nebular remnant, which can then be used as a distance indicator via the expansion parallax relation of Equation 1.5, and the inclination of the system (related to that of the central binary), which can be used to determine the component masses and the expansion velocity and nebular shaping.

Studies of the line profiles have proven fruitful with an estimate of the true 3D geometry of the system. However, modelling the line profiles is hindered by the fact that assumptions about the model, and the line itself, must be made. In order to better constrain a model from line profile modelling the model should ideally produce some testable predictions. For example, if the inclination suggests that eclipses are observable then a search for these should be attempted to test the model.

This thesis has the overall aim to explore the morphology of the remnants of CNe and RNe and to derive important physical parameters in each case. This is achieved by developing sophisticated models from a combination of spectroscopy and resolved imaging (where available). In Chapter 2 a morpho-kinematical code is introduced and compared to previous work to gain full understanding of how the code performs. In Chapter 3 the code is applied to a combination of *HST* imaging and ground-based optical spectroscopy to derive important physical parameters

---

of the expanding nebular remnant of the RN RS Oph. In Chapters 4 and 5 the code is used to replicate the observed early spectroscopic evolution of two RNe candidates, V2491 Cyg and V2672 Oph. In Chapter 6, optical and X-ray behaviour of KT Eri (another proposed RN candidate among the CNe) are discussed as well as morpho-kinematical modelling of the remnant as applied in Chapters 4 and 5. Finally, a summary and future work are presented in Chapter 7.

# Chapter 2

## Models of the Ejecta of Novae

### 2.1 Introduction

Modelling the ejecta of novae has been performed for several decades now. They have usually been modelled using spatially unresolved spectroscopy (e.g., Hutchings 1972a,b; Solf 1983), while if nova shells are spatially resolved and if combined with spectroscopy the results can provide better constraints on the true behaviour of the nova shell while providing important physical parameters – for example, inclination, expansion velocity and hence distance (e.g., Slavin et al. 1995; Gill & O’Brien 1998, 2000; Harman & O’Brien 2003).

Hutchings (1972a) developed numerical methods to compute stellar line profiles and continuum fluxes for different geometries. The line profiles are calculated for the established geometry, where the flux is computed assuming the flux is normal to the stellar surface. The program simply sums the flux from each visible sector, with a limb-darkening factor depending on the angle between the line of sight and the sector.

Hutchings (1972b) applied the code described above demonstrating how the geometry of the envelope determines the line profile and applying the techniques to three novae; HR Del, LU Vul and FH Ser. In HR Del and FH Ser the derived

morphologies, polar blobs and 2 rings, and polar blobs respectively, replicated well the line profiles and velocity behaviour. In the case of LU Vul, the morphology only replicated marginally the observations. Furthermore, the inclination of the systems were derived. However, it is worth noting that Harman & O'Brien (2003) from their *HST* resolved imaging and ground-based spectroscopy of HR Del derived an inclination of  $35\pm 3^\circ$ . Although this value seems half of that,  $62^\circ$ , estimated from Hutchings (1972b) they are in line with each other. This is due to the way Hutchings (1972a) defines the inclination, as the angle between the pole of rotation and the line of sight. The morphology of the system was described by Harman & O'Brien (2003) as a closed hourglass with an equatorial ring and evidence for two polar rings in line with the geometry found by Hutchings (1972b).

Gill & O'Brien (1999) developed a code to calculate optically thin emission line profiles for CN shells. The emission is calculated by generating a velocity cube with two spatial dimensions (the plane of the sky) and one dimension representing the velocity along the line of sight. To generate a spectrum the cube is collapsed in the spatial directions while to generate an image the collapse happens in the spectral direction. The emission is proportional to the volume and the square of the density and added into the appropriate bin in the velocity cube (see Section 2.2.4 for some example images).

Other codes developed include *XSHAPE* (Harman 2001) which used the backbone of an existing code used for active galactic nuclei (AGN; Holloway et al. 1996). This code again was based on optically thin emission and produced synthetic images and position-velocity profiles.

It is not always easy to acquire spatially resolved images due to several factors. For example, the time since outburst versus the velocity of the ejecta and the distance to the object, and the brightness of the shell (see for example, Equation 1.5 and Figure 1.8). Therefore, it is important to develop codes that can be used to extract information about spatially unresolved spectroscopic observations (line profiles). In the rest of this Chapter a description of the code used extensively in this thesis is provided. The choice of the code described below comes from the

need to have a code that was appropriate for the task, publicly available and that did not require user programming intervention.

## 2.2 SHAPE

SHAPE<sup>1</sup> is a morpho-kinematical code used to analyse and disentangle the 3D geometry and kinematic structure of nebulae and other astrophysical phenomena (Steffen & López 2006; Steffen et al. 2010). SHAPE was originally developed to model the complex structures of AGN (Holloway et al. 1996). It has been developed with the ability to be user-driven and interactive to reconstruct the 3D structure of astrophysical objects based on data sets that do not allow an automatic reconstruction. Most of the time this is due to the lack of sufficiently detailed data or the basic assumptions for the reconstruction algorithm are not met by the object.

To model in SHAPE, first the observations must be initially interpreted. These observations can be an image of an object or a spectrum (a combination of both is ideal, as described previously). This is used as a first guess/estimate of the 3D structure of the system. This is improved with the introduction of an emissivity and velocity field. The structures are rendered to produce synthetic images and spectra so that these can be compared with observations.

It is noteworthy to mention that SHAPE is not a hydrodynamical or N-body code. What SHAPE does allow is for the analysis of 3D structures and kinematics of astrophysical nebulae. However, SHAPE has the potential application for modelling of complex 3D structures as initial conditions of numerical photo-ionisation and hydrodynamic calculations as well as the visualisation and calculation of spectral information resulting from such calculations.

---

<sup>1</sup>Available from <http://bufadora.astrosen.unam.mx/shape/>

### 2.2.1 Using SHAPE

Here a description of using SHAPE's graphical user interface (GUI), input and output information is provided. SHAPE's GUI is initiated from the world wide web as a java webstart. The initial window shows the most recent news (Figure 2.1a). The user opens a project which loads the rendering module window (Figure 2.1b).

The rendering module window allows the user to set the general parameters for the output image. Here the dimensions are set for (a) the image, in analogue to the CCD image dimensions, and the slit size and position on the sky; (b) the velocity range for the position-velocity, 1D line profile (Section 2.2.3) and the resolution (in  $\text{km s}^{-1}$ ), analogues to the spectrograph resolution; (c) the rotation (inclination and position angle) of the object; (d) the rendering technique (Section 2.2.2); and (e) the units of the system.

In the 3D module window (Figure 2.1c) the user sets the basic geometry of the object. There are basic structures from which the user can choose to start with; sphere, torus, cylinder, to name a few. In the *Permitive* option the user sets the size of the object. The basic structures can be "deformed" using the *Modifiers* options. A brief discussion of some of the *Modifiers* used is provided below:

- Velocity (Figure 2.1d) – this allows to set the velocity field within the object. There are two modes to determine the velocity field of the outburst; a quick mode which provides a simple formula,  $f(r) = A + B*(r/r_0) + C*(r/r_0)^D$ , where A, B, C and D are constants, r and r0 are the position away from the centre and r0 the maximum size of the structure; and a custom mode where the user has the option to determine the velocity field.

The nova and PNe community often use the term "Hubble flow" velocity to describe the velocity field within the expansion. It is an analogous to the cosmological usage where expansion velocity is proportional to distance from the center – typical of a point-like explosion.

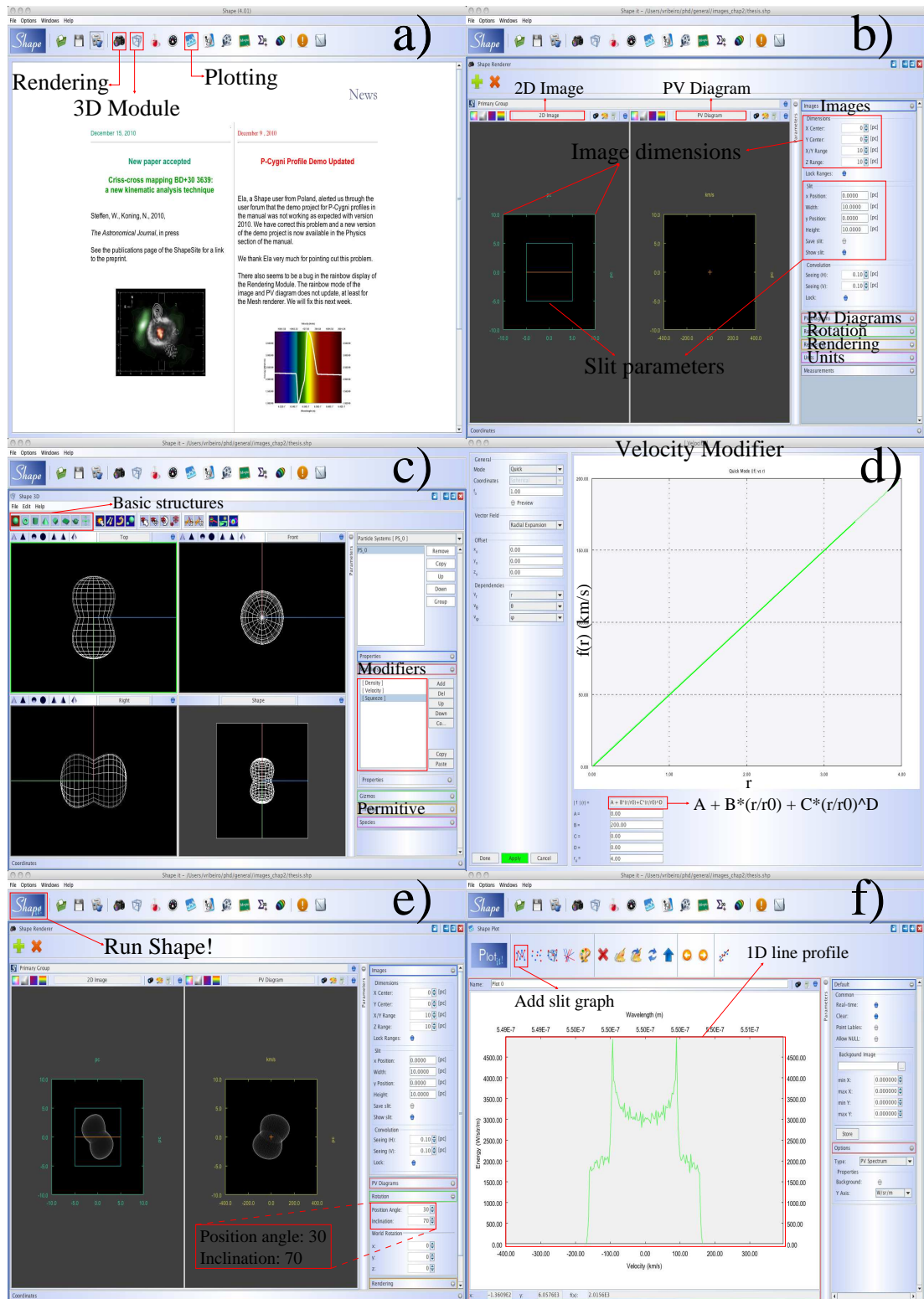


Figure 2.1: SHAPE graphical user interface showing the modules used for this work. a) Initial page showing recent news related to SHAPE. b) Rendering module where input parameters are set. c) 3D module where the basic structure are set and modified. d) An example of the velocity modifier. e) Output image from the rendered structures and initial parameters. f) 1D line profile of the rendered structures and initial parameters.

- Density – as the name suggests this provides the number density per cubic meter in the object. The density distribution can follow the same principle as demonstrated in Figure 2.1*d*.
- Squeeze – describes how much of a pinch the structure should have. This has been used in this work to determine the ratio between the major- to minor-axis.

All the points discussed above are inputs which are then rendered (Section 2.2.2) to produce output images (Figure 2.1*e*) and 1D line profiles (Figure 2.1*f*). These outputs are extensively used for this work and the 2D images are retrieved from the rendering module and the 1D line profile (Section 2.2.3) from the plotting module window. These line profiles are calculated from the velocity along the line of sight. Furthermore, the 2D image output can be saved as an image and the 1D line profiles as an ASCII file which are then used to compare with the observational data.

## 2.2.2 Rendering and distribution

Several rendering options are available in SHAPE. However, the ones used throughout this work are *particle* and then *mesh* renders. The distribution of material within a certain structure can either be a volume or a surface distribution.

The *particle* renderer uses a random distribution of particle numbers, determined by the user. Each particle has its own emissivity and velocity information and their values are added directly to the image pixels or spectrum according to their projected position and velocity along the line of sight. However, the *particle* renderer should not be confused with physical particles but is for visualisation and defining the sampling.

The *mesh* renderer sets up the volume cube into regular grids. The emission is determined from the fraction of the assumed structure that is located within the individual grid and then each individual grid's information is projected onto the

image plane.

In Figure 2.2 a simple spherical model is presented to show both how the *particle* and *mesh* renderers are equivalent and how the line profile of a simple sphere should look. What is immediately evident is that both the *particle* and *mesh* are indeed equivalent. The *particle* renderer was initially used from a very early version of SHAPE when the *mesh* renderer was not yet available. However, the *mesh* renderer is preferred due to the speed of the rendering and how well the image and spectra are sampled compared to the *particle* renderer.

Furthermore, Figure 2.2 is a test of the code since a sphere is the simplest structure, and results can be easily interpreted. On a surface distribution with all the material travelling at a constant velocity then the expected shape of the line profile is that of a top hat. While for a volume distribution there is much greater range of velocities, since the velocity is set as a “Hubble flow”, where the faster moving material is at a proportionately greater distance from the central source, and therefore the line profile is expected to be an inverted “U” shape because there is more lower velocity material in the line of sight. The “noise” on the synthetic spectra of Figure 2.2 is caused by the finite resolution (briefly discussed in Section 2.2.3).

### 2.2.3 1D line profiles

The line profiles are divided into 256 bins, regardless of their velocity range. This is reasonable for low velocities. However, for high velocities, as in the Figures 2.3 and 2.4, then the profiles become noticeably “noisy”. This “noise” can be smoothed by setting a resolution to the spectra by convolution with a Gaussian kernel, ideally at the resolution of the spectrograph, which will reduce the noise in the line profiles.

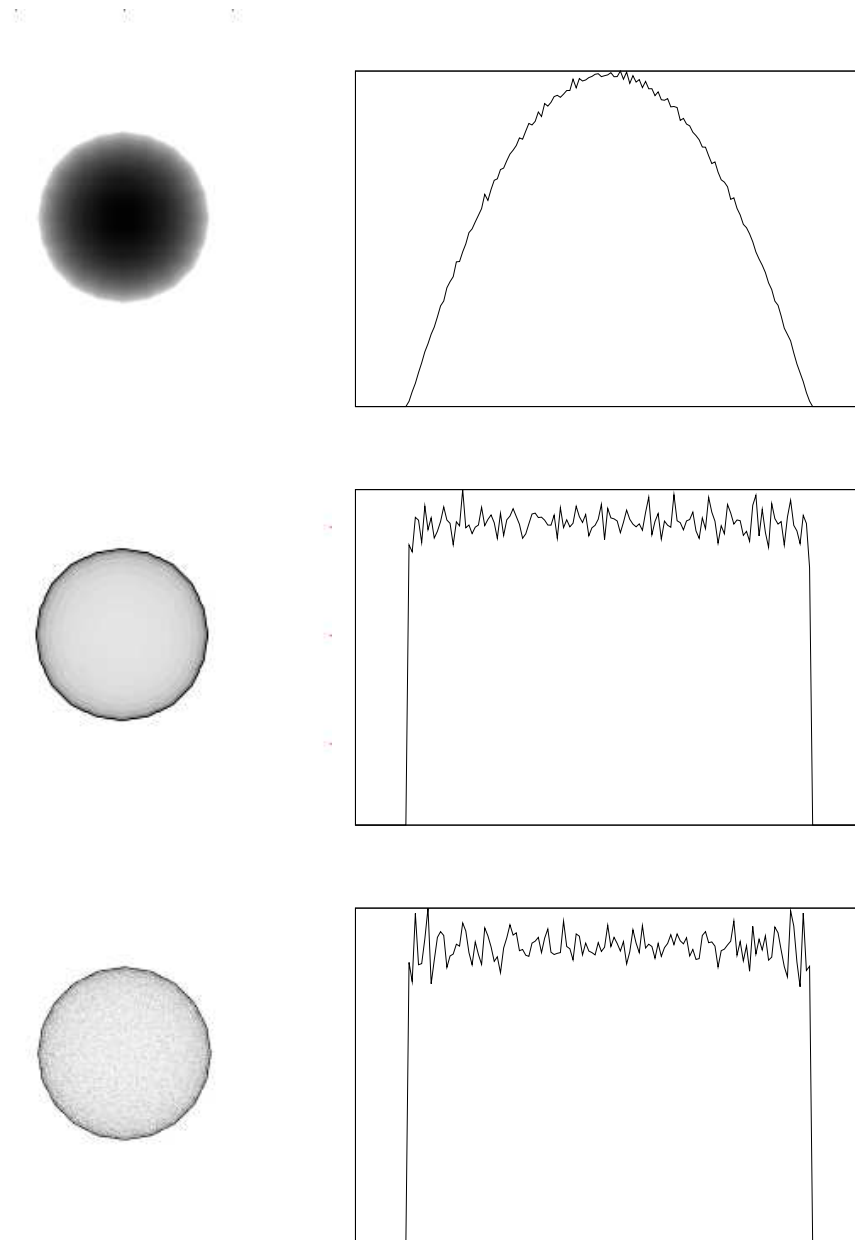


Figure 2.2: Synthetic images and line profiles for a simple SHAPE model demonstrating a spherical structure with both volume and surface distributions produced with a *particle* and *mesh* rendering. The top two panels are synthetic images and spectra for the *mesh* rendering of a volume and surface distribution (top and middle panels, respectively). The bottom panel is the synthetic image and spectrum for a *particle* rendering with surface distribution with one hundred thousand particles.

### 2.2.4 Testing against early models

The SHAPE code results were compared to the results in Gill & O'Brien (1999) since these produce both synthetic images and line profiles. The Gill & O'Brien (1999) code was not available for comparison however. Therefore when comparing the SHAPE code results with Gill & O'Brien (1999) it was based on some of the details within the published literature and by eye. For example, in the case of the size of the extra features on the underlying ellipsoid. The next discussion follows with models using a surface distribution.

The first model, shown in Figure 2.3, is that of a prolate structure (major to minor axis ratio of 1.33) with equatorial and tropical rings. The rings were enhanced by twice the background. The velocity was in the form of a Hubble flow. The chosen inclination of  $60^\circ$  was arbitrary (from a choice of  $0^\circ$ ,  $30^\circ$ ,  $60^\circ$  and  $90^\circ$  from Gill & O'Brien 1999). Differences in the images and line profiles are due to brightness contrast and binning, respectively. However, the results presented in Figure 2.3 show both images and line profiles to be very similar. Subtle differences can be attributed to the sizes and positions of the rings.

The previous paragraph argument follows on to the second model, shown in Figure 2.4. In this case presented is a system with an equatorial ring and polar caps. The polar caps start at the position of the tropical rings and both polar caps and equatorial ring have a density enhancement twice that of the overall structure. It can be seen that again, the results are qualitatively very similar.

### 2.2.5 Optimizer module

The optimizer module is a powerful tool developed within SHAPE to automatically improve the fit of the set parameters using a least squares minimization. Here the user estimates an initial structure, velocity field (in order to retrieve a 1D line profile) and other parameters. The general strategy to optimize a structure is to choose one or more of the parameters to optimize. The user then provides a

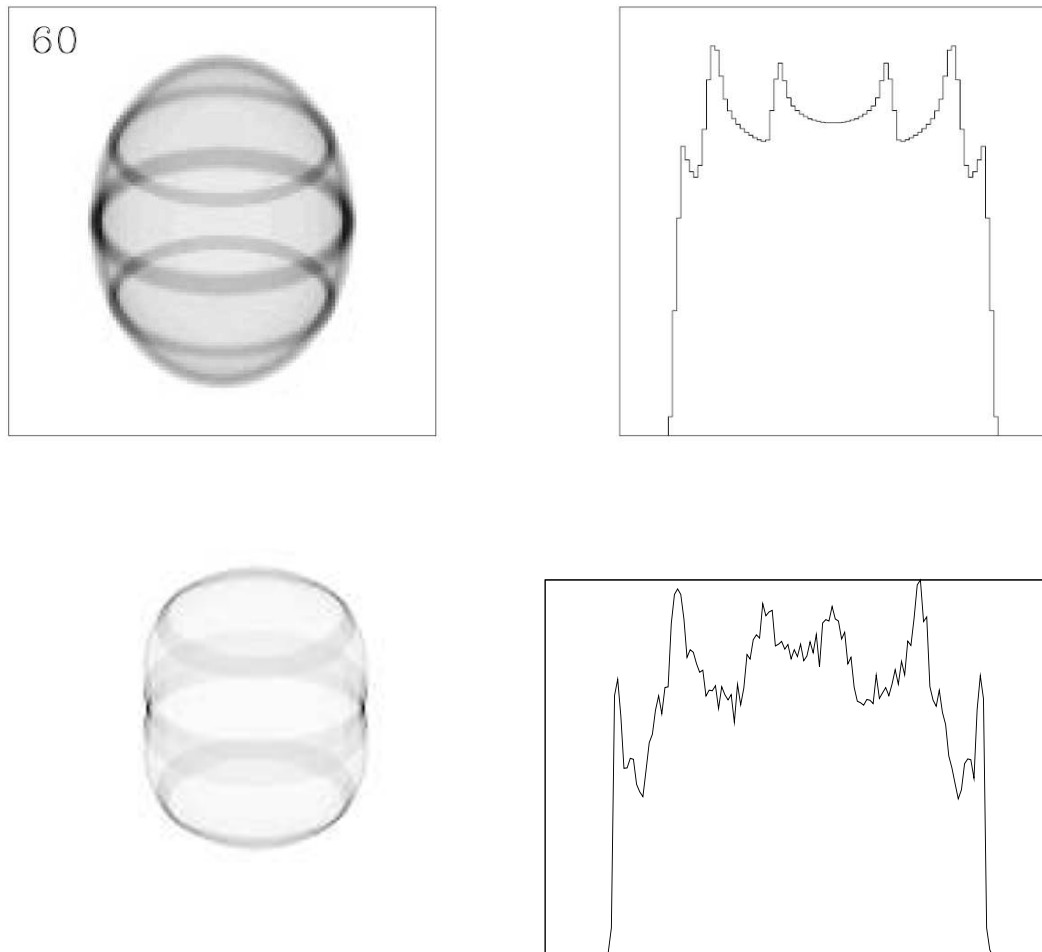


Figure 2.3: Synthetic images and line profiles for a system with enhanced brightness in equatorial and tropical rings. The top panel is from Gill & O'Brien (1999) for a system inclined at  $60^\circ$ . The bottom panel is from SHAPE for a system also inclined at  $60^\circ$ . It should be noted that the geometries are not exactly the same and differences in the images and line profiles are attributed to the brightness contrast and binning sampling, respectively.

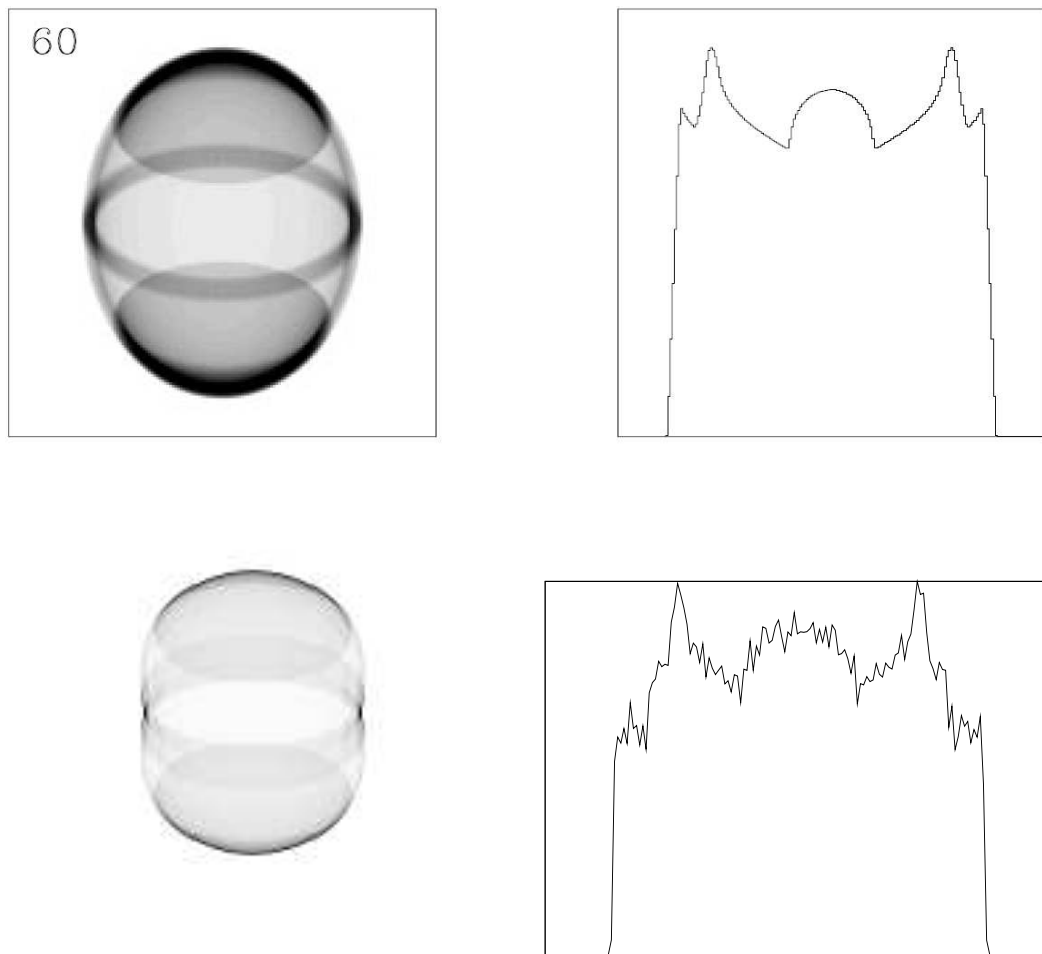


Figure 2.4: As Figure 2.3 but for a system with enhanced brightness in the equatorial ring and polar caps.

range of values which the optimizer searches around. The initial values are those attributed by the user during the initial guess. Then, in the case of this project, a line profile is loaded which drives the minimization process, although, the user may also load an observed image or position-velocity diagram.

Once the optimization process starts, the model is compared with the observation to generate a least-squares difference. The values of the parameters are varied over the range that was preset to find the least-squares solution and in the order they appear in the stack. The cycle of optimization is repeated until a minimum difference is achieved.

## 2.3 Contributions to SHAPE

In this section, user suggestions that led to further development of SHAPE are briefly described. The contributions made have generally been driven by the requirements of this work. However, other minor contributions are also presented.

### 2.3.1 Doppler filter profile

The use of narrowband filters in an imager means that not all the light from a broad spectral line arrives on the detector. Furthermore, the detectors have varying sensitivity at different wavelengths (see Chapter 3 for further details). In systems like PNe the velocities are very low and the emission line of interest generally fits within the narrowband filter range. However, in CN systems it is not always the case due to their high ejection velocities, which can reach several thousands of kilometres per second. Therefore, the Doppler filter was introduced which allows the user to render specific velocity ranges replicating the response function of the narrowband filter on an instrument.

### 2.3.2 Other contributions

The projects presented in Chapters 4 and 5 presented a whole new challenge. In these cases all the information was solely in the form of line profiles and therefore to model these an assumption on the structure was made. This presented a new challenge on how to handle the data. There is an animation option within SHAPE that allowed the user to dump out figures of the rendered images. However, for these projects, what was required was the line profile information, i.e. an ASCII file with velocity and flux information which was subsequently made available. This allowed the project to run at a much faster pace than the previous option, which involved human intervention.

Further contribution concerned how the *mesh* renderer worked with structures that occupied the same area of space. It was realised that the velocities were being averaged rather than being added. This averaging inadvertently affected the shape of the line profiles and SHAPE was modified accordingly.

## 2.4 Concluding Remarks

Although initially developed for AGN, and extensively used for PNe, SHAPE can certainly be applied to nova outbursts as demonstrated with the comparison with previous models that were used for such objects. Contributions of the work presented here to SHAPE were also briefly discussed; these contributions greatly enhanced this work.

In the next Chapter a description is given of how SHAPE was applied in the context of this work to the RN RS Oph to model the expanding nebular remnant as observed with *HST* imaging and ground-based spectroscopy.

# Chapter 3

## The Expanding Nebular

## Remnant of the Recurrent Nova

## RS Ophiuchi<sup>1</sup>

### 3.1 Introduction

RS Ophiuchi is a symbiotic recurrent nova with outbursts recorded in 1898, 1933, 1958, 1967, 1985 (see Rosino 1987; Rosino & Iijima 1987) and 2006 (Evans et al. 2008, and references therein, see also Chapter 1). However, during the period 1898–1933, before the star was known to be a RN, some outbursts might have occurred, most likely in 1907 (Schaefer 2004). There is also evidence for an eruption in 1945 (Oppenheimer & Mattei 1993). RS Oph was observed to be undergoing its latest eruption on 2006 February 12.83 (Narumi et al. 2006), reaching a magnitude  $V = 4.5$  at this time. This is defined as  $t = 0$ . Later work by Hounsell et al. (2010) showed the peak of the outburst occurring on 2006 February 12.94. The optical light curve then began a rapid decline, consistent with that seen in previous outbursts (Rosino 1987, AAVSO<sup>2</sup>). The distance to RS Oph has

---

<sup>1</sup>The work presented in this Chapter was published in Ribeiro et al. (2009).

<sup>2</sup>see <http://www.aavso.org>

been derived from several lines of evidence as  $1.6 \pm 0.3$  kpc (Bode 1987; see also Barry et al. 2008).

The RS Oph binary system comprises a red giant, with a spectral type estimated to be in the range G5III to M4III (e.g., Bohigas et al. 1989; Anupama & Mikolajewska 1999), and a WD with mass thought to be close to the Chandrasekhar limit (see Dobrzycka & Kenyon 1994; Shore et al. 1996; Fekel et al. 2000; Brandi et al. 2009). Accretion of hydrogen-rich material from the red giant onto the WD surface leads to a thermonuclear runaway, as in the outbursts of CNe (again, see Chapter 1). Spectroscopy of RS Oph has shown  $H\alpha$  line emission with  $\text{FWHM} = 3930 \text{ km s}^{-1}$  and  $\text{FWZI} = 7540 \text{ km s}^{-1}$  on 2006 February 14.2 ( $t = 1.37$  days; Buil 2006).

Unlike CNe, where the mass donor is a low mass main sequence star, the presence of the red giant in the RS Oph binary means that the high-velocity ejecta run into a dense circumstellar medium in the form of a red giant wind, setting up a shock system. The forward shock moving into the wind has a gas temperature  $\sim 2.2 \times 10^8$  K for a shock velocity  $v_s = 4000 \text{ km s}^{-1}$  (Bode et al. 2006).

Very Long Baseline Interferometry (VLBI) radio observations by O'Brien et al. (2006) at  $t = 13.8$  days showed a partial ring of non-thermal radio emission resulting from the expanding shock, which developed into a more bipolar structure (see also O'Brien et al. 2008). The asymmetry in this ring was suggested to be due to absorption in the overlying red giant wind and they also noted the emergence of more extended components to the east and west. Sokoloski et al. (2008) followed the evolution of the radio source with the Very Long Baseline Array (VLBA) at 4 epochs between days 34 and 51 after outburst. They found a central thermally-dominated source linked by what appeared to be a narrow (collimated) outflow to expanding non-thermal lobes which they interpreted as the working surfaces of jets. Jet collimation could be due to the expected accretion disc around the WD. It should be noted that Taylor et al. (1989) had also interpreted their 5 GHz VLBI map from day 77 after the 1985 outburst in terms of a central thermal source with expanding non-thermal lobes.

From *HST* observations, 155 days after outburst, Bode et al. (2007) revealed the remnant to have a double ring structure with the major axis lying in the east-west direction (see also Section 3.3). They suggested that there was evidence for deceleration in the north-south direction by comparing their observations to earlier epoch observations in the radio (O’Brien et al. 2006). Bode et al. (2007) also provided preliminary models of the remnant as a bipolar structure which implied a true expansion velocity,  $V_{\text{exp}} = 5600 \pm 1100 \text{ km s}^{-1}$  for the material at the poles. It was proposed that the shaping of the remnant occurred due to the ejecta interaction with the pre-existing circumstellar environment.

Mastrodemos & Morris (1999) examined the influence of a detached binary companion on the dusty winds from red giant and asymptotic giant branch stars with 3D smoothed particle hydrodynamics models. Their parameter space included wind outflow velocities in the range of 10–26  $\text{km s}^{-1}$ , circular orbits with binary separations of 3.6–50 AU and binary companions having masses in the range of 0.25–2  $M_{\odot}$ . They found by varying these parameters that a range of envelope geometries and density contrast can be replicated: bipolar, elliptical and quasi-spherical. However, Mastrodemos & Morris (1999) did not explore the parameter space for a system like RS Oph, with a wind velocity of 40  $\text{km s}^{-1}$  (Wallerstein 1958) and binary separation  $\sim 1$  AU, but some extrapolation might be possible using their Figure 21*b*.

The projected 2D geometry of nova explosions on the sky is usually complex, as are their 1D spectra. However, taken together they provide the underlying 3D structure of an object. The projected image on the sky provides spatial information on its structure while the spectra provide information about the component of the velocity vector along the line of sight. In the following sections the *HST* observations of the expanding nebular remnant, taken at  $t = 155$  days and those at a second epoch at  $t = 449$  days after outburst, are re-examined. These are compared to spectral observations (where available), then using the code described in Chapter 2, the detailed 3D structure of the remnant is determined. In Section 3.2 the observations and data reduction methods used in this study are presented.

The results of the observations are shown in Section 3.3 and then modelled in Section 3.4. The results of the modelling are presented in Section 3.5. In Section 3.6 the results of the *HST* imaging are compared with X-ray observations. Finally, in Section 3.7 a discussion of the results is presented.

## 3.2 Observations and Data Reduction

### 3.2.1 Hubble Space Telescope imaging

RS Oph was imaged with the *HST* on two occasions, under the Director's Discretionary programmes GO/DD-11004 and GO/DD-11075. The first observations were made on 2006 July 17 (155 days after outburst) with the High-Resolution Channel (HRC) of the Advanced Camera for Surveys (ACS), with a scale of  $0''.025$  pixel<sup>-1</sup> (equivalent to 40 AU pixel<sup>-1</sup> at  $d = 1.6$  kpc). The second observations were made on 2007 May 7 (449 days after outburst) with the Planetary Camera CCD of the Wide Field Planetary Camera 2 (WFPC2), with a scale of  $0''.046$  pixel<sup>-1</sup>, since in the meantime the ACS had suffered a failure. During the first epoch observations, the ACS/HRC was used with three narrowband filters to isolate the H $\alpha$ + [N II] (F658N), [O III] (F502N) and [Ne V] (F344N) nebular emission lines. For the subsequent WFPC2 observations, only the F502N filter was used in order to isolate the [O III] emission line. This emission line was chosen based on the results from the first epoch observations.

Work detailed below concentrated on the F502N filter observations common to both epochs. The other two *HST* filter bands, F344N and F658N, were not taken into account because there is no spectral information available for the former and the latter presented no detectable structure in the first epoch *HST* images (see Bode et al. 2007).

Table 3.1: Log of optical spectral observations.

Date (days after outburst)	Instrument	Total Exposure time (s)	R
2006 February 22 (10)	Echelle	430	16000
2006 February 23 (11)	Echelle	425	16000
2006 February 24 (12)	Echelle	435	16000
2006 February 25 (13)	Echelle	435	16000
2006 March 14 (30)	Echelle	600	16000
2006 March 15 (31)	Boller & Chivens	90	2355.2
2006 April 17* (64)	Boller & Chivens	150	1668.6
2006 April 18* (65)	Boller & Chivens	140	3149.6
2006 May 29 (83)	Boller & Chivens	40	1525.9
2006 June 18 (126)	Echelle	1830	16000
2006 June 19 (127)	Echelle	990	16000
2006 July 30 (168)	Echelle	420	16000

\* Observations taken at the Observatorio Astrofísico Guillermo Haro, otherwise from Observatorio Astronómico Nacional en San Pedro Mártir.

### 3.2.2 Ground-based spectroscopy

Spectral observations were carried out by collaborators at the Observatorio Astronómico Nacional en San Pedro Mártir, Baja California, México, using the 2.1m telescope with the Boller & Chivens and Echelle spectrographs, and at the Observatorio Astrofísico Guillermo Haro, at Cananea, Sonora, México, using the 2.12m telescope with their Boller & Chivens spectrograph. The Boller & Chivens spectrographs have intermediate spectral resolutions, from  $R \sim 1500$  to 3500, while the Echelle spectrograph has a maximum resolution of about  $R = 18000$  at  $5000\text{\AA}$ .

The observations were carried out over several epochs from days 10 (2006 February 22) to 168 (2006 July 30) after outburst. The log of spectroscopic observations is shown in Table 3.1. For direct comparison with the *HST* imaging the work focused on the spectral wavelength region around the [O III]  $5007\text{\AA}$  emission line, which falls in the *HST* F502N narrowband filter.

### 3.2.3 Hubble Space Telescope data reduction

All data were reprocessed using standard procedures outlined in the ACS<sup>3</sup> and WFPC2<sup>4</sup> Data Handbooks and the Pydrizzle<sup>5</sup> and Multidrizzle<sup>6</sup> Handbooks.

The observations were taken using the dithering technique which involves spatially offsetting the telescope by shifts that are generally small relative to the detector size, therefore moving the target to a number of different locations on the detector. This is useful to facilitate the removal of bad pixels and improve spatial sampling of the Point Spread Function (PSF).

The ACS/HRC and WCPC2 have similar data reduction steps but different reduction methods. The Pydrizzle package has been developed to work well with ACS/HRC data and is a simpler package to use than calling different commands within, for example, IRAF. Therefore, below an outline description of the data reduction steps for the WCPC2 is given:

- Determine the sky value for subtraction.
- Remove cosmic rays.
- Determine the shift offsets between the images and a reference image.
- Create a static pixel mask file from the calibrated image data quality file.
- Drizzle the images using the offsets determined above and combine them. Drizzle is a linear reconstruction method for an image that has been under-sampled and dithered (Fruchter & Hook 1997).
- If the combined image is cosmic ray free then it is blotted, which basically maps the combined image back to each input image. The blot task is essentially the reverse of drizzling.

---

<sup>3</sup>See [http://www.stsci.edu/hst/acs/documents/handbooks/DataHandbookv5/ACS\\_longdhbcover.html](http://www.stsci.edu/hst/acs/documents/handbooks/DataHandbookv5/ACS_longdhbcover.html)

<sup>4</sup>See [http://www.stsci.edu/instruments/wfpc2/Wfpc2\\_dhb/WFPC2\\_longdhbcover.html](http://www.stsci.edu/instruments/wfpc2/Wfpc2_dhb/WFPC2_longdhbcover.html)

<sup>5</sup>See <http://stsdas.stsci.edu/pydrizzle>

<sup>6</sup>See <http://stsdas.stsci.edu/pydrizzle/multidrizzle/>

- Create a derivative image to estimate the effects caused by blurring in the median image and errors in the input offsets.
- Now cosmic rays can be identified by comparing the blotted image with each original image.
- A master mask for each image can now be created by multiplying the static pixel mask with each individual cosmic ray mask file.
- The master mask file is then used in the final drizzle where all the input images are drizzled together.

Although these steps can be automated, it is important to have a look at the individual files produced to see that the tasks are performing as they should.

PSF profiles were generated using TinyTim (Krist 1995) for both ACS/HRC and WFPC2 images. In the ACS/HRC and WFPC2 images, the PSF flux was scaled to an extent such that when subtracted from the observed image the new PSF-subtracted image pixel flux was close to those surrounding it. Deconvolution was then performed using the Lucy-Richardson method (Richardson 1972; Lucy 1974) for the ACS/HRC and WFPC2 images. CLEAN (Högbom 1974) and Maximum Entropy (e.g., Wu 1993) techniques were also used as a check, and produced similar results.

## 3.3 Observational Results

### 3.3.1 Hubble Space Telescope images

The first epoch observations clearly show extended structure in the [O III] line in the deconvolved images, as well as in the raw images at both epochs (Figure 3.1). As reported in Bode et al. (2007), a striking feature is the double ring structure (top image in Figure 3.1) with the major axis lying east-west with a total (peak-to-peak) extent of  $360 \pm 30$  mas, in the plane of the sky, corresponding to an

expansion rate of  $1.2 \pm 0.1$  mas day<sup>-1</sup> (and equivalent to  $V_t = 3200 \pm 300$  km s<sup>-1</sup> for  $d = 1.6$  kpc, where  $V_t$  is the transverse velocity). More extended emission was detected above background in the deconvolved image with an expansion rate of  $1.7 \pm 0.2$  mas day<sup>-1</sup> and, when compared with values seen in the radio, it was suggested in Bode et al. (2007) that the east-west bipolar emission seen here and in the radio arises from the same regions of the remnant, if the expansion velocities in the east-west direction are roughly constant after outburst (see also O'Brien et al. 2008).

The north-south (peak-to-peak) extent is  $150 \pm 25$  mas corresponding to an expansion rate of  $0.48 \pm 0.08$  mas day<sup>-1</sup>. Results of the expansion in the early radio observations (O'Brien et al. 2006; Rupen et al. 2008) and more recently from O'Brien et al. (2008), led to a north-south expansion rate of  $0.77 \pm 0.04$  mas day<sup>-1</sup> derived from observations over the first 107 days, suggesting deceleration in this direction (Bode et al. 2007).

In the second epoch observation images (bottom images on Figure 3.1), structure is still visible in the [O III] line. It has an east-west extent of  $1100 \pm 100$  mas (peak-to-peak) corresponding to an expansion rate from the centre of  $1.2 \pm 0.1$  mas day<sup>-1</sup> suggesting no deceleration had taken place between epochs in terms of greatest east-west extent. The north-south extent is much harder to determine but is approximately  $460 \pm 46$  mas corresponding to an expansion rate of  $0.51 \pm 0.03$  mas day<sup>-1</sup>. This result would imply that no deceleration occurred in the north-south direction between the two epochs.

Furthermore, the extent of the remnant at each epoch is compared with the expected dimensions of the red giant wind. Assuming a wind that has been expanding for 21 yrs (the period between the last two outbursts) and a wind velocity of  $40$  km s<sup>-1</sup> (Wallerstein 1958), this implies a maximum wind radius of  $2.6 \times 10^{15}$  cm. For a distance  $d = 1.6$  kpc, the first epoch angular size suggests the outburst remnant has maximum east-west extent from the centre of  $4.3 \pm 0.4 \times 10^{15}$  cm and at the second epoch the remnant has maximum extent  $1.3 \pm 0.1 \times 10^{16}$  cm. Therefore, by the time of the *HST* observations the remnant

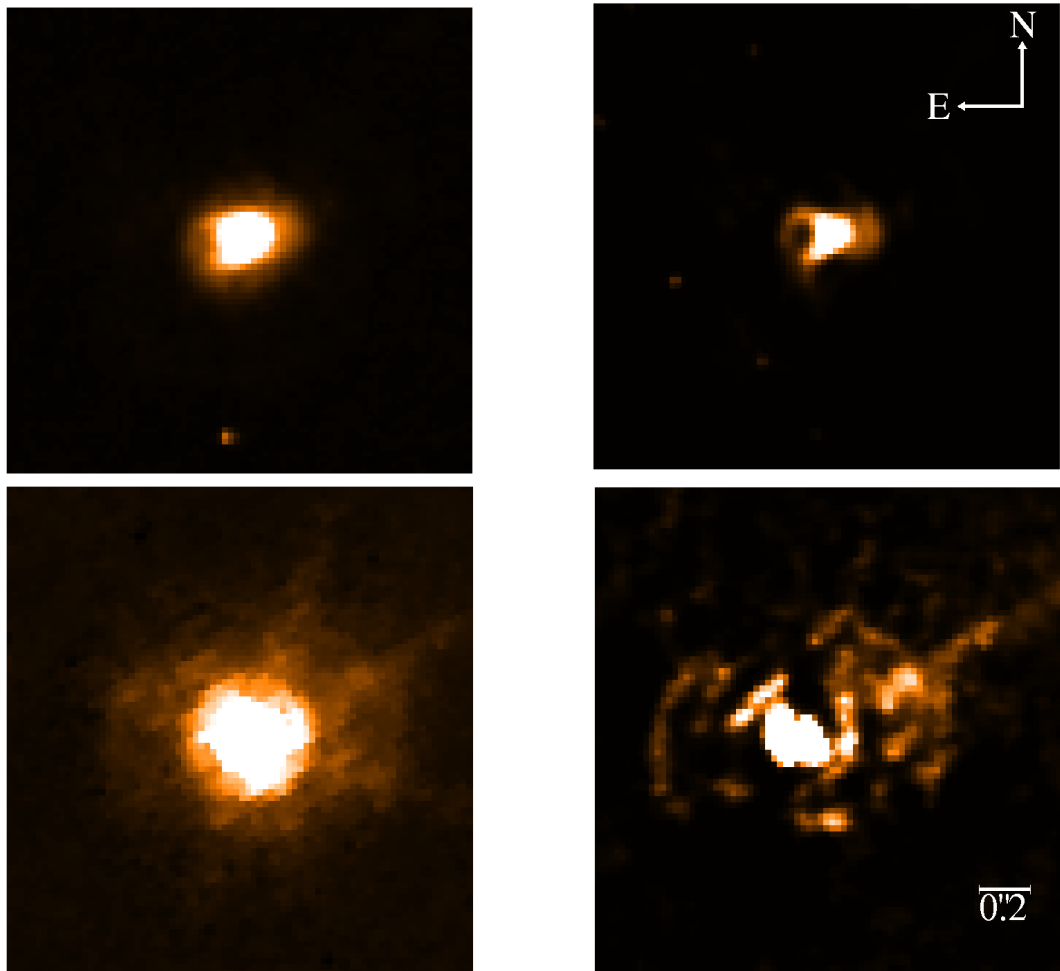


Figure 3.1: *HST* images of RS Oph through the F502N filter. *Top left* - Raw image from the first epoch observations ( $t = 155$  days after outburst) using the ACS/HRC. *Top right* - PSF-subtracted and deconvolved image using a TinyTim PSF, showing a double ring structure. *Bottom left* - Raw image from the second epoch observations ( $t = 449$  days after outburst) using WFPC2. *Bottom right* - PSF-subtracted and deconvolved image using a TinyTim PSF, again showing evidence of a double ring structure (note that the “jet-like” feature on the WFPC2 deconvolved image is an artifact caused by bleeding on the CCD chip; see also Section 3.6). North is up and east is to the left in all images.

appears larger in the east-west direction than the expected size of the red giant wind.

### 3.3.2 Ground-based spectroscopy

In Figures 3.2–3.4 the spectral evolution of RS Oph as determined from low resolution spectra obtained from day 31 to 83 after outburst is shown. The principal emission lines were identified following Rosino (1987).

Figure 3.2 shows the observed spectrum 31 days after outburst. The visual magnitude had declined to  $V \sim 9$  by this time. The spectrum shows the presence of broad emission lines of H $\beta$ , H $\gamma$ , H $\delta$ , He I ( $\lambda$ 4471, 4713, 4922, 5016, 5048 and 5411), Fe II (multiplets 27, 28, 42, 48, 49), N III  $\lambda$ 4640 and [Si II]  $\lambda$ 5041. What Rosino (1987) identified as the [Ar X]  $\lambda$ 5535 coronal line is also present.

Figure 3.3 shows spectra taken on days 64 and 65 after outburst. The magnitude had now declined to  $V \sim 10$ . The spectra show an increased degree of excitation, with the presence of moderately strong coronal lines of [Ar X]  $\lambda$ 5535 plus Fe XIV  $\lambda$ 5303, and [Fe X]  $\lambda$ 6374. Also present at this time are the nebular lines of [O II] ( $\lambda$ 4363, 4959 and 5007) and [N II]  $\lambda$ 5755.

Figure 3.4 shows spectra on day 107 after outburst ( $V \sim 11.5$ , i.e. approaching minimum light). Here the Fe XIV  $\lambda$ 5303 and [Ar X]  $\lambda$ 5535 lines have become significantly weaker. In contrast, the spectrum also shows an increase in the relative strength of [O III], and [N II], and [O I]  $\lambda$ 6300 has appeared.

This spectral evolution is typical of that seen in previous outbursts (Rosino 1987; Rosino & Iijima 1987). As an aside to the main discussion, the lines identified by Rosino (1987) and others as coronal lines, for example on the day 64 spectrum, are blueshifted with respect to the Balmer and other lower excitation lines by  $\sim 100 \text{ km s}^{-1}$ . This may be related to the relative principal regions of origin of these lines within the velocity field of the remnant.

The higher resolution spectra in the region of the [O III] emission line were used

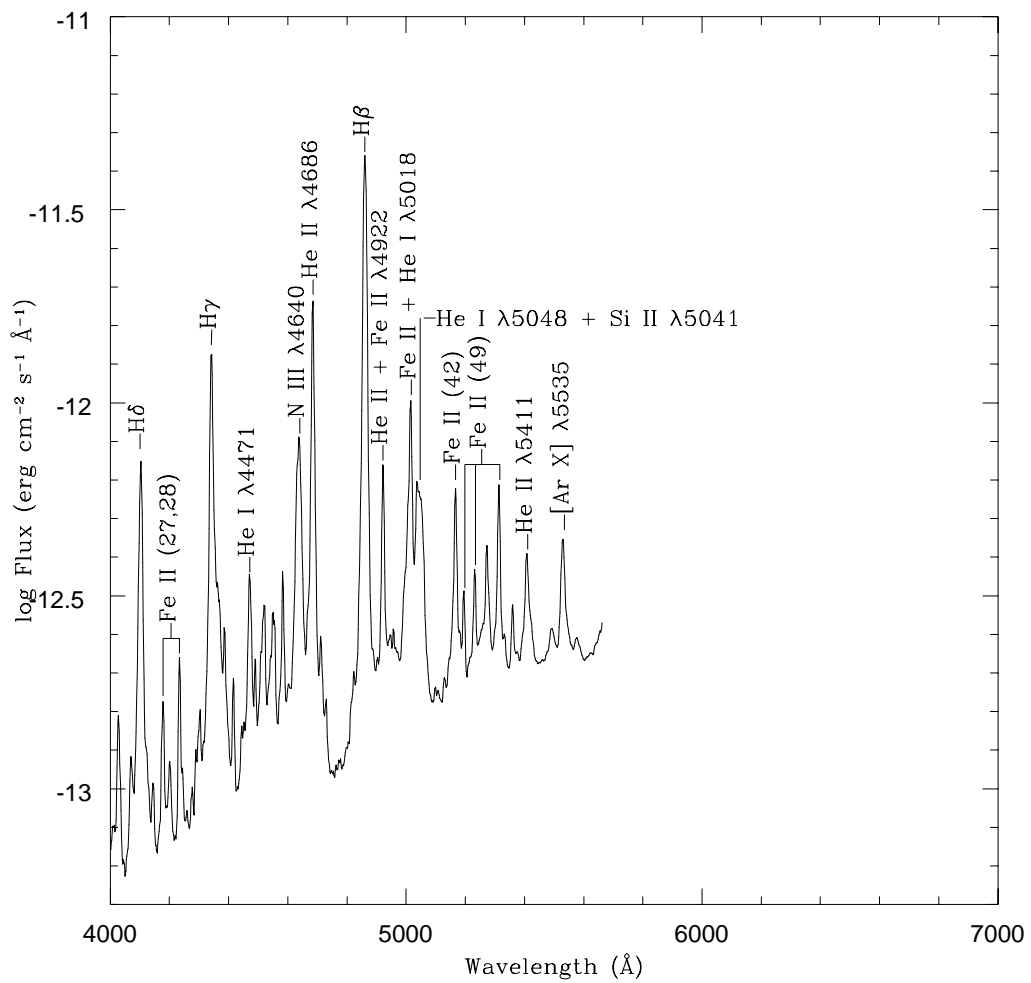


Figure 3.2: Spectral observations of RS Oph on 2006 March 15 ( $t = 31$  days after outburst – see Table 3.1).

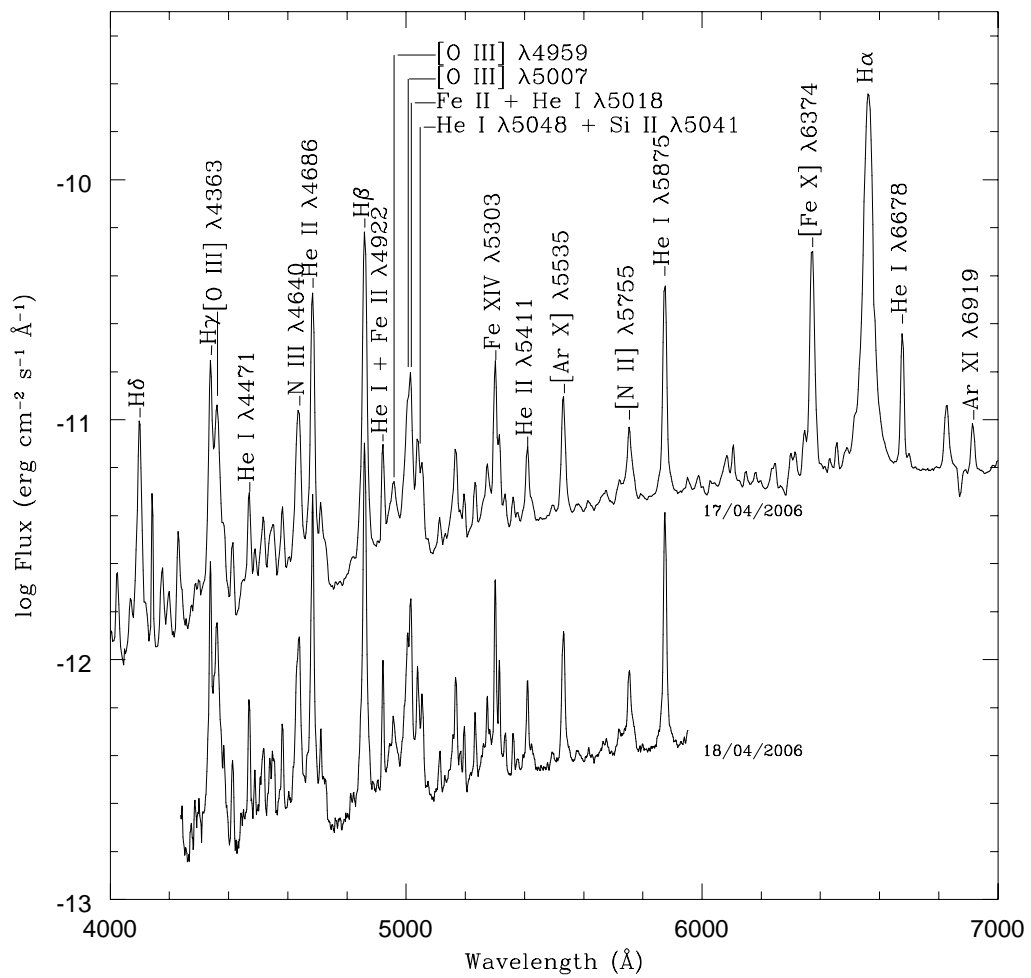


Figure 3.3: As Figure 3.2, but for 2006 April 17 and 18 ( $t = 64\text{--}65$  days after outburst). Note that the day 64 spectrum has been offset in flux by +1 dex for clarity.

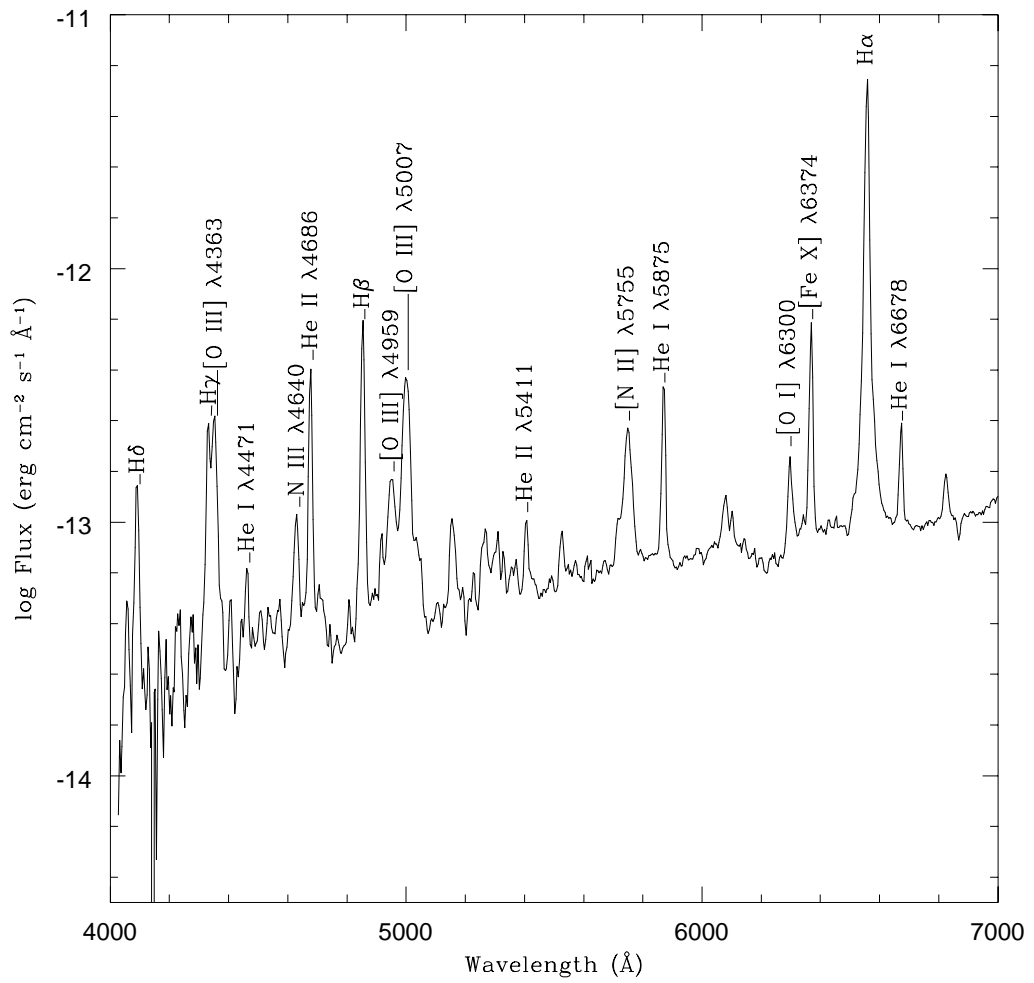


Figure 3.4: As Figure 3.2, but for 2006 May 29 ( $t = 107$  days after outburst).

to distinguish features arising from different parts of the remnant (Figure 3.5). For example, during the months of 2006 February and March (bottom two panels in Figure 3.5, approximately  $\sim 10$  to  $\sim 30$  days after outburst), the emission lines of [O III]  $\lambda 4959$  and  $\lambda 5007$ , He I  $\lambda 5016$  and  $\lambda 5048$ , Fe II  $\lambda 5018$  and [Si II]  $\lambda 5041$  were identified. Immediately it is observed that He I  $\lambda 5048$  and [Si II]  $\lambda 5041$  lines are not strongly present in the spectra in 2006 June and July (top two panels in Figure 3.5). The narrow emission lines are interpreted as arising from the ionized red giant wind ahead of the forward shock, whereas the broad features are associated with the shocked ejecta or the shocked wind (see e.g., Shore et al. 1996).

With the knowledge of the likely origin of various features in the [O III] spectral region, the modelling of the emission line from the expanding remnant alone can be performed (i.e. by ignoring emission from other elements or from the ionized wind – see Section 3.4 below). The line profile modelled in detail is that of 2006 July 30 ( $t = 168$  days) since it was obtained closest in time to our *HST* imaging (top panel Figure 3.5).

### 3.4 Modelling Procedure

Numerical simulations by Lloyd et al. (1993) suggested that bipolarity can be achieved by either (i) the outburst being spherically symmetric and the bipolarity resulting from subsequent interactions with an anisotropic red giant wind or (ii) the outburst itself being intrinsically bipolar, with material being ejected preferentially in the polar directions and then interacting with an isotropic ambient medium. Lloyd et al. (1993) found the latter to be the best-fit to (the admittedly sparse) observations of bipolar structure from VLBI observations of the 1985 outburst of RS Oph.

Sokoloski et al. (2008) suggested that the observed bipolar structure in the radio was not due to an intrinsically asymmetric explosion or to shaping of the ejecta

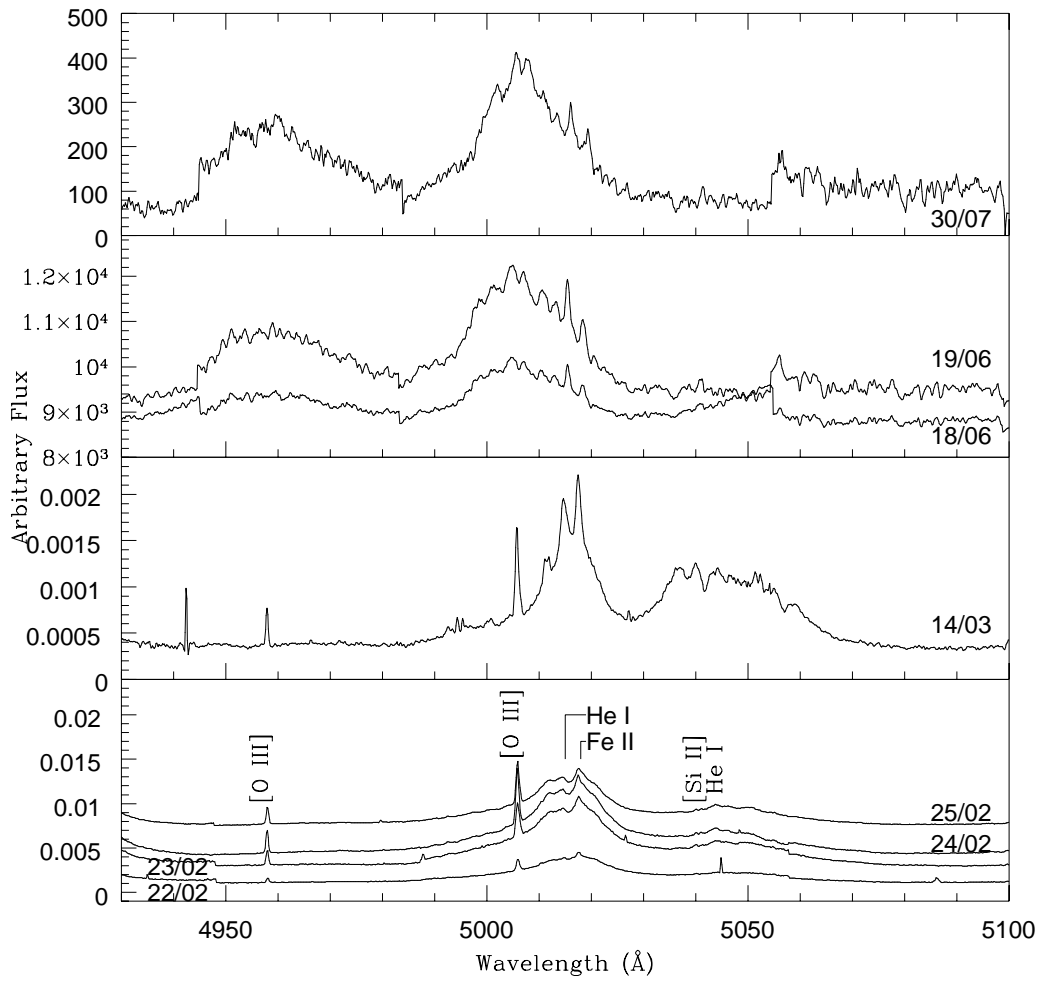


Figure 3.5: RS Oph [O III] spectral evolution at different epochs after the 2006 outburst. From bottom to top, 2006 February, March, June and July (dates as shown). Here the evolution of [O III] can be tracked first as arising from the ionised wind of the red giant (narrow lines in February and March) and then at later times (June and July) it is more likely related to shocked ejecta and/or shocked wind (broad lines). See Table 3.1 for more details of spectroscopic observations.

by circumbinary material but due to collimation at very early times, possibly by the accretion disk. Other authors (Skopal et al. 2008; Banerjee et al. 2009) have modelled the RS Oph outburst by means of Gaussian fitting to line profiles and find several components that are interpreted as arising from different regions of the expanding remnant; namely the central broad component is associated with more slowly expanding material from the waist while the outliers of the lines are associated by these authors with high velocity ejecta.

Here SHAPE (see Chapter 2) was used to analyse and disentangle the 3D geometry and kinematic structure of the expanding nebular emission in RS Oph. It allows modelling of the structure and kinematics of an object to compare with observed images and spectra and includes parameters such as location and width of the spectrograph slit, seeing values and spectral resolutions. At the time of the first epoch *HST* observations the nebular remnant was of course much smaller than the width of the spectrograph slit.

The information described in Section 3.3.1 was used to set initial parameters in SHAPE. These were the derived velocities and structure of RS Oph's extended emission. The emission line of interest, [O III], is very broad and extends beyond the blue cut-off of the *HST* filter (Figure 3.6). Thus, a Doppler filter (Section 2.3.1) was applied to replicate the finite extent of the *HST* narrow band filters (in the case of F502N of the ACS, the central wavelength of the filter, width  $57\text{\AA}$  is  $5022\text{\AA}$  so the sensitivity to material outside the range  $\sim -800$  to  $+2600$  km  $\text{s}^{-1}$  is greatly reduced – see below).

The modelling also determines the nebular remnant inclination and relates this to that of the central binary (where an inclination  $i = 90^\circ$  corresponds to the major axis of the bipolar structure or the orbital axis of the binary lying in the plane of the sky; Figure 1.6). Different authors have suggested that the central binary system has an inclination between  $30^\circ \leq i \leq 40^\circ$  (Dobrzycka & Kenyon 1994) or  $49^\circ \leq i \leq 52^\circ$  (Brandi et al. 2009).

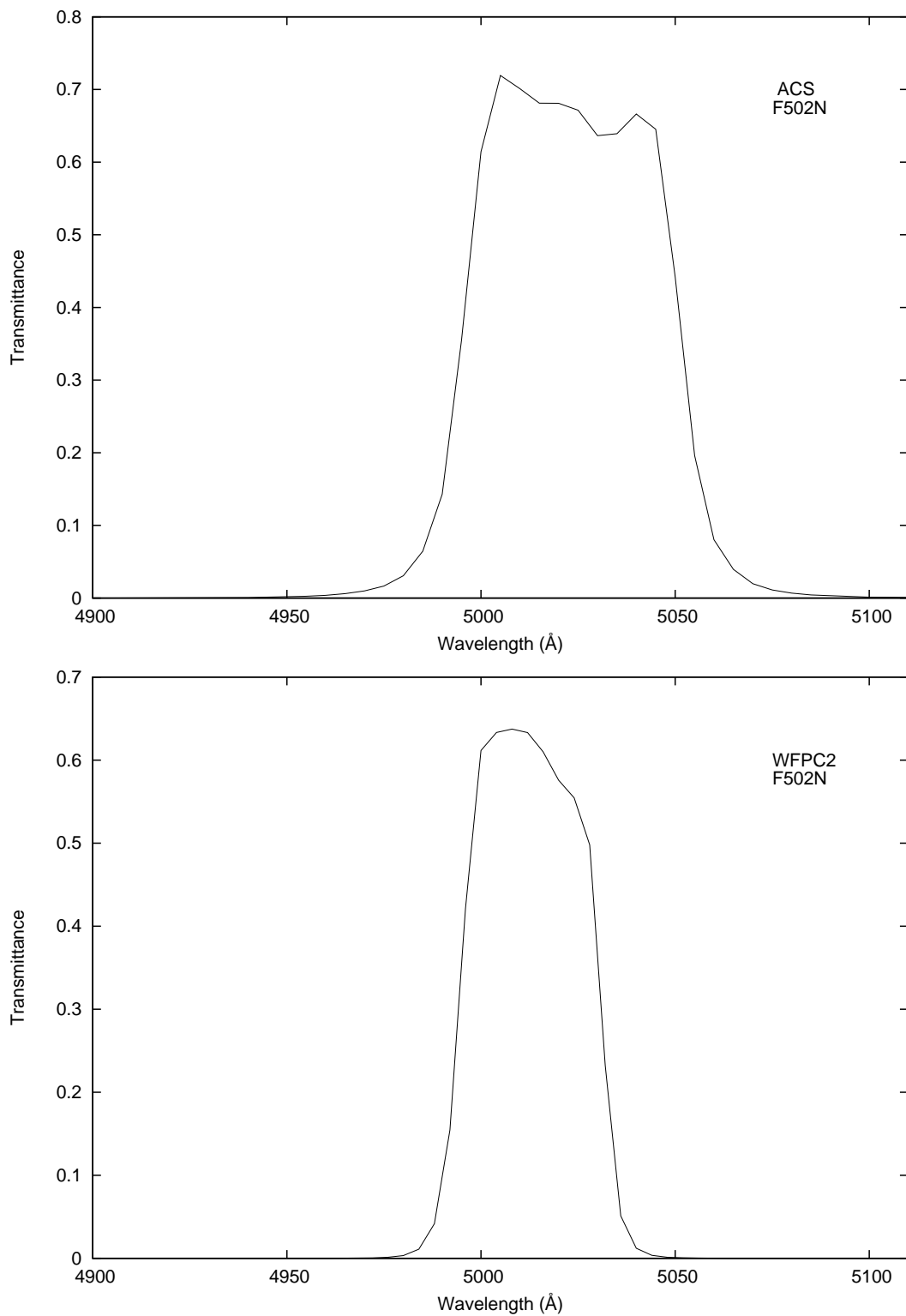


Figure 3.6: *Top* – *HST* ACS/HRC F502N narrowband filter profile centred on 5022Å and with a 57Å FWHM. *Bottom* – *HST* WFPC2 F502N narrowband filter profile centred on 5012Å and with a 27Å FWHM.

## 3.5 Modelling Results

### 3.5.1 General structure

Figure 3.1 suggests that the evolving resolved structure in RS Oph is bipolar and it has been modelled as such by O’Brien et al. (2006) and in Bode et al. (2007). Assuming a bipolar model, the inclination of the system was varied. The velocity field was assumed to be a Hubble-flow type (see Section 2.2.1), given by;

$$V_{\text{exp}} = \frac{3200}{\sin i} \frac{r}{r_0} \text{ km s}^{-1}, \quad (3.1)$$

where  $r$  is the distance of a particle from the centre of the remnant and  $r_0$  is the true semi-major axis. The waist was modelled so that the north-south extent was constrained to  $3.60 \times 10^{15}$  cm in line with that derived in Section 3.3.1 above. In SHAPE a dumbbell structure was first introduced with  $3 \times 10^6$  particles distributed on the surface (as the image suggested the outer lobes were not centrally filled) and the model was run several times to produce a well sampled model spectrum. The model image was then pixelated to replicate the *HST* ACS/HRC CCD pixel size of 0.025 arcseconds.

The model results for this simple geometry (Figure 3.7) do not reproduce the observed spectrum (Figure 3.5). In particular, it gives too broad a line profile, suggesting that lower velocity material must dominate the emission at  $t = 155$  days. Therefore, an over-density was introduced towards the centre containing lower velocity material. This was accomplished via an inner hour glass structure with semi-major axis  $1.26 \times 10^{15} / \sin i$  cm (for  $d = 1.6$  kpc) and with the particles distributed within the volume as the central structure showed no evidence of limb brightening in the *HST* image. A simple spherical geometry was explored for this inner region, but the fits to the observed spectra were then much poorer in terms of the gross line profile (inverted U-shape; Figure 2.2) and finer detail (no double central peak; Figure 3.5). It should be noted that this inner structure is smaller than the estimated extent of the red giant wind at this epoch.

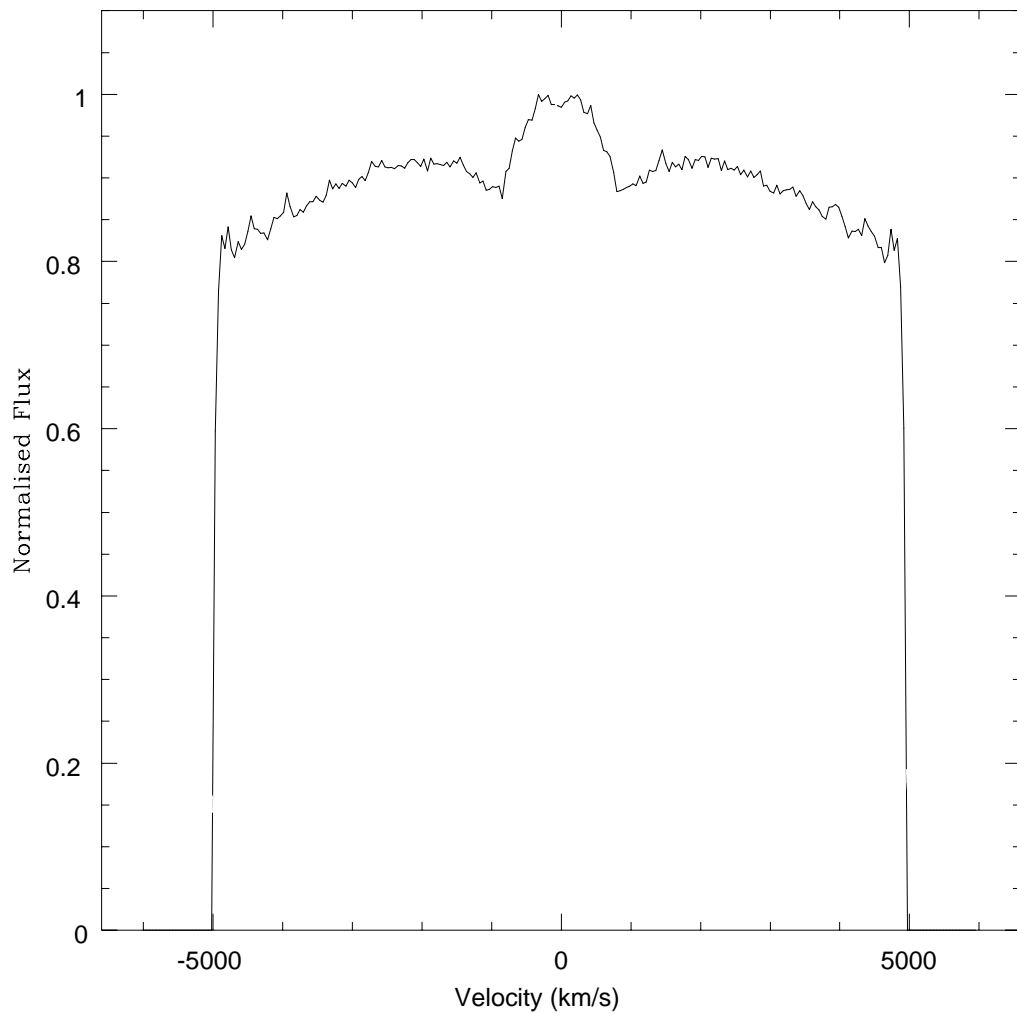


Figure 3.7: Synthetic spectrum for a dumbbell structure with surface distribution. Note the fine structure is not real, but due to the finite number of particles used in the model (see also section 2.2.3).

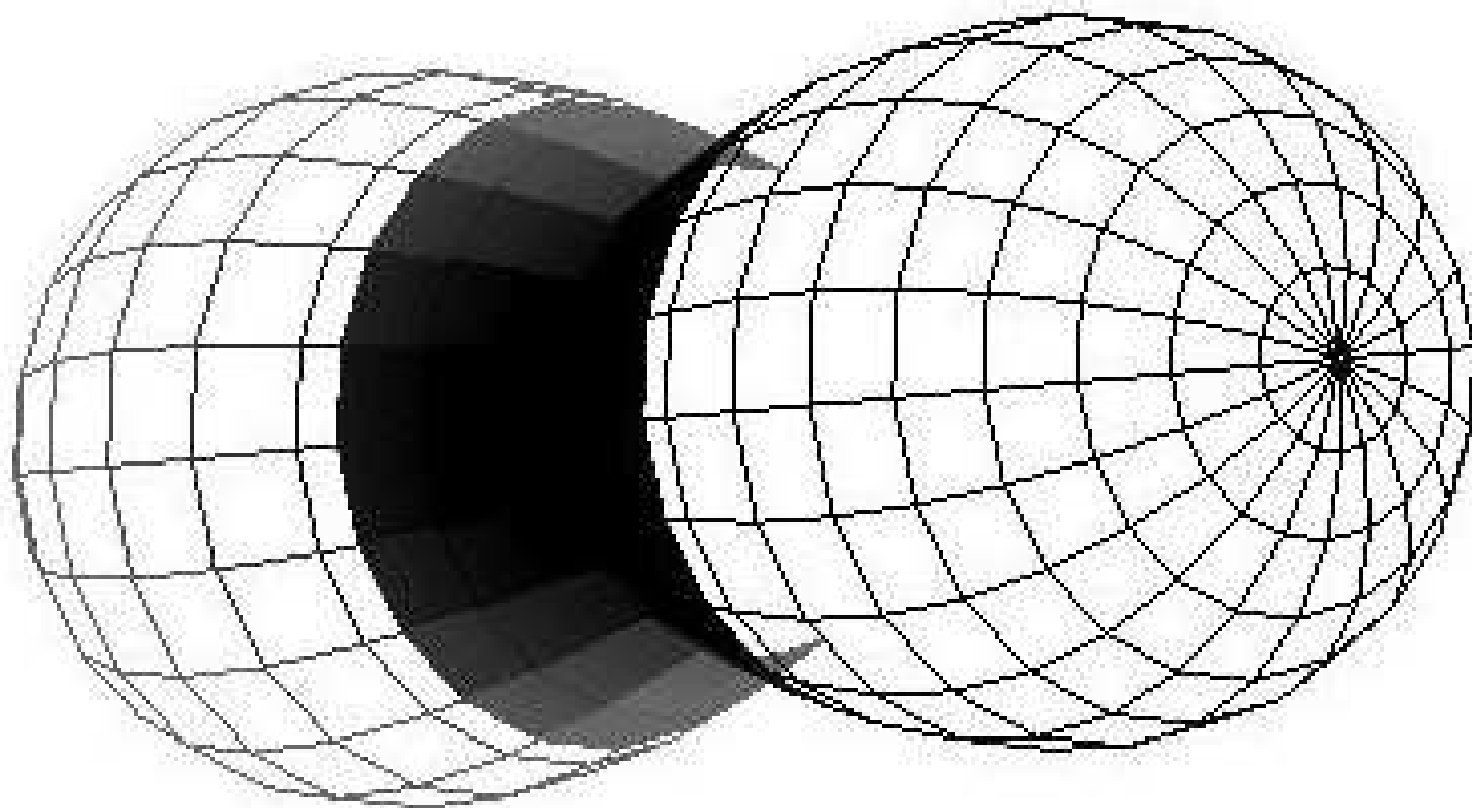


Figure 3.8: Dumbbell (outer) and hour glass (inner) structure that is used to replicate the RS Oph remnant.

The model system thus contains two structures with the central hour glass having four times more emitting particles than the outer dumbbell structure (Figure 3.8); this ratio is in approximate agreement with the estimated ratio of flux from the inner region of the image to that in the lobes (factor of 4; likely to be a lower limit for this ratio as some of the flux in the central region will be contributed by the innermost parts of the outer structure).

The existence of a distinctly two component structure is compatible with early infrared interferometry (Chesneau et al. 2007; Chesneau 2008), and radio observations of a central peak (thermally dominated) and outer lobes (non-thermal; Taylor et al. 1989; Sokoloski et al. 2008; Eyres et al. 2009). In addition, Vaytet et al. (2010) modelled the early-time X-ray spectra of RS Oph and found that they also required a density enhancement towards the central regions to give a high enough absorbing column.

### 3.5.2 System orientation

Figure 3.9 shows the results of modelling using the outer dumbbell and inner hour glass structures described above. The model image reproduces well the general morphology seen in the *HST* image, including that of the west side appearing less prominent than the east. This asymmetry is an observational effect, due to the finite wavelength range, and offset from the [O III] 5007Å rest wavelength, of the *HST* F502N filters' effective transmission (as illustrated in Figures 3.6 and 3.9; see also Sections 2.3.1 and 3.4 above) and immediately shows that the western lobe is approaching the observer. Indeed, any apparent disagreements between the model and observed images can largely be attributed to artifacts of the PSF subtraction procedure. The spectrum also shows excess emission on the blueward side (top Figure 3.5). This could be attributed to Fe II  $\lambda$ 5001.91, although this line is not observed in spectra at earlier times (Figure 3.5).

Although radio observations led O'Brien et al. (2006) to model the RS Oph remnant as a bipolar structure, the deduced orientation of the system differs from

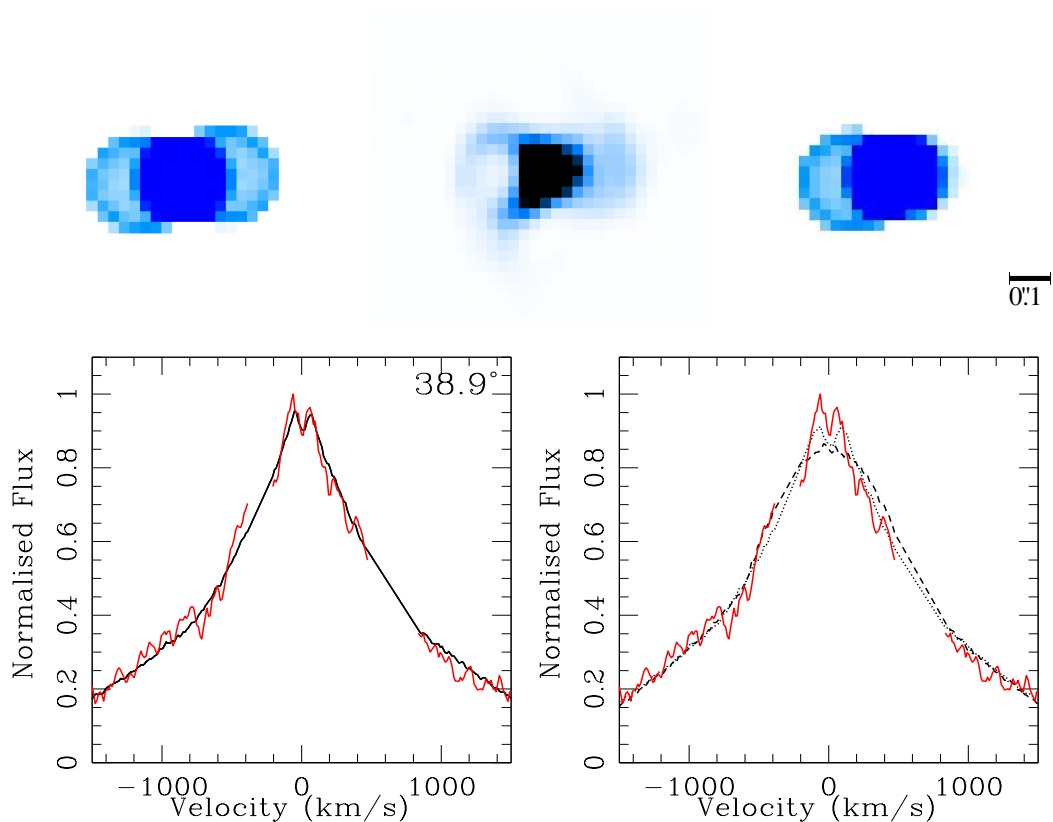


Figure 3.9: *Top* - Synthetic image without the Doppler filter applied (left), enlarged *HST/ACS* image at  $t = 155$  days (middle) and synthetic image with Doppler filter applied (right). The colours have been inverted compared to Figure 3.1. The synthetic images are from a combined outer dumbbell and inner hour glass structure inclined at 39 degrees to the line of sight and with a position angle of  $85^\circ$ . *Bottom* - Best fit synthetic spectrum (black; left) is overlaid with the observed spectrum (red; the emission lines of  $\text{Fe II } \lambda 5001.91$ ,  $\text{He I } \lambda 5015.68$  and  $\text{Fe II } \lambda 5018.44$  associated with the ionized wind ahead of the forward shock have been removed). Model spectra resulting from inclination angles at the  $1\sigma$  error limits are also shown (right) where the dotted line is for  $i = 40^\circ$  and the dashed line is for  $i = 29^\circ$ .

that found here, in the optical. O’Brien et al. (2006) modelled the orientation with the east lobe closest to the observer since that is where a second component appears first in their radio observations at early times. However, the observations here suggest that the west lobe must be approaching the observer. This is in agreement with results from infrared interferometry at early times and it is suggested that the early emergence of the eastern-most radio lobe may be due to obscuration by a flared disk of circumbinary material lying in the orbital plane (Chesneau et al. 2007; Chesneau 2008). Even at the epoch of the first VLBI observation, this material has to be external to the binary and would therefore arise from an anisotropic red giant wind. The system has a position angle on the sky of  $85^\circ$  in line with that found from the radio observations of the 1985 outburst by Porcas et al. (1987).

### 3.5.3 System inclination

If the nebula’s orientation is linked to that of the central binary, and with the knowledge that RS Oph is not an eclipsing system, the upper limit of  $i$  can be determined. For an eclipsing binary with an M2 III giant with a radius of  $67_{-16}^{+19} R_\odot$  (Dumm & Schild 1998) and a separation between the giant and WD of  $1.05 \pm 0.06 \times 10^{13}$  cm (Fekel et al. 2000) eclipses will occur if  $i \geq 64_{-7}^{+6}$  degrees. A lower limit for the range over which  $i$  was explored was also constrained by velocities being far too high to arise from a nova explosion; e.g., at  $i = 20^\circ$ ,  $V_{\text{exp}} = 9300 \text{ km s}^{-1}$ . Therefore the model was run between  $20^\circ \leq i \leq 70^\circ$  and determined each model’s respective  $\chi^2$  fit by comparing the observed and model spectra.

The best-fit value for the inclination of the remnant was determined to be  $i = 39_{-10}^{+1}$  degrees (Figure 3.10; the errors were determined in the standard way by taking the  $\Delta\chi^2$  and calculating the  $1\sigma$  level). This is in good agreement with the inclination for the central binary found by Dobrzycka & Kenyon (1994) of  $30^\circ \leq i \leq 40^\circ$ , though less so with the more recent determination of  $49^\circ \leq i \leq$

52° by Brandi et al. (2009). For illustration, Figure 3.9 also shows the synthetic spectra derived at the error limits quoted for the inclination where clearly the synthetic line profiles do not reproduce as well the observed profiles as does the best fit value of  $i = 39^\circ$ . It should be noted again that lines of Fe II  $\lambda 5001.91$ , He I  $\lambda 5015.68$  and Fe II  $\lambda 5018.44$  have been removed from the observed spectrum prior to model fitting to ensure that our spectral fits are only to the [O III] line itself.

### 3.5.4 Second epoch *HST* observations ( $t = 449$ days)

Using the built-in time evolution option in SHAPE, first a simple linear expansion from the first to the second epoch was explored using the results found in Section 3.4. In this case, the effective wavelength (5012Å) being much less offset from the rest wavelength of the [O III] line itself for the same filter in the ACS means that the asymmetry in the resulting image introduced by the Doppler cuts is not as marked as it was for the first epoch (ACS) image (Figure 3.6).

Fitting to the second epoch image (Figure 3.11), little resemblance is evident between the observed image and a purely linearly expanded modelled image. This is an important result because it implies that the second epoch is not just a linear expansion of the first, at least in the central regions. Then the dumbbell structure was allowed to expand linearly but the inner hour glass was kept the same size as in the first epoch (right image in Figure 3.11). The linear expansion of the outer structure may be understood if, as calculated above, it had already cleared the pre-existing red giant wind by the first epoch. Alternatively, the apparent constant expansion rate may be consistent with powering by narrow jets as proposed by Sokoloski et al. (2008). The apparent constancy of the inferred size of the innermost hour glass structure is more difficult to understand. However, caution should be exercised of over-interpretation of the poorer image from the second epoch, plus the lack of contemporaneous optical spectroscopy to aid the modelling. Although the model reproduces some other features of the second epoch

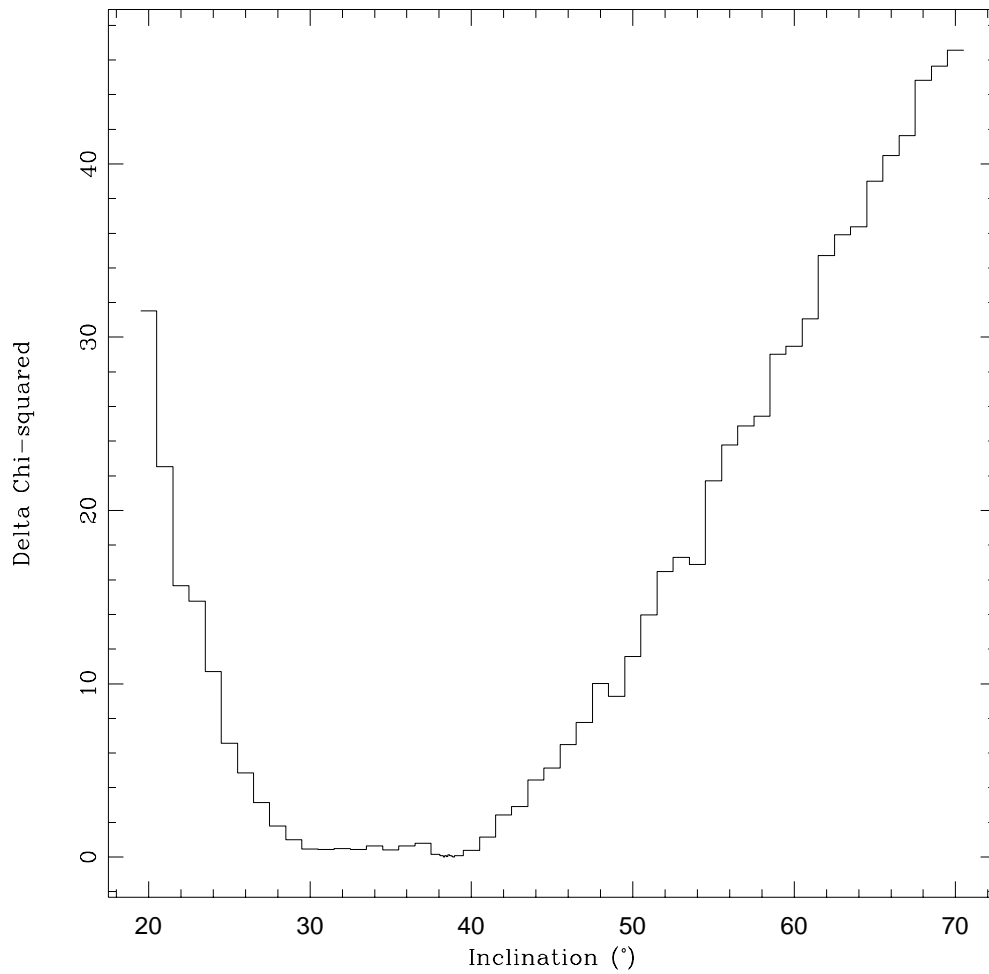


Figure 3.10:  $\Delta\chi^2$  as a function of inclination angle. This reveals that the best-fit value for the inclination of the system is  $39_{-10}^{+1}$  degrees ( $1\sigma$  errors;  $3\sigma$  errors are  $+8^\circ$  and  $-14^\circ$ ). The inclination was varied in  $1^\circ$  steps and then, when close to the minimum, in  $0.1^\circ$  steps.

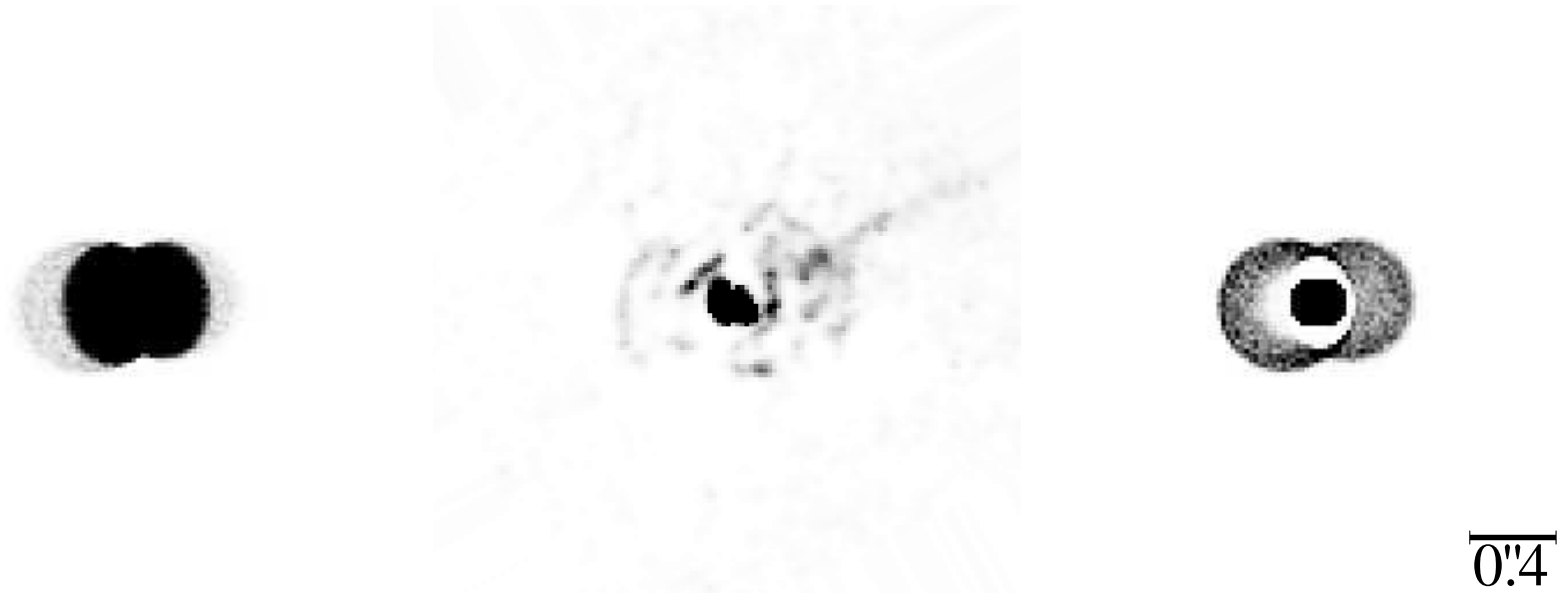


Figure 3.11: *Left* - results from a linear expansion of the first epoch model. *Middle* - *HST*/WFPC2 image at  $t = 449$  days. *Right* - result from a model in which the outer dumbbell structure was expanded linearly but the central hour glass was kept the same size as in the first epoch. The model images have Doppler cuts applied at around  $-1600 \text{ km s}^{-1}$  and  $+2300 \text{ km s}^{-1}$  as appropriate for the WFPC2 filter. Note what appears to be extended emission, in the north west direction in the deconvolved *HST* image. However, this appears to be an artifact most likely due to over exposure (see Section 3.6 for details). North is up and east is to the left.

observations, for example the gap in the east lobe due to the applied Doppler filter which has cut out detection of high velocity material, further investigation is required.

### 3.6 Extended X-ray Emission

X-rays observations taken with the *Chandra* X-ray Observatory one and a half years after the 2006 outburst revealed a narrow, extended structure (Figure 3.12; Luna et al. 2009). Although the feature is consistent with the readout direction of the *Chandra* ACIS-S CCD detector, extensive testing performed by Luna et al. (2009) suggests that the feature is not an artifact. The length of this structure suggests an average expansion rate in the plane of the sky of  $\sim 2.3 \text{ mas day}^{-1}$ , which corresponds to velocities in the plane of the sky of  $\sim 6300 \pm 1600 \text{ km s}^{-1}$  (days/1.6 kpc). It was expected that from the strong shocks moving at these high speeds to produce hard X-ray emission. However, only soft X-ray emission was observed.

The narrow feature, if real, may be explained. For example, Orlando et al. (2009) model shocks preferentially propagating in the direction perpendicular to the plane of the binary. As Luna et al. (2009) point out the position of the red giant at the time of the outburst (from Brandi et al. 2009) would mean this extension to be in the north-south direction. Therefore, they interpreted their results as suggesting that either the orbital solution for RS Oph needed to be re-examined or that the explosion somehow ejected X-ray emitting plasma in a direction that was neither perpendicular to the plane of the orbit nor along the line joining the WD and the red giant.

Also shown in Figure 3.12 is the contour of the RS Oph *HST* second epoch image (Figure 3.11) where the images were matched by the brightest pixel. A few points should be made about Figure 3.12; (a) the sizes of the east-west extents are different; (b) the *HST* artifact and extended X-ray emission seem to lie in the

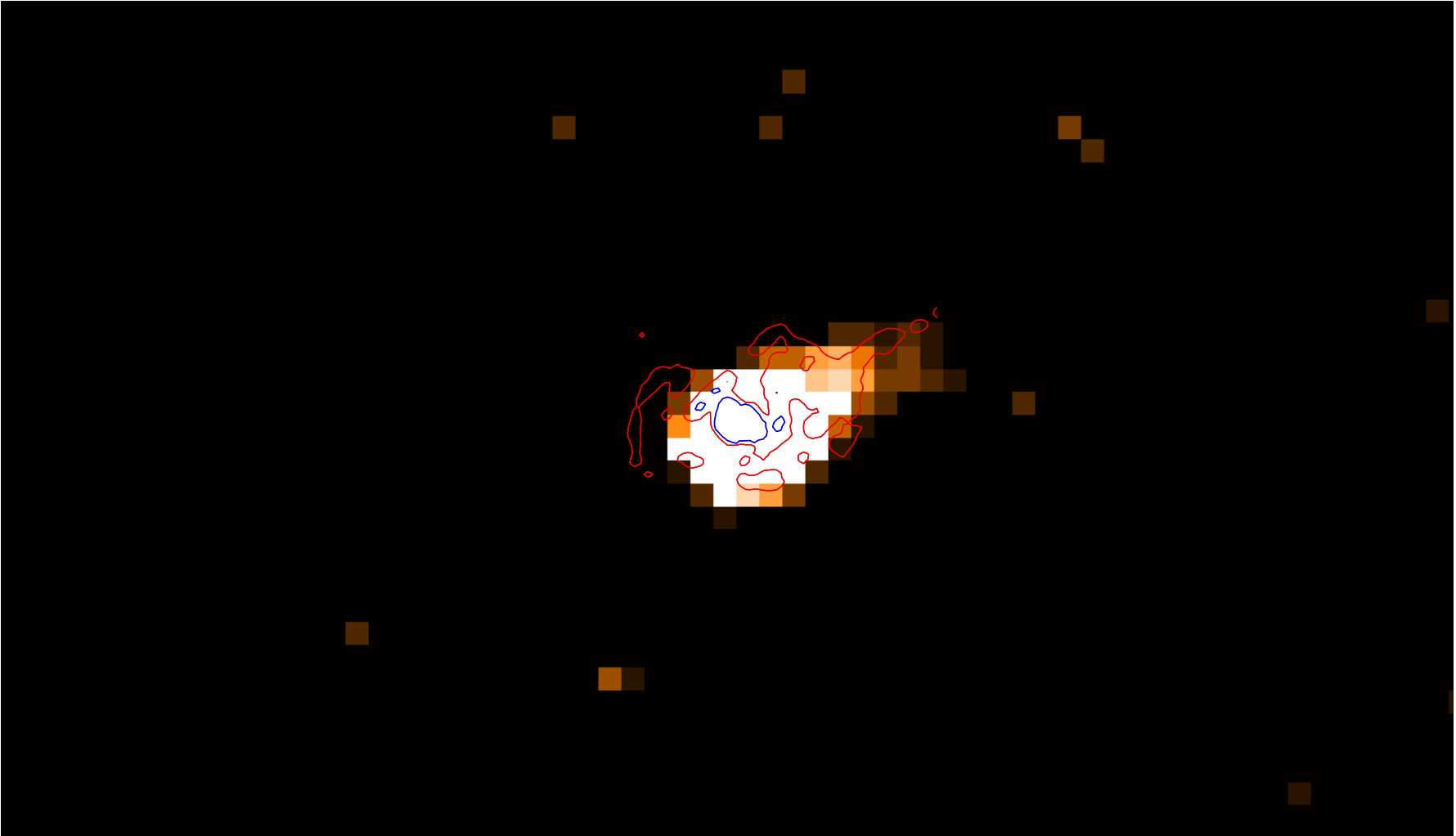


Figure 3.12: *Chandra* image (from Luna et al. 2009) overlaid with the second epoch *HST* image. The contours are for the *HST* image. The images were overlaid so that the brightest pixels matched.

same direction. A discussion of each point is presented below:

- The east-west extent – assuming that the brightest pixel is indeed the centre of the binary, the X-ray image should be larger than the optical image, since it was demonstrated that the east-west direction presented a linear expansion (Section 3.5.4). The expected size at the epoch of the *Chandra* image (539 days after outburst) should be  $\sim 1300$  mas, while the observed size of the *Chandra* image in Figure 3.12 is clearly much larger. This discrepancy between the expected size of the *Chandra* image might point to the fact that taking the brightest pixel is not correct.
- To establish that the optical feature in Figure 3.11 is an artifact, also in the readout direction of the *HST* ACS/HRC CCD, a raw image is shown in Figure 3.13 which shows extended features clearly from nearby warm pixels. The artifact shows up more clearly for RS Oph when the images are processed.

The reality of the extended feature is therefore questionable. However, to add to the debate over the reality of the *Chandra* ‘jet’, which may not be detected in the optical, R Montez (private communication) used *Chandra* observations at a later epoch and found an expansion rate which is comparable with those found here.

## 3.7 Discussion

Using a combination of resolved imaging and ground-based spectroscopy the evolution of the nebular remnant of RS Oph was followed in great detail. Modelling of this evolution has provided the most realistic morpho-kinematical model and helped constrain important physical parameters of the system.

This work suggested a model system comprising two structures, a central hour glass over-density and outer dumbbell structure. The ratio of the deprojected major to minor axes was determined as 3.85. The morphology presented here

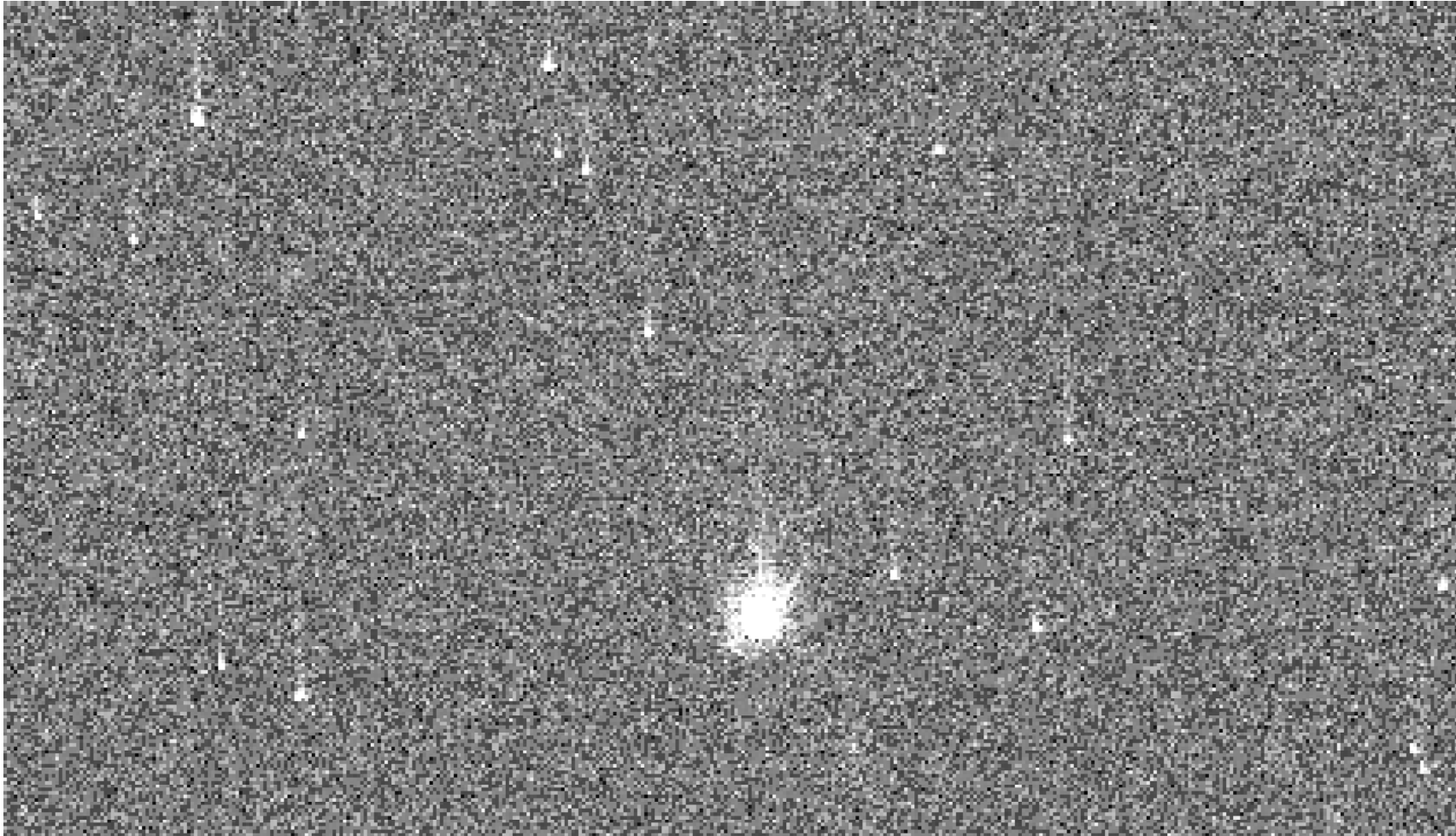


Figure 3.13: *HST* WFPC2 raw image for an area around the RS Oph remnant (bright source). The read-out direction is from bottom to top.

suggests that remnant shaping in RS Oph may happen due to the interaction with the pre-existing anisotropic red giant wind. Mastrodemos & Morris (1999) expect that from a fast wind, as that from the red-giant in RS Oph, equatorial density enhancements are formed for separations  $< 7$  AU. However, Mastrodemos & Morris (1999) models demonstrate pre-existing wind anisotropy that may shape the remnant as suggested above.

The asymmetry observed in the first epoch image is attributed to the narrow band ACS/HRC filter which due to the high expansion velocity of RS Oph cuts out detection of high speed material on the blue side of the spectra. This led to the conclusion that the west lobe is approaching the observer, consistent with results found by Chesneau (2008).

The inclination of the system was derived as  $39_{-10}^{+1}$  degrees and a maximum expansion velocity of the system, following Equation 3.1, as  $5100_{-100}^{+1500}$  km s $^{-1}$  (the range of values for the velocity are associated with the  $1\sigma$  errors on the inclination). This inclination is compatible with estimates of inclination of the central binary, adding weight to the proposed shaping by pre-existing circumbinary material.

The model when evolved to a later epoch suggested that some of the centrally located material might have suffered some deceleration, while the outer dumbbell structure expanded linearly.

In the next Chapter the structure derived here is applied to V2491 Cyg, another RN candidate, along with comparisons to other structures observed in CN systems in order to determine the properties of the expanding nebula and potentially the central binary system in the nova.

# Chapter 4

## The Morphology of the Expanding Ejecta of Nova V2491 Cygni<sup>1</sup>

### 4.1 Introduction

Nova Cygni 2008 N.2 (hereafter, V2491 Cyg) was discovered on 2008 April 10.8 UT (taken as  $t = 0$ ) at about 7.7 mag on unfiltered CCD frames (Nakano et al. 2008) and its nature confirmed spectroscopically yielding velocities of  $\sim 4500$  km s<sup>-1</sup> (H $\alpha$  FWHM, Ayani & Matsumoto 2008). Henden & Munari (2008) identified USNO-B1.0 1223-042965 as the likely progenitor system (within 0.9 arcsec of V2491 Cyg). An archival search by Jurdana-Sepic & Munari (2008) of the Asiago Schmidt telescope images of the progenitor collected over the period 1970-1986 showed no previous outburst. Munari et al. (2011b) have provided a detailed study of the photometric and spectroscopic evolution of V2491 Cyg, including a photo-ionization analysis of the ejecta and their chemical abundances. They derived the reddening for V2491 Cyg of  $E(B - V) = 0.23 \pm 0.01$ , a distance of 14 kpc, and  $V = 17.9$ ,  $R_c = 17.5$ ,  $I_c = 17.1$  for the progenitor in quiescence.

---

<sup>1</sup>The work presented in this Chapter was published in (Ribeiro et al. 2010).

Figure 4.1 shows the light curve for the first 50 days after outburst from the AAVSO. A rapid decline is observed for the first 10 days after outburst and then a sudden rebrightening peaking around day 15. It is not fully understood why this rebrightening should happen. For example, Hachisu & Kato (2009) have modelled the rebrightening by introducing magnetic activity as an additional energy source to nuclear burning. Although, a magnetic WD has a spin closely related to the binary orbital period (King et al. 1990), taken by several authors as 0.0958 days (Baklanov et al. 2008), but there is no observed evidence of a short periodicity in the X-rays related to the supposed orbital period (Ibarra et al. 2009; Page et al. 2010) and generally polars are weak X-ray sources (King & Watson 1987). It is also noteworthy that Baklanov (private communication) does not believe that the above period is related to the orbital period of the system, a matter that is addressed in Darnley et al. (in preparation).

V2491 Cyg is of particular interest because it was detected as an X-ray source pre-outburst (Ibarra & Kuulkers 2008; Ibarra et al. 2008, 2009). This is only the second CN to be detected in X-rays pre-outburst (after V2487 Ophiuchi; Hernanz & Sala 2002). V2487 Oph was originally suggested to be a RN due to its rapid decline in the optical domain and the presence of a plateau phase during decline (see, e.g., Hachisu et al. 2002; Hernanz & Sala 2002). V2487 Oph's true recurrent nature came to light only after a search of the Harvard College Observatory archival photographic collection revealed an outburst on 1900 June 20 (Pagnotta et al. 2009). They used two methods to determine a recurrence timescale of order  $\sim 20$  years, a Monte Carlo simulation to calculate the probability that a given recurrence timescale would produce exactly two discovered eruptions and by directly estimating the most likely number of eruptions. Furthermore, V2491 Cyg has very similar properties to the suggested extragalactic RN M31N 2007-12b, which was shown to have similar magnitude and colour to the RN RS Oph at quiescence (Bode et al. 2009a). On the other hand, Ibarra et al. (2009) derived 0.2–10 keV X-ray luminosities ranging from  $10^{34} - 4 \times 10^{35}$  erg s $^{-1}$  implying inter-outburst mass accretion rates in the range of  $10^{-9}$  to  $10^{-8}$  M $_{\odot}$  yr $^{-1}$  for a 1 M $_{\odot}$

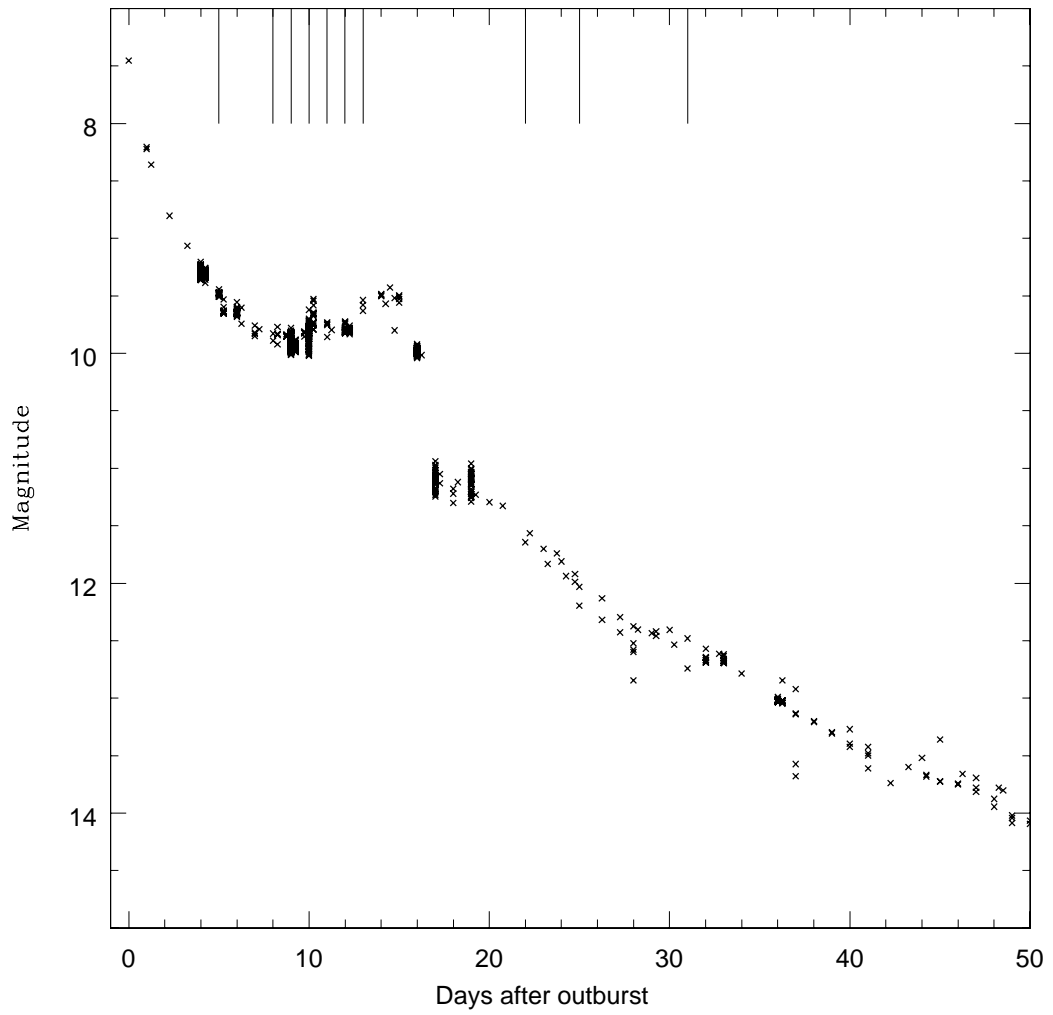


Figure 4.1: Optical light curve for V2491 Cyg from AAVSO data. The vertical lines are days where data were taken with the Meaburn Spectrograph on the 2m robotic Liverpool Telescope.

WD. Such low values for the accretion rate would imply a recurrence timescale of  $\gtrsim 100$  yrs (Yaron et al. 2005; Ibarra et al. 2009; Page et al. 2010). However, a higher WD mass will reduce the recurrence time.

Post-outburst *Swift* observations of V2491 Cyg showed a clearly detected X-ray source, although the count rate was almost an order of magnitude fainter than during pre-outburst observations (Page et al. 2010). The post-outburst observations showed three distinct phases: first a hard X-ray emission phase, then a SSS phase and finally the decline of the SSS with the hard component again becoming prominent, since it fades much less rapidly than the SSS emission (Page et al. 2010).

Here spectroscopic data were used to constrain the structure and velocity field for the expanding remnant of V2491 Cyg. In Section 4.2, the observations and data reduction methodology are described. The results are presented in Section 4.3 and then modelled in Section 4.4. In Section 4.5 the results of the modelling are presented and in Section 4.6 the implications of the results are discussed.

## 4.2 Observations and Data Reduction

Optical spectra of V2491 Cyg were obtained with the Meaburn Spectrograph (a thermocooled, Apogee AP7p 512×512 pixel thinned Tektronix array prototype fibre-fed robotic spectrograph, now superseded by FRODOSpec) on the LT sited at the Observatorio del Roque de Los Muchachos on the Canary Island of La Palma, Spain. The spectrograph was fed using a close-packed fibre bundle input array, consisting of  $49 \times 0.8''$  diameter fibres which were reformatted as a slit with the fibres in random order. These were among the first science results to be detailed using a spectrograph on the robotic LT.

The observations were carried out over several epochs from  $t = 5$  days (2008 April 16) to 31 days (2008 May 12) post-outburst. The log of spectroscopic observations is shown in Table 4.1. The spectrograph provided three overlapping fixed grat-

Table 4.1: Log of optical spectral observations for V2491 Cyg.

Date of observation	days after outburst	Exposure time (sec)	Instrument
2008 April 13	2	900.0	Varese-MMS
2008 April 16	5	200.0	Meaburn-LT
2008 April 19	8	200.0	Meaburn-LT
2008 April 20	9	200.0	Meaburn-LT
2008 April 21	10	200.0	Meaburn-LT
2008 April 22	11	200.0	Meaburn-LT
2008 April 23	12	200.0	Meaburn-LT
2008 April 24	13	200.0	Meaburn-LT
2008 April 25	14	300.0	SARG-TNG
2008 May 03	22	600.0	Meaburn-LT
2008 May 06	25	600.0	Meaburn-LT
2008 May 12	31	600.0	Meaburn-LT
2008 May 14	33	1800.0	Varese-MMS
2008 July 27	108	900.0	Asiago-AFOSC
2009 July 31	477	7200	Asiago-AFOSC

ing positions, giving complete wavelength coverage from 3900–8000Å. However, only a single grating position (5350–6888Å) is used with dispersion of 3.00 Å/pix and spectral resolving power  $\sim 350$ . Data reduction was performed through a pipeline that initially performs bias, dark frame and flat field subtraction. With a comparison arc spectrum, a third order polynomial 2D wavelength/distortion map was created using the STARLINK Figaro ARC/IARC/ISCRUNCH routines and applied to the object image. Sky subtraction based on identification of non-object areas of the 2D spectrum was then carried out, if significant sky lines were visible, using the Figaro routine POLYSKY. A 1D spectrum was then automatically extracted using the PROFILE and OPTEXTRACT routines. Relative flux correction was accomplished by using observations of a number of early type Be stars (showing few absorption lines) obtained for a different programme. Absorption lines were patched over and the star’s temperature was chosen following their spectral type (Boehm-Vitense 1981). Using the STARLINK Figaro IRFLUX routine the spectra was corrected for instrumental efficiency/atmospheric absorption. Figure 4.2 shows the computed flux-corrected spectra from  $t = 5$  to 31 days after outburst.

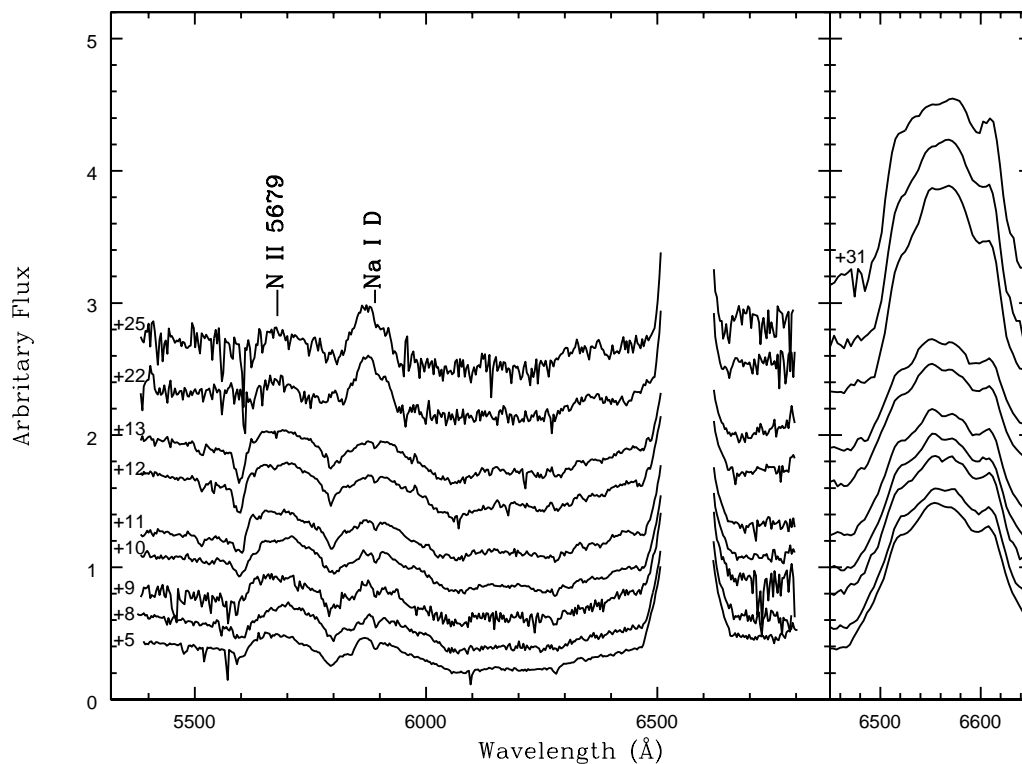


Figure 4.2: Meaburn spectroscopic observations of V2491 Cyg during days 5–31 (2008 April 06 to 2008 May 12). The Meaburn spectra have been corrected for instrumental efficiency/atmospheric transmission using Be Star comparison spectra (see text for details). On the left-hand-side the H $\alpha$  emission has been truncated to show more clearly the lower intensity lines. The spectrum on day 31 after outburst was too noisy at this low level, so only the H $\alpha$  is plotted line. On the right-hand-side the H $\alpha$  line profiles are shown. The time since outburst (in days) is shown to the left of each spectrum. Cosmic rays have also been removed. The higher resolution(non-Meaburn spectrograph) H $\alpha$  profiles in Table 4.1 are shown in Figure 4.4.

Spectroscopic observations were also obtained at  $t = 2, 25, 33, 108$  and  $477$  days after outburst with: (i) the 0.6m telescope of the Schiaparelli observatory in Varese equipped with a multi mode spectrograph and various reflection gratings, (ii) the 3.5m TNG in La Palma and the high resolution spectrograph SARG ( $\Delta\lambda/\lambda = 75000$ ), and (iii) the spectrograph/imager AFOSC on the 1.82m telescope of the Padova Astronomical Observatory in Asiago with wavelength coverage of  $6400\text{--}7050\text{\AA}$ . This is part of the observational monitoring of V2491 Cyg is described by Munari et al. (2011b).

### 4.3 Observational Results

The spectral data were first analysed to get an initial estimate of the component parameters before detailed modelling of V2491 Cyg began. The spectra show broad  $H\alpha$ , nitrogen ( $N\text{ II } 5679\text{\AA}$ ) and sodium ( $\text{Na I D}$ ) lines (Figure 4.2). The spectral monitoring by Munari et al. (2011b) showed that at day 33 after outburst the auroral  $[N\text{ II}] 5755\text{\AA}$  line was still pretty weak, and thus the nebular  $[N\text{ II}] 6458, 6584\text{\AA}$  lines should not yet be perturbing the  $H\alpha$  profile. Also evident is a narrowing of the  $H\alpha$  line profile from day 22 after outburst, which is after the optical rebrightening. It is not possible to say why this rebrightening should happen but it is noteworthy that Munari et al. (2011b) also observed a decrease in the equivalent widths of the  $H\beta$  line. The  $N\text{ II}$  and  $\text{Na I}$  lines are similar to those seen in the early spectrum of V394 CrA (Williams et al. 1991). However, these lines disappear from the spectrum of V394 CrA 20 days after its 1987 outburst. In the case of V2491 Cyg both are clearly present later after outburst. The  $[N\text{ II}]$  line, as in V394 CrA, is most likely due to continuum fluorescence from the post-outburst WD radiation.

The line of interest for detailed analyses is  $H\alpha$  due to its strength compared to those of other lines visible in the spectrum. Furthermore, later in the outburst other emission lines are blended (Munari et al. 2011b). Using the low resolution Meaburn spectra, initially five Gaussian components were fit to the spectra (see

Figure 4.3). This allows the derivation of the individual components' radial velocities and their respective FWHM (see Tables 4.2 and 4.3, respectively). There is evidence for velocity symmetry between the faster moving components, 1 and 5. Components 2, 3 and 4 are much harder to constrain, especially component 3 which becomes stronger after rebrightening. The displacement of the line profile from the rest wavelength of  $H\alpha$ , using components 1 and 5, is suggested to be  $92\pm 36$  km s<sup>-1</sup> which may be the space velocity of the system.

## 4.4 Modelling

Using SHAPE (Version 3.56, see Chapter 2) morpho-kinematical studies of V2491 Cyg were performed. Classical nova ejecta have been modelled with various structures (e.g., Hutchings 1972b; Solf 1983; Gill & O'Brien 1999, see also Chapter 2). Work by Slavin et al. (1995), later updated by Bode (2002), suggested a relationship between the speed class (in terms of the time for the wind flux to decline 3 magnitudes from peak –  $t_3$ ) and the major to minor axis ratio of the expanding nova shell, where the faster the nova the less the degree of shaping. This relationship works well with CNe (short orbital period systems) and possibly RNe of short orbital period. However, RS Oph, a system with orbital period of 455 days (Dobrzycka & Kenyon 1994; Fekel et al. 2000; Brandi et al. 2009), at 155 days after outburst showed a deprojected major to minor axial ratio of 3.85 (Chapter 3), which considering its fast optical decline would not agree with the relationship originally found by Slavin et al. (1995). However, the mechanism for formation of CN and RN shells, especially those RNe with long orbital periods, is expected to be different. For example, systems such as RS Oph have remnants grossly affected by the interaction of ejecta with the pre-existing red-giant wind, which is unique to this sub-group of RNe (again, see previous Chapter).

Table 4.2: Derived radial velocity for each of the 5 components of the H $\alpha$  line in V2491 Cyg (see Figure 4.3 and text for details).

Date	days after outburst	Component Radial Velocity ( km s <sup>-1</sup> )				
		1	2	3	4	5
2008 April 16	5	-1875±32	-530±34	117±3500	615±64	2028±68
2008 April 19	8	-1860±17	-510±22	112±960	671±61	2085±19
2008 April 20	9	-1899±50	-537±38	98±850	700±28	2088±3
2008 April 21	10	-1828±65	-482±48	99±2500	653±8	1994±53
2008 April 22	11	-1909±76	-531±55	92±1200	687±59	2043±24
2008 April 23	12	-2025±160	-642±93	120±1600	680±87	2072±120
2008 April 24	13	-2054±67	-720±72	90±1300	558±29	2009±65
2008 May 03	22	-1634±47	-610±30	184±29	673±30	2088±26
2008 May 06	25	-1739±220	-716±20	96±33	687±58	2015±44
2008 May 12	31	-1865±92	-822±110	334±91	368±370	2094±5

Table 4.3: Derived FWHM velocity for each of the 5 components of the H $\alpha$  line in V2491 Cyg (see Figure 4.3 and text for details).

Date	days after outburst	Component FWHM Velocity ( km s <sup>-1</sup> )				
		1	2	3	4	5
2008 April 16	5	1729 $\pm$ 47	1357 $\pm$ 24	1870 $\pm$ 3500	1379 $\pm$ 130	1166 $\pm$ 91
2008 April 19	8	1664 $\pm$ 48	1412 $\pm$ 14	1807 $\pm$ 1800	1429 $\pm$ 110	1115 $\pm$ 41
2008 April 20	9	1649 $\pm$ 40	1399 $\pm$ 100	1998 $\pm$ 1200	1488 $\pm$ 57	1050 $\pm$ 27
2008 April 21	10	1658 $\pm$ 100	1239 $\pm$ 53	1995 $\pm$ 2200	1261 $\pm$ 140	1194 $\pm$ 74
2008 April 22	11	1660 $\pm$ 89	1283 $\pm$ 59	2694 $\pm$ 3000	1305 $\pm$ 140	1084 $\pm$ 53
2008 April 23	12	1639 $\pm$ 180	1384 $\pm$ 210	1617 $\pm$ 780	1476 $\pm$ 400	1030 $\pm$ 170
2008 April 24	13	1421 $\pm$ 110	1335 $\pm$ 83	1765 $\pm$ 2100	1364 $\pm$ 170	1127 $\pm$ 92
2008 May 03	22	1340 $\pm$ 60	910 $\pm$ 27	931 $\pm$ 86	1502 $\pm$ 110	806 $\pm$ 40
2008 May 06	25	1232 $\pm$ 260	996 $\pm$ 240	1081 $\pm$ 680	1477 $\pm$ 390	875 $\pm$ 63
2008 May 12	31	1189 $\pm$ 100	1096 $\pm$ 76	1725 $\pm$ 300	1832 $\pm$ 320	795 $\pm$ 26

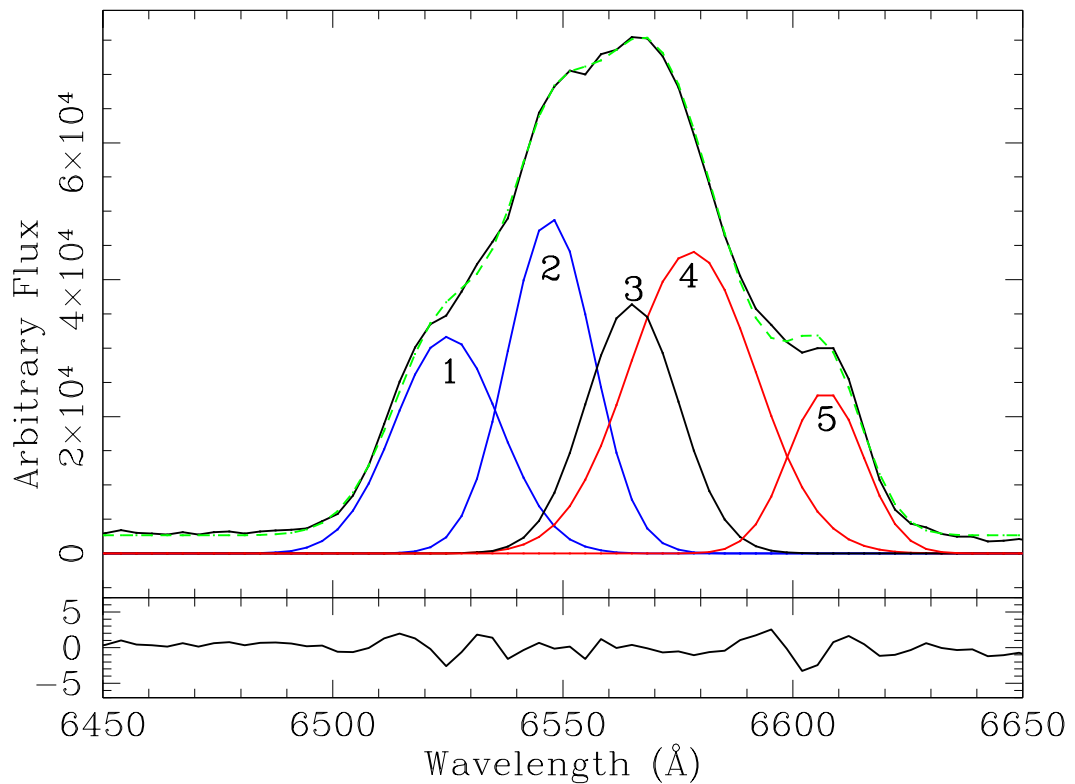


Figure 4.3: Gaussian components best-fit to the observed  $H\alpha$  line profile for V2491 Cyg on day 25 after outburst. The observed spectrum is shown in black and the combined Gaussian components in dashed green. The colour scheme for the individual Gaussian components is just to separate the different components. The component numbers, 1 through 5, are in increasing wavelength of the peak. Also shown are the residuals to the overall fit. The results for the derived radial velocities of each peak and FWHM of each component are presented in Tables 4.2 and 4.3, respectively.

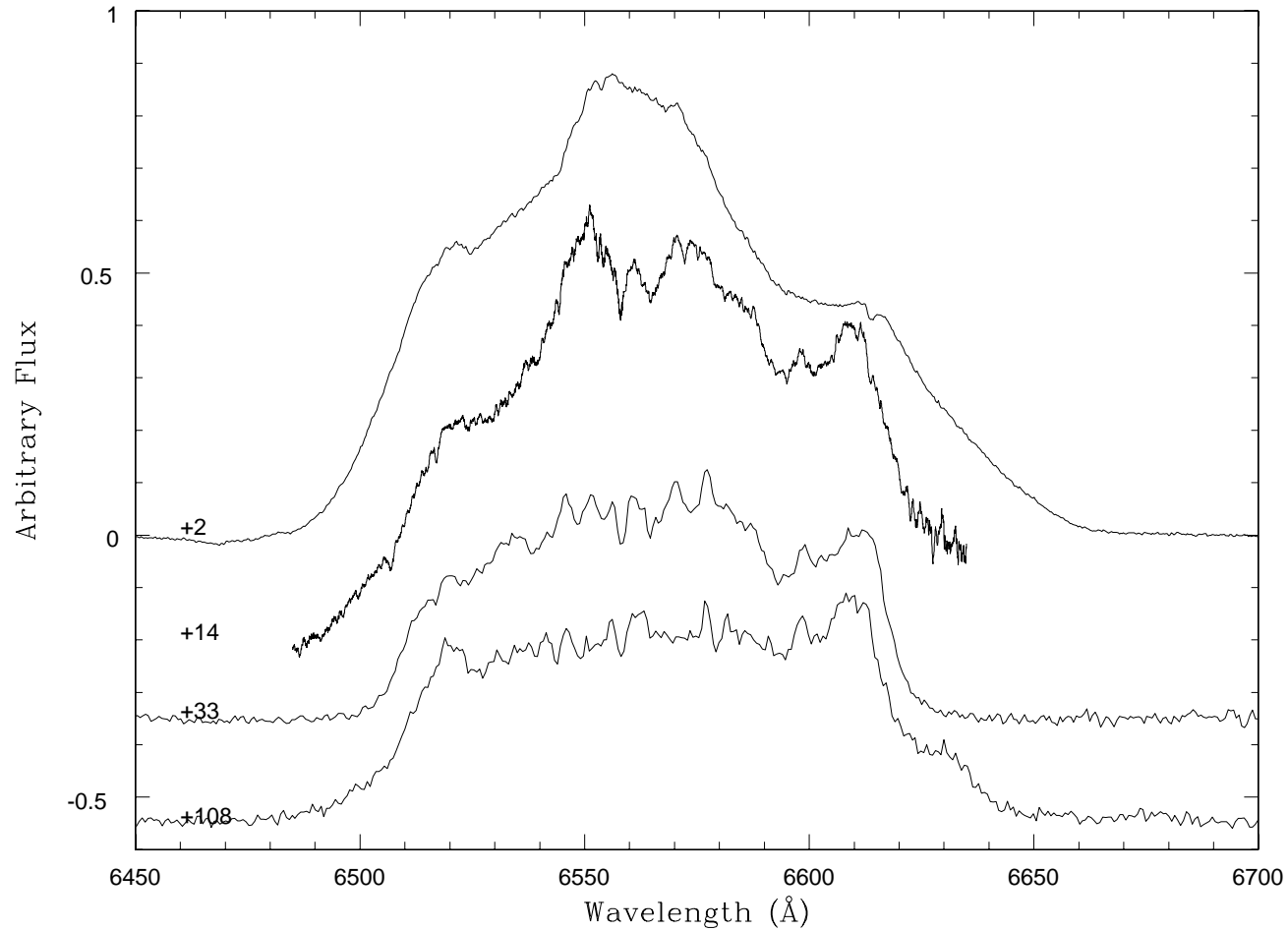


Figure 4.4: Spectral evolution of the high resolution H $\alpha$  line profile from several telescopes as shown in Table 4.1 and in the text. The spectra have been offset and the numbers on the left are days after outburst.

### 4.4.1 Model assumptions

It is desirable when dealing with modelling to reduce computing time and yet have a physically sound model. The modelling of permitted line profiles so early after outburst is complicated by the fact that they are most likely affected by optical depth effects. The full treatment of radiative transfer requires full knowledge of several parameters of the central system and further assumptions are required. For example, the temperature of the ejecta, which can be derived spectroscopically, and the density of each component, which is much harder to derive since an ejected mass and a geometry of the system must be assumed.

The effects of radiative transfer on the line profiles were considered. It was found that the lower the inclination the more the absorption affects the results but the overall line shape does not in fact significantly change from the optically thin case. Furthermore, absorption affects the lower velocity systems more. So when dealing with the results caution is necessary especially with the densities derived from the models because applying a density in the optically thin case will actually be only a lower limit to the true density of a system with greater opacity.

The assumption was also made that at early times the structures are still volume filled. della Valle et al. (2002) have shown the  $H\alpha$  spectral evolution of V382 Vel from early outburst to the nebular stages (5 to 498 days after outburst); at early stages the line profile showed an asymmetric saddle-shape with the blue component more prominent than the red. The blue component diminishes in strength and the whole line profile develops to become a flat-topped shape. They associate this with the termination of the post-outburst wind phase and the complete ejection of the envelope. The higher resolution spectra, shown in Figure 4.4, also show a similar development, and a similar interpretation can perhaps be made here.

### 4.4.2 Model parameters

Given V2491 Cyg’s fast decline from maximum, an axial ratio of 1.15 was assumed for the chosen structures following the relationships in Slavin et al. (1995). The possibility was also considered of a structure similar to RS Oph, first coined “peanut-shaped” (Bode et al. 2007) and later modelled as a dumbbell structure with an hour-glass-shaped central overdensity (Ribeiro et al. 2009, see also Chapter 3). This model is included in the studies described here because, as mentioned before, this system has been suggested as a RN and this morphology has also been suggested for the RN U Sco (Drake & Orlando 2010). The candidate structures chosen are then (i) polar blobs with an equatorial ring (Model A, e.g., HR Del; Hutchings 1972b; Solf 1983); (ii) a dumbbell with an inner hour-glass overdensity with an axial ratio the same as derived above for RS Oph (Model B); (iii) prolate shell with an equatorial ring (Model C); and (iv) a prolate shell with tropical rings (Model D, e.g., V705 Cas; Gill & O’Brien 1999). As noted above, Model B differs from that generated by the common-envelope phase described above because the observed structure could arise due to interaction with a pre-existing red-giant wind and/or collimation by the accretion disc (e.g., Bode et al. 2007; Sokoloski et al. 2008; Ribeiro et al. 2009). The models, as visualised in SHAPE, are shown in Figure 4.5.

The lack of a resolved image of the remnant means any model is not as well constrained as when the structure is spatially resolved (e.g., Chapter 3). However, for the models assumed above, a system inclination (Figure 1.6) was constrained with an expansion assumed to take place in a Hubble flow.

The parameter space from 0–90 degrees was explored together with maximum expansion velocity ( $V_{\text{exp}}$ ) ranging from 100–8000 km s<sup>-1</sup> (in steps of 1 degree and 100 km s<sup>-1</sup>, respectively).  $V_{\text{exp}} > 8000$  km s<sup>-1</sup> are excluded as this is much higher than those normally associated with novae and indeed is at the lower end of velocities found in Type Ia Supernovae (e.g., Livio 2000). However, it is noteworthy that in the helium nova V445 Pup high speed knots were observed moving

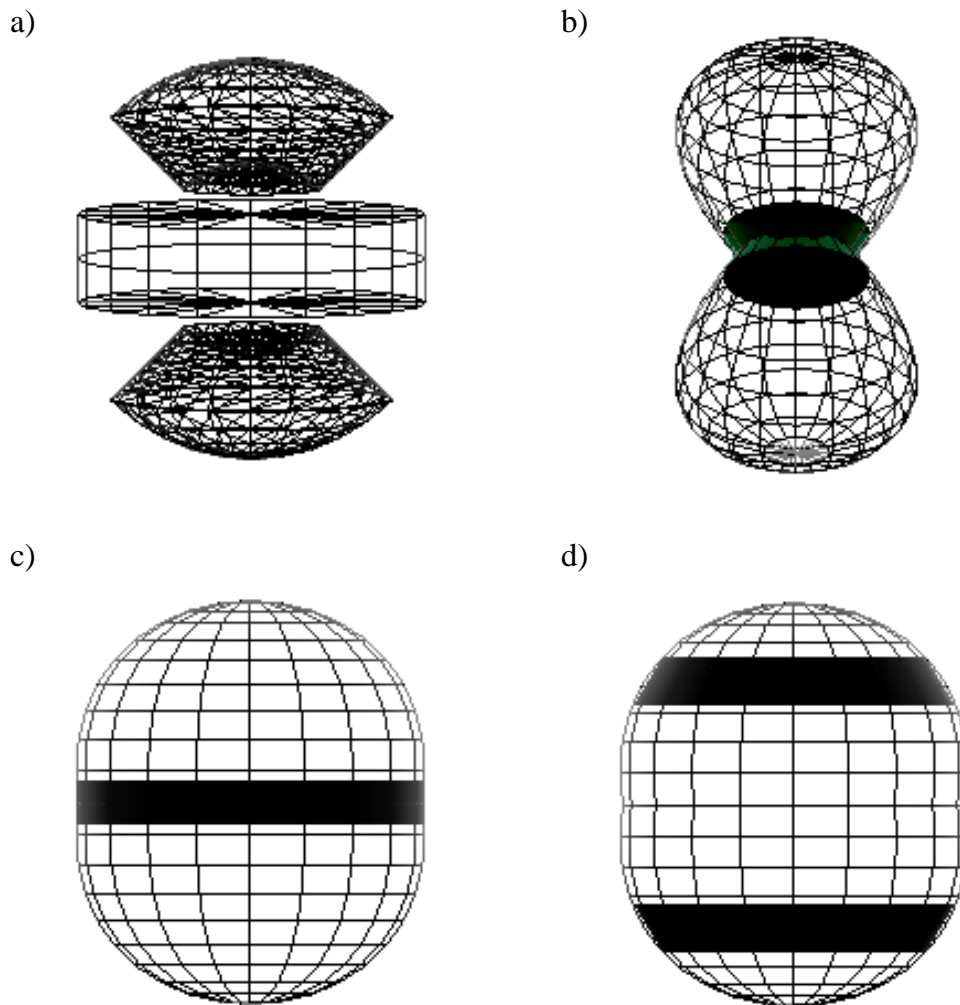


Figure 4.5: Models as visualised in SHAPE. a) polar blobs with an equatorial ring (Model A), b) a dumbbell structure with an hour-glass overdensity (Model B), c) prolate shell with an equatorial ring (Model C) and d) prolate shell with tropical rings (Model D).

at  $8450 \pm 570$  km s<sup>-1</sup> (Woudt et al. 2009). The models were run several times to produce a well sampled model spectrum. The model spectra are compared to the observed spectra and flux matched via  $\chi^2$  minimisation, using techniques from Press et al. (1992). Furthermore, an estimate of the density ratio of each component was derived from their total fluxes using the task SPECFIT in IRAF. These were used as inputs for the relative structure densities.

## 4.5 Modelling Results

### 4.5.1 Early epoch observations ( $t = 25$ days)

Shown in Figure 4.6 are the results of the model fits, and their respective  $1\sigma$  errors, for all the model runs. Panel a) shows the results for Model A. These suggest that the best-fit for this model is an inclination of  $80_{-12}^{+3}$  degrees with maximum expansion velocity,  $V_{\text{exp}}$ , for the polar blobs of  $\sim 3100_{-100}^{+200}$  km s<sup>-1</sup> and for the equatorial ring of  $\sim 2700_{-100}^{+200}$  km s<sup>-1</sup>. The individual component fluxes are about the same. Panel b) shows the results for Model B. These suggest that the best-fit to the model is for a system with inclination  $63_{-8}^{+23}$  degrees and  $V_{\text{exp}}$  of  $3500_{-300}^{+1500}$  km s<sup>-1</sup>. The flux is dominated by the dumbbell component. Panel c) shows the results for Model C. These suggest that the best-fit to the model is for a system with inclination  $50_{-12}^{+33}$  degrees and  $V_{\text{exp}}$  of  $2800_{-200}^{+300}$  km s<sup>-1</sup>. The flux is dominated by the prolate structure. Finally, panel d) shows the results for Model D. These suggest that the best-fit to the model is for a system with inclination  $54_{-21}^{+36}$  degrees and  $V_{\text{exp}}$  of  $2800_{-200}^{+300}$  km s<sup>-1</sup>. The flux is again dominated by the prolate structure.

As previously mentioned these results are not as well constrained as they would be if the spectra were combined with imaging data. A simple sphere was also explored (Figure 2.2). The results suggest that the best-fit maximum expansion velocity  $V_{\text{exp}} \sim 2700$  km s<sup>-1</sup>.

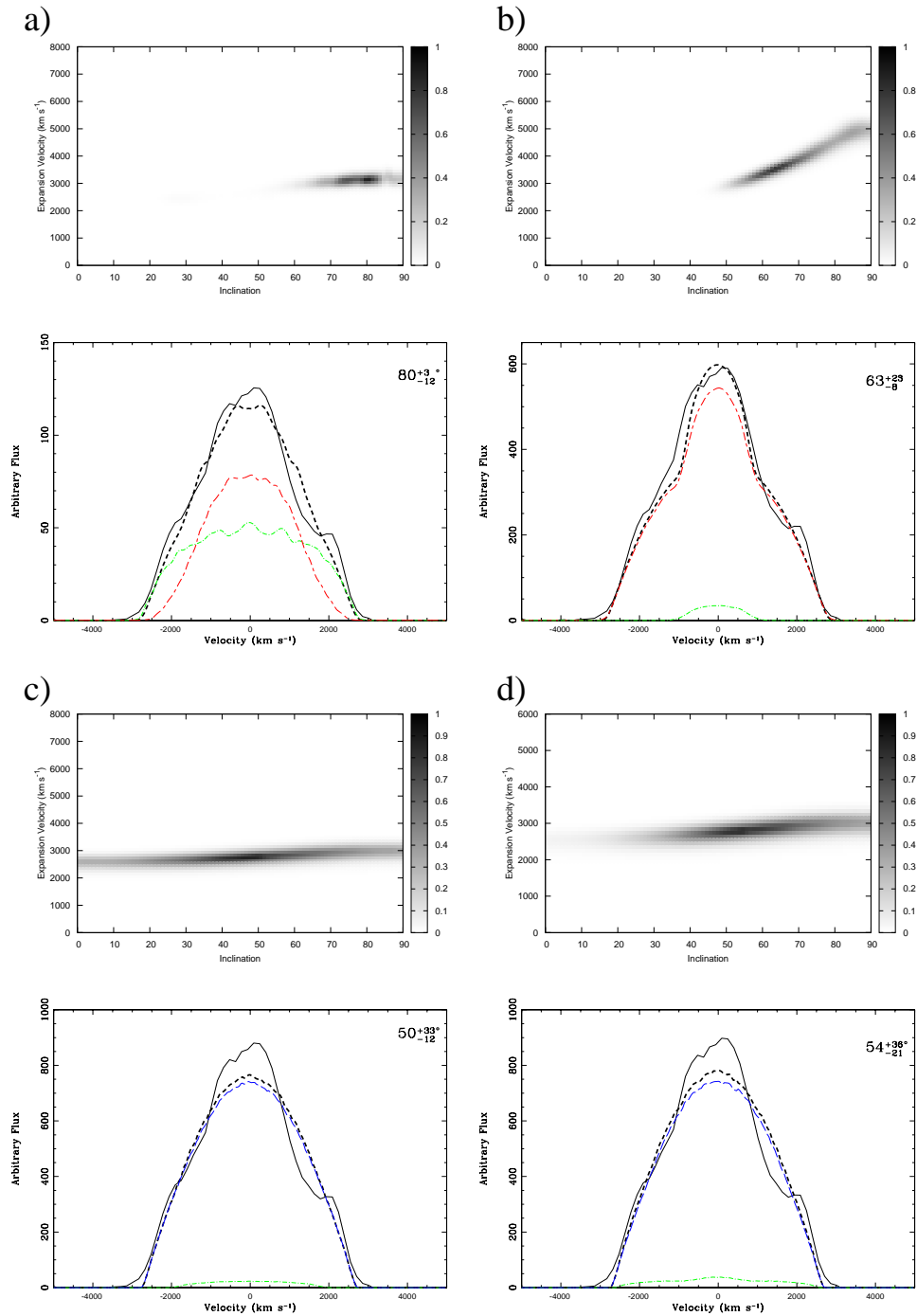


Figure 4.6: Results of the best-fit model spectrum to the observed spectrum on day 25 after outburst. The images are for a) polar blobs with an equatorial ring (Model A), b) dumbbell structure with an hour-glass overdensity (Model B), c) prolate shell with an equatorial ring (Model C) and d) prolate shell with tropical rings (Model D). *Top* – the most likely result for the structure, where the colour gradient represents the probability that the observed  $\chi^2$  value is correct. *Bottom* – the observed (solid black) and modelled spectrum (short-dash black). Also shown are the individual component contributions; rings (dot-dash green), prolate (long-dash blue) and polar blobs and dumbbell (short-dash-long-dash red).

To determine the best-fitting morphology, the derived reduced  $\chi^2$  probabilities were examined and it was found that Models A and B showed comparable probabilities. The other structures had negligible probabilities.

### 4.5.2 Later epoch observations ( $t = 108$ days)

Another test performed on the models to see which best reproduces the data, now considering only Models A and B, was to evolve the models to a later epoch, keeping the parameters for inclination and  $V_{\text{exp}}$  as derived from the first epoch. In the case of Model A, it was allowed to evolve linearly. However, Ribeiro et al. (2009, see also Chapter 3) suggested that their central component for RS Oph showed deceleration and therefore this central component was kept the same size from one epoch to the next in Model B.

What is evident is that if the models are allowed to evolve linearly, with the derived parameters the same, then the line profile should look identical from one epoch to the next in the absence of other physical changes. For the line profile to change, but with the velocity field and inclination constant, there must be a transition involving other factors. Just changing the densities does not suffice without the addition of new components. This transition may therefore be associated to the termination of the post-outburst wind phase and the complete ejection of the envelope, which is proposed to happen within the first couple of weeks (as in V382 Vel; della Valle et al. 2002). Therefore, the later epoch modelling does not have a filled distribution but now has a depth of material (shell) determined by the first epoch model. Therefore a volume distribution was applied within this shell to both models and compared with the spectrum at day 108 after outburst (Figure 4.4). Furthermore, Munari et al. (2011b) from photo-ionisation models showed the nova to be in the nebular stage at day 108 after outburst and the [N II] 6548 and 6584Å emission lines could have contributed significantly to the H $\alpha$  profile. Certainly [O III] was about ten times stronger than H $\alpha$  at this time (Munari et al. 2011b).

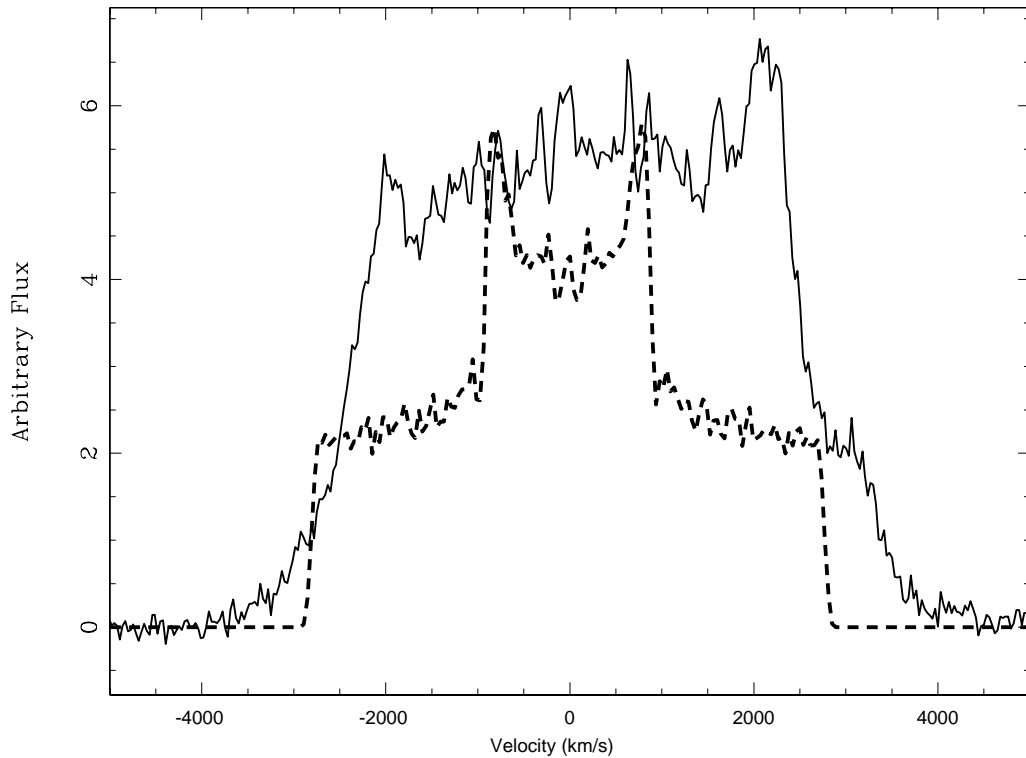


Figure 4.7: Observed spectrum (solid) at 108 days after outburst with the thin shell Model B line profile for comparison (dashed).

### Model B – Dumbbell with an hour-glass overdensity

The Model B synthetic spectrum did not reproduce the observed second epoch spectrum. The synthetic spectrum was that of an upside down “T” shape (Figure 4.7). Although Model B as a thin shell did not provide a reasonable fit to the second epoch this general model was investigated further. Therefore the first epoch model line profile generated by a filled shell (Figure 4.6) was subtracted from the observed spectrum on day 108 after outburst. The result, shown in Figure 4.8, is reminiscent of an optically thick accretion disc line profile (Figure 4.9, Horne & Marsh 1986). Furthermore, the separation of the peaks on the line profile is consistent with a high inclination disc and the observed high velocity would suggest a high mass WD.

To consider if this is an accretion disc the integrated flux of the spectrum was investigated. Munari et al. (2011b) derive a dereddened  $H\alpha$  integrated flux of 9.3

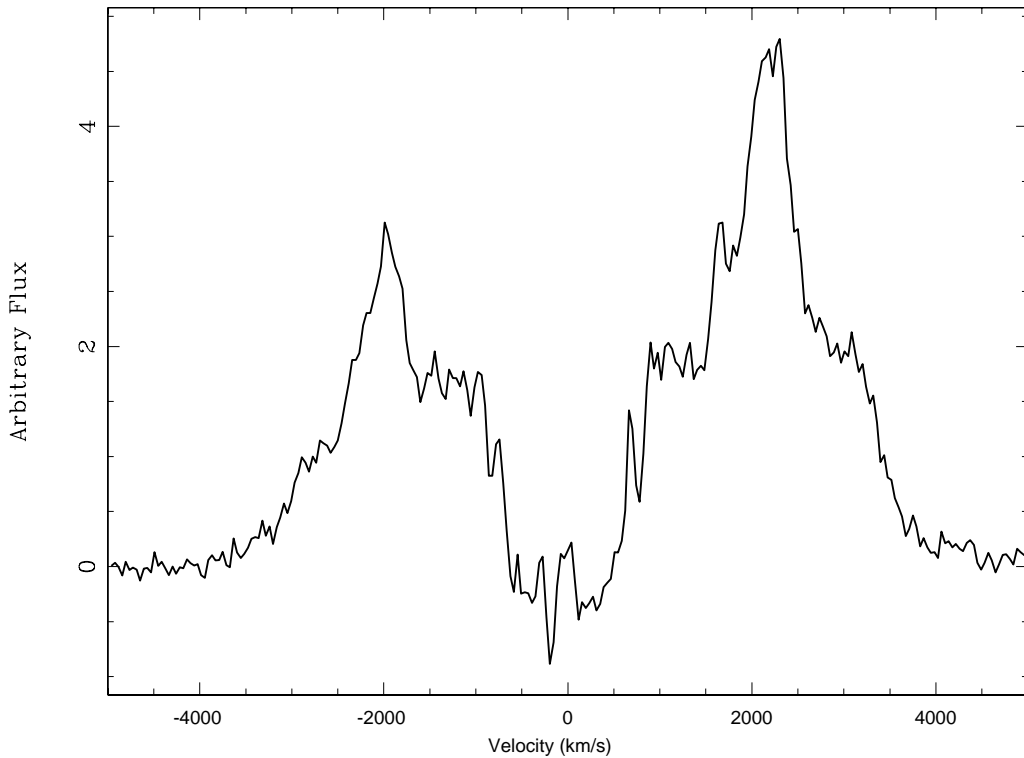


Figure 4.8: Observed spectrum at 108 days after outburst with the RS Oph-like line profile subtracted. The line profile is similar to an optically thick accretion disc profile (see Figure 4.9).

$\times 10^{-13} \text{ erg cm}^{-2} \text{ s}^{-1}$  for the spectrum on day 108 after outburst. This translates to an accretion disc flux of  $2.6 \times 10^{-13} \text{ erg cm}^{-2} \text{ s}^{-1}$ . Therefore, the luminosity of DQ Her, at a distance of  $525 \pm 28 \text{ pc}$  (Vaytet et al. 2007), was compared with V2491 Cyg. DQ Her's luminosity is around  $1.6 \times 10^{32} \text{ erg s}^{-1}$  (Bianchini et al. 2004) while a luminosity for V2491 Cyg is suggested as around  $6.1 \times 10^{33} \text{ erg s}^{-1}$ . The value for the luminosity of V2491 Cyg is thus much greater than DQ Her, at this time.

In subsequent observations at day 831 after outburst, the  $\text{H}\alpha$  integrated flux was  $1.33 \times 10^{-14} \text{ erg cm}^{-2} \text{ s}^{-1}$  (Munari et al. 2011b). A comparison of broadband  $r'$  and narrow band  $\text{H}\alpha$  imaging taken by collaborators using the LT on day 833 after outburst also showed a clear and significant  $\text{H}\alpha$  excess was still present. A possible contribution from  $[\text{N II}]$  cannot be deblended because of the low signal-to-noise of this spectrum, but lack of other noticeable nebular lines suggested at

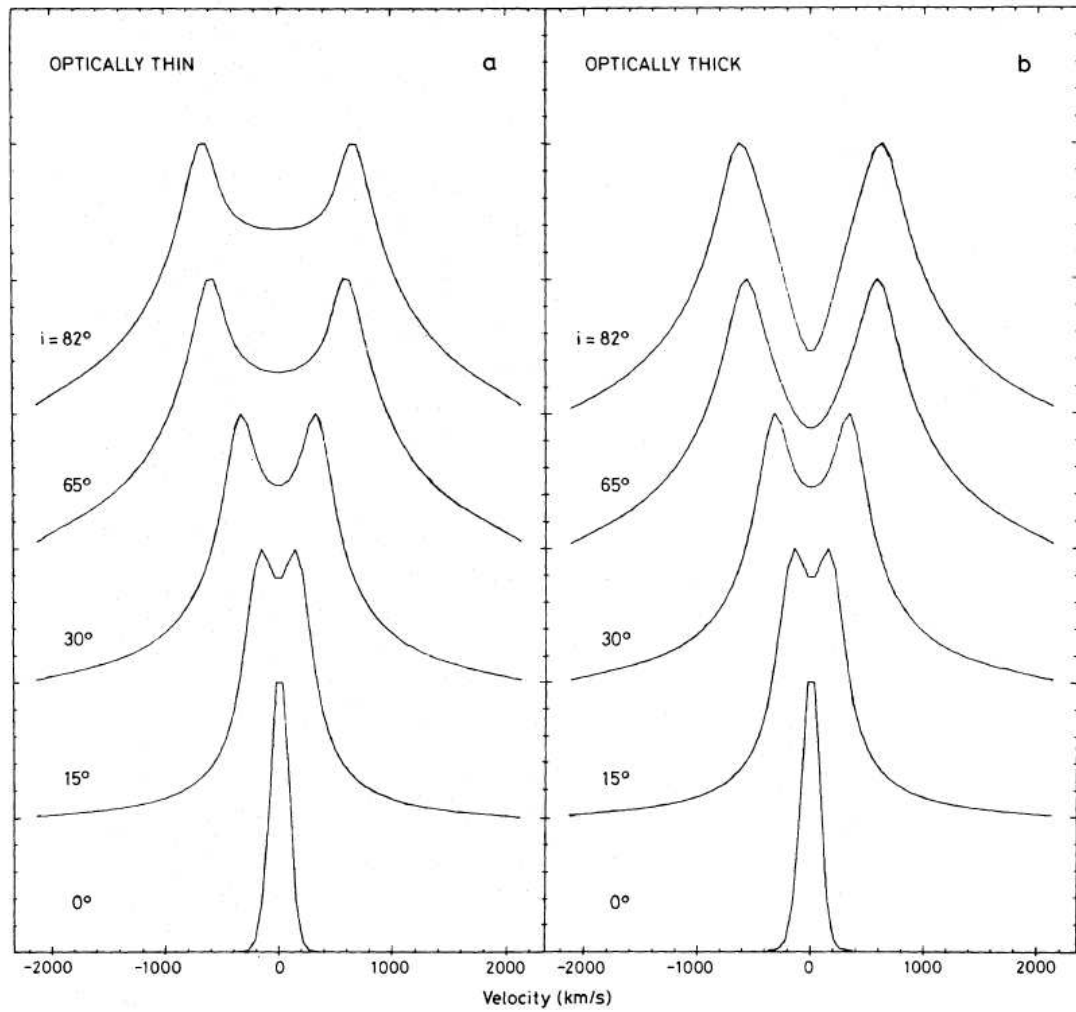


Figure 4.9: Synthetic line profiles for optically thin and optically thick emission lines covering a range of inclinations (from Horne & Marsh 1986).

first sight that the majority of the measured flux arises from  $H\alpha$ . This integrated flux equates to a luminosity of around  $3.1 \times 10^{32}$  erg  $s^{-1}$  for  $d = 14$  kpc, i.e. now much closer (within a factor  $\sim 2$ ) to that observed in DQ Her at quiescence. If this is emission from an accretion disc, it may imply that V2491 Cyg had a much higher accretion rate at day 108 than in DQ Her, which then declined towards the DQ Her value. It should also be noted that observations by Munari et al. (2011b) showed that the nova on day 108 after outburst was in the nebular stage while at day 477 after outburst it was close to quiescence. Alternatively, emission still dominated by the expanding ejecta is being observed. However, as will be demonstrated below the favoured model is Model A.

### **Model A – Polar blobs and equatorial ring**

In light of the probably presence of significant contamination from the [N II] lines these should be accounted for when modelling the spectra on day 108. [N II] is expected to appear as the expanding remnant becomes less dense and the nebular spectrum emerges. Using the evolved Model A above, collaborators were able to devise a simple code that would fit the observed spectra with the synthetic in order to provide a best-fit result. In the first instance to fit the observed spectrum, the velocities were kept constant from the first epoch for the  $H\alpha$  and [N II] lines and only the relative flux was allowed to change. The model derived for  $H\alpha$  is assumed to be the same for [N II]. This did not reproduce the observed spectrum without introducing significant additional absorption features.

Therefore the velocity of the different components was allowed to vary keeping the flux ratio of the [N II] lines always at 1:3 (as dictated by atomic physics) and the relative flux of the  $H\alpha$  to the [N II] lines as a free parameter. The result of this modelling is shown in Figure 4.10. This provides an excellent fit to the spectrum at day 108. The derived maximum velocities for the polar blobs were  $\sim 3500$  km  $s^{-1}$  ( $H\alpha$ ) and  $\sim 3600$  km  $s^{-1}$  ([N II]) and for the equatorial ring,  $\sim 2700$  km  $s^{-1}$  ( $H\alpha$ ) and  $\sim 2600$  km  $s^{-1}$  ([N II]). These results are within  $2\sigma$  of those derived

for the first epoch.

It should be noted that there is a change in the contributions to the flux of the different components of  $H\alpha$ . Where in the first epoch the two components were of comparable flux, in the second epoch the ring is the major contributor to the flux with relative flux contribution of the polar blobs to the ring of 1:2.5 for  $H\alpha$ . This change in relative flux can be easily understood as arising from the fact that material moving at higher velocities will fade faster in its  $H\alpha$  emission. Therefore, the change shown in Figure 4.10, where the equatorial ring becomes the dominant component, stems from the fact that it presents an expansion velocity lower than that of the polar blobs. In the case of the  $[N II]$  line the polar blobs to ring relative flux contribution is 2.2:1. Their expansion velocities are  $\sim 3600 \text{ km s}^{-1}$  and  $\sim 2600 \text{ km s}^{-1}$ , respectively.

Furthermore, Munari et al. (2011b) show a line profile at day 477, which is very different from the day 108 line profile (Figure 4.11). The model can also account for this if the densities of the different components continue to evolve. As the nebula becomes less dense it is expected that the relative contribution from  $[N II]$  should increase. At this time the ratio of the  $H\alpha$  polar blobs to equatorial ring is 3:1, an apparent increase of relative flux but this may be due to the fact that material from the inner regions of the central binary is being observed. The  $[N II]$  polar blobs to equatorial ring ratio (4.6:1) has increased as expected due to the fact that there is additional less dense material allowing for  $[N II]$  to emerge.

There is one more test we can perform to further constrain our model. The derived inclination of 80 degrees is very high and therefore eclipses are expected whose existence is now being investigated. Such eclipses should be easily observed in this system. For example, the CN DQ Her (orbital period  $\sim 4 \text{ h}$ ) shows  $\sim 0.9 \text{ mag}$  deep eclipses in UBVR (Zhang et al. 1995) as does the RN U Sco with eclipses of depth  $\sim 1.5 \text{ mag}$  in B (Schaefer & Ringwald 1995). Of course, if V2491 Cyg turns out to be eclipsing this will also enable us to determine more precisely important parameters of the central binary.

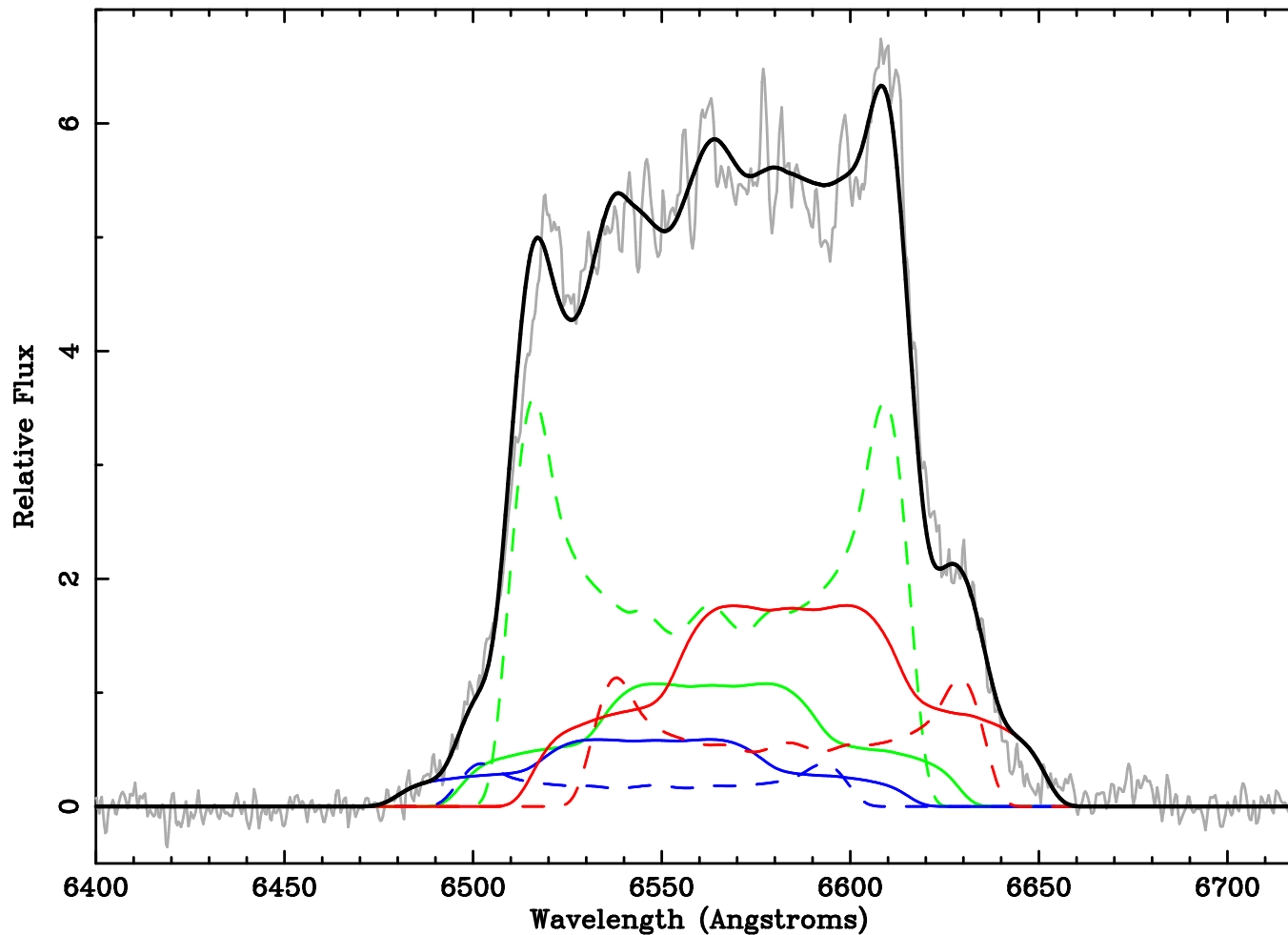


Figure 4.10: Fit to the observed line profile (grey) at day 108 after outburst. The model spectrum (black) is the sum of the individual components, H $\alpha$  (green), [N II] 6584Å (red) and [N II] 6548Å (blue). The ring (dashed line) and polar blobs (solid line). The ratio of the [N II] lines was kept at 1:3 and the relative flux of the H $\alpha$  to the [N II] was kept as a free parameter (from Ribeiro et al. 2010).

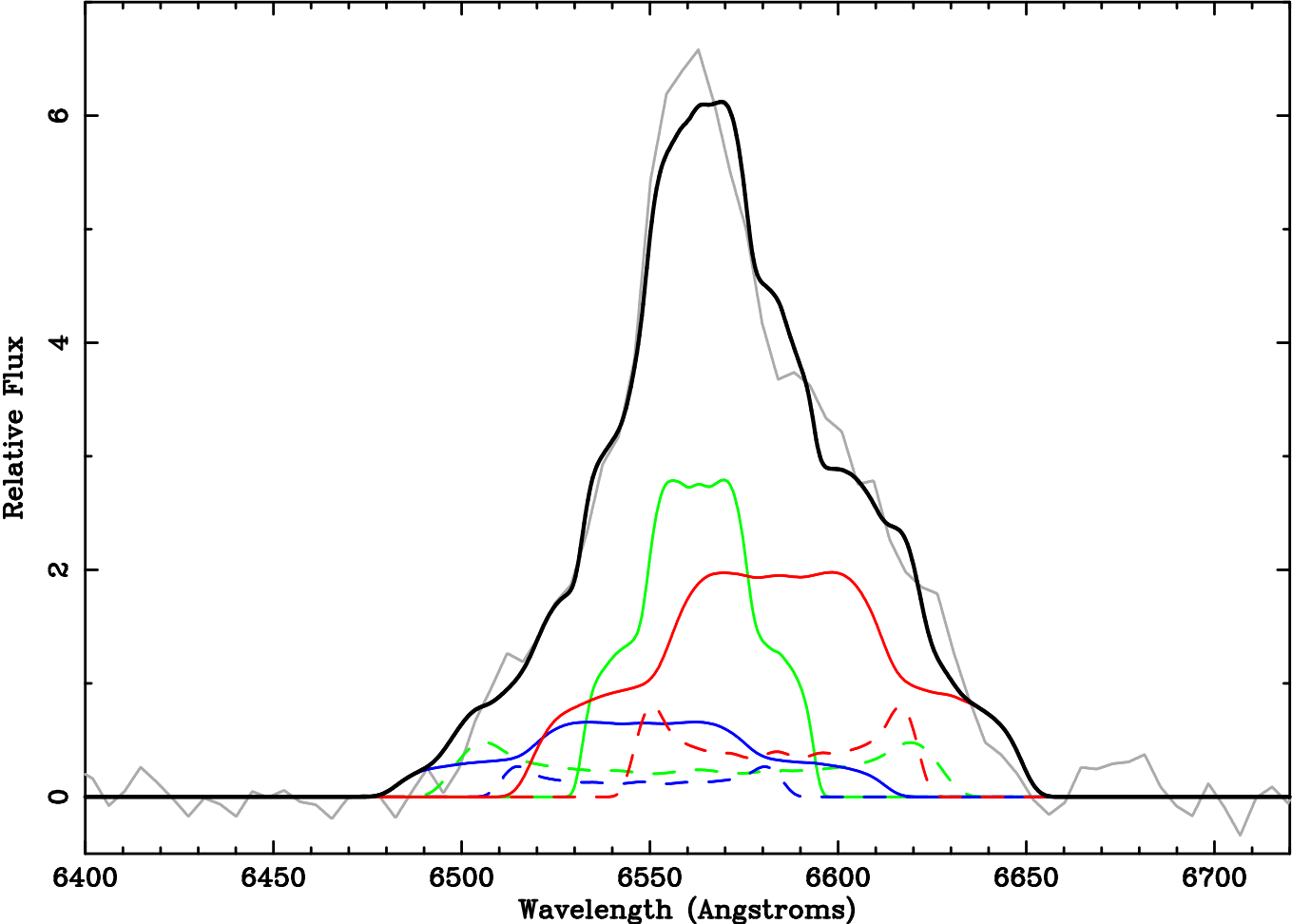


Figure 4.11: As Figure 4.10 but for day 108 after outburst (from Ribeiro et al. 2010).

## 4.6 Discussion and Conclusions

Of the morphologies discussed in detail above early in outburst, Models A and B are the best fitting and give results that are very similar to each other and this is reflected by the fact that the derived inclinations of the two modelled morphologies overlap, within the errors. Furthermore, the main real difference is in the size of the central region. Model A is representative of a CN system, while the Model B has a morphology that has been observed in the RN RS Oph.

To explore the second epoch observations the model was allowed to evolve into a system that was not volume filled but a shell. To replicate the observed spectrum with Model A significant emission from the [N II] lines around  $H\alpha$  at this time was needed and the components' densities required to be changed with the equatorial ring becoming the dominant contributor to the flux. The change in derived densities between the components should also be expected since the different components are moving at different speeds. Emission from the polar blobs moving at higher speed will be observed to fade faster than the equatorial ring. Model B at the second epoch did not reproduce the line profile using a thin shell however. It was also proposed that if the filled shell model was subtracted from the observed profile the residual resembled an accretion disc profile. However, it was shown from the second epoch observations that Model A is suggested the most likely giving an inclination of  $80_{-12}^{+3}$  degrees and a maximum expansion velocity of  $3100_{-100}^{+200}$  km s<sup>-1</sup>, for the polar blobs. This velocity is in line with those found in high-ionisation absorption lines in X-ray spectra by Ness et al. (2010, MNRAS, submitted). Further fitting to a third epoch also gave good fits for this model, adding to the confidence that this model is correct.

The high inclination found for Model A is however difficult to reconcile with the outburst amplitude vs. decline rate relationship for classical novae (Figure 4.12, Warner 1987). The observed amplitude of 10 mags is much lower than that predicted for the derived inclination of 80 degrees (15.5 mags) while a pole-on system would still have a predicted amplitude of 12.5 mags. However, RNe present

a similar outburst amplitude at a similar inclination (e.g., Munari et al. 1999). This is in line with the suggested RN nature of this object from other authors (e.g., Page et al. 2010). Further exploration of the nature of the progenitor will be presented in Darnley et al. (2010, in preparation)

These results also suggest that eclipses should be observed for this inclination. Spectroscopy at quiescence will in addition help determine the relative contributions to the line flux from any accretion disc. Furthermore, the distance to the system should be explored by looking for a resolved remnant.

In the next Chapter the structures and techniques explored here are applied to the suggested RN V2672 Oph in order to determine the properties of the nebular remnant and hence the central binary system.

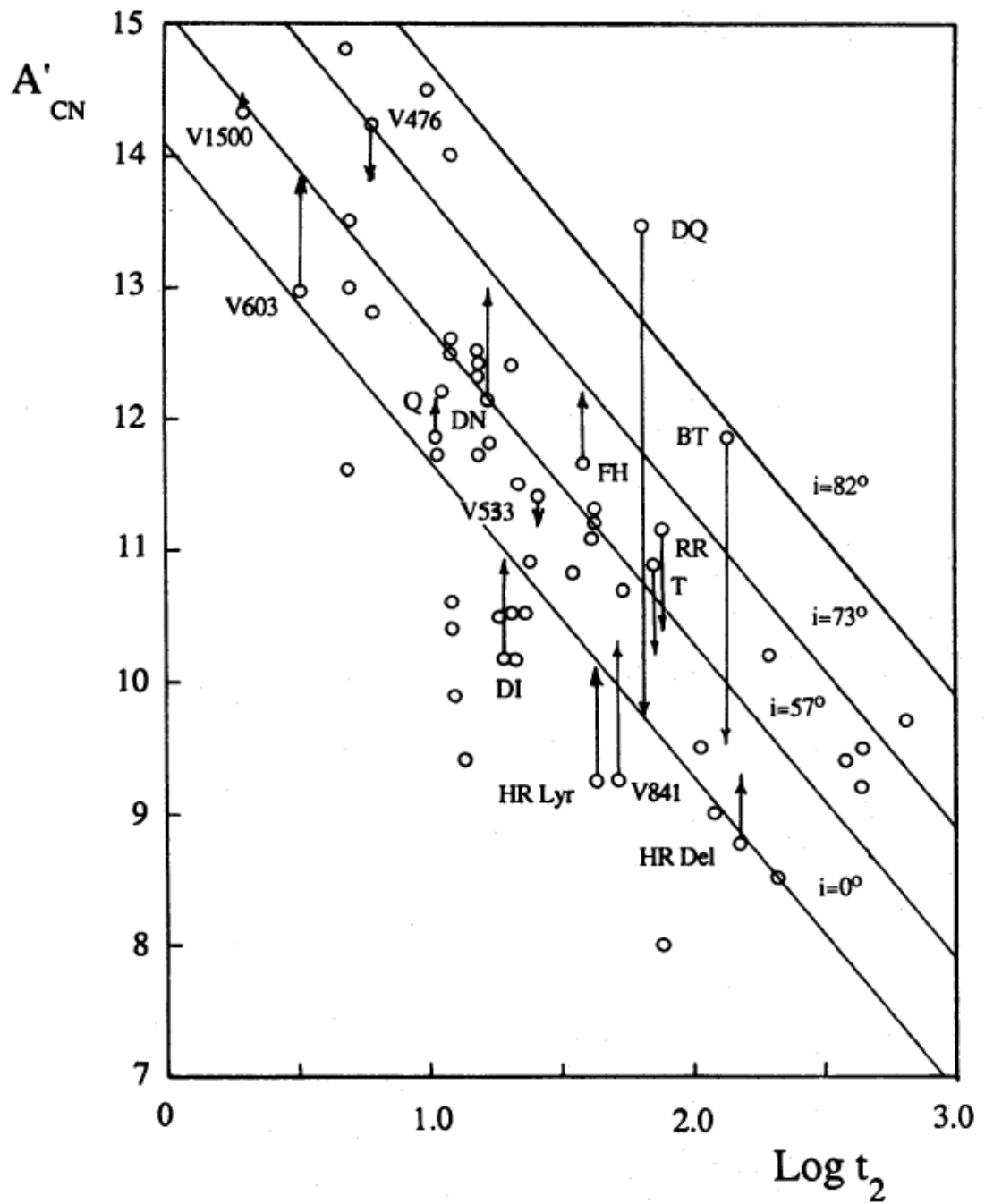


Figure 4.12: Amplitude ( $A'_{CN}$ )-rate of decline ( $t_2$ ) relationship for CNe (from Warner 1987).

# Chapter 5

## The Morphology of the Expanding Ejecta of Nova V2672 Ophiuchi<sup>1</sup>

### 5.1 Introduction

Nova Ophiuchi 2009 (hereafter, V2672 Oph) was discovered in outburst on 2009 August 16.515 UT at mag = 10 on unfiltered CCD images (taken as  $t = 0$ , Nakano et al. 2009). This was confirmed spectroscopically on 2009 August 17.6 and 17.8 UT with very large velocity width for H $\alpha$  and the paucity of other emission lines on a red and featureless continuum (Ayani et al. 2009; Munari et al. 2009).

V2671 Oph is a very fast nova with  $t_2(V) = 2.3 \pm 0.1$  days (Munari et al. 2011a) and is as fast as V1500 Cyg (Young et al. 1976) and V838 Her (e.g., Schwarz et al. 2007) among CNe and U Sco (Munari et al. 1999, 2010) among RNe. The distance to the system has been determined, using several methods and averaging them, as  $19 \pm 2$  kpc and  $E(B - V) = 1.6 \pm 0.1$  (Munari et al. 2011a).

Munari et al. (2011a) found no progenitor counterpart in the 2MASS and SDSS

---

<sup>1</sup>The work presented in this Chapter was published in Munari et al. (2011a).

surveys and suggested that this non-detection favours a system similar to U Sco if it were a RN, rather than RS Oph or T CrB, with an inferred orbital period of order days. They go on to suggest that the photometric (Figure 5.1) and spectroscopic similarities with U Sco are evidence for the recurrent nature of V2672 Oph. Furthermore, the reasons for only one outburst being detectable were suggested as (i) V2472 Oph suffers from long seasonal invisibility; (ii) its southern declination means that it is only observable for a brief fraction of the year from northern latitudes where most observers have been historically concentrated; (iii) it is also faint at maximum; and (iv) the fast decline time means that V2672 Oph would return below the discovery threshold very quickly (Munari et al. 2011a).

Schwarz et al. (2009) detected V2672 Oph on day 1.5 after outburst with the *Swift* satellite with both the XRT and UVOT instruments. They too suggested that the rapid decline in the optical/UV light curves, the extremely broad emission lines, and the early X-ray detection imply that V2672 Oph is either a RN or a very fast CN. Furthermore, they suggested that the observed early hard X-ray emission was likely due to shocks between the fast ejecta and a pre-existing circumstellar medium (as in the RN RS Oph – Bode et al. 2006) or intra-ejecta shocks (as in the very fast CN V838 Her – O’Brien et al. 1994).

V2672 Oph was also observed and detected at radio wavelengths on day 15 after outburst at 8.46 GHz. However, on day 18 after outburst there was no detection at 22.46 GHz (Krauss Hartman et al. 2009). They suggested that the non-detection is due to the emission being already optically thin, or a substantial fraction of the observed flux density was synchrotron in origin. In support of the latter view, Krauss Hartman et al. (2009) noted that observed hard X-ray emission was evidence of relativistic electrons and strong magnetic fields needed to generate synchrotron radiation. Furthermore, the detection of radio synchrotron emission lends support to the suggestion that V2672 Oph might be a RN. For example, RS Oph shows strong radio synchrotron emission within days of the outburst (e.g., Padin et al. 1985; O’Brien et al. 2006; Eyres et al. 2009).

The observations and data reduction for this Chapter were taken by collabora-

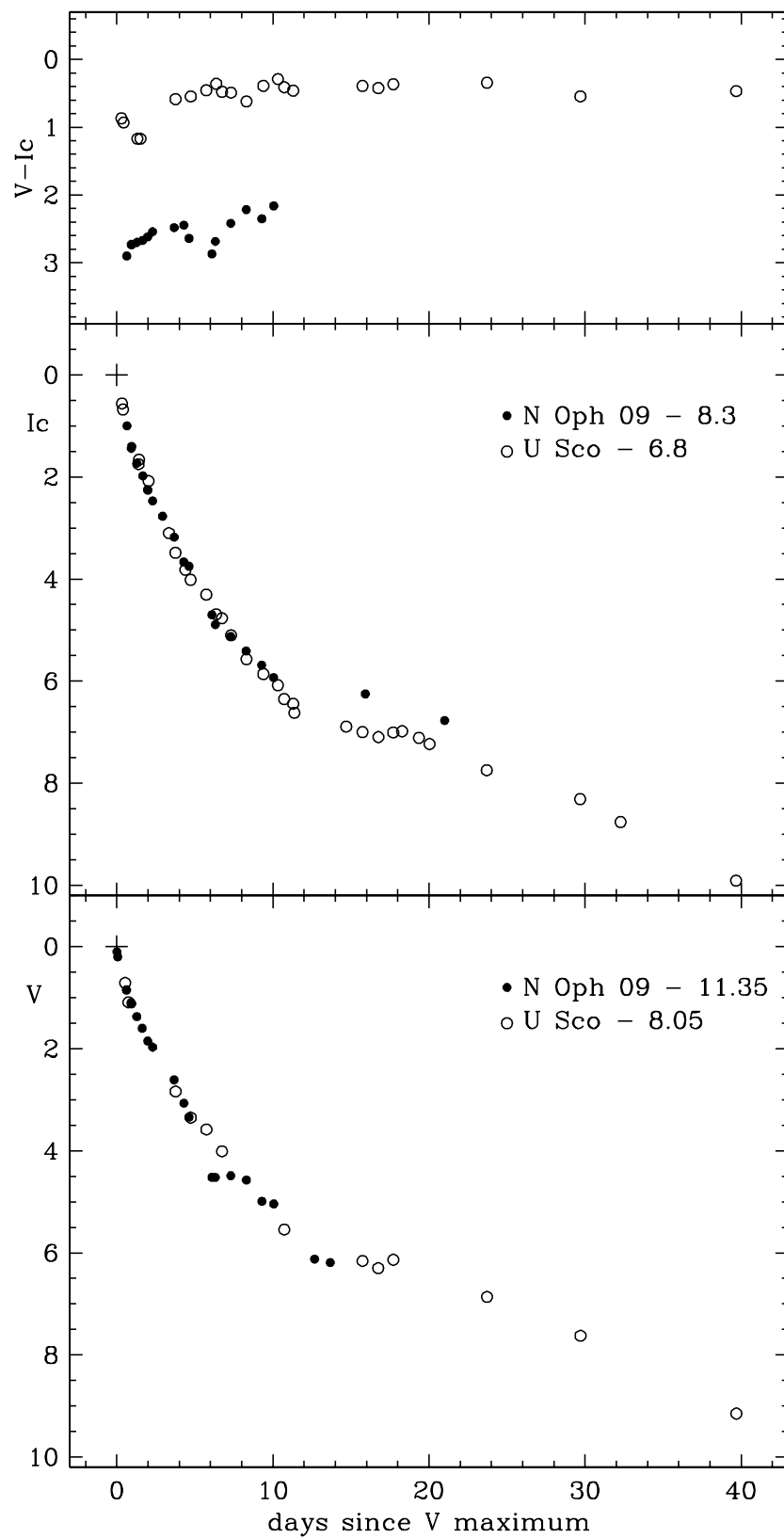


Figure 5.1: Comparison between the photometric evolutions of V2672 Oph and U Sco during its 2010 outburst (from Munari et al. 2011a).

tors and published in Munari et al. (2011a). The Chapter concentrates on the use of the reduced spectra to perform morpho-kinematical modelling using the techniques employed in Chapter 4. In Section 5.2 the particular procedures for modelling V2672 Oph are described. The results are then presented in Section 5.3 and discussed in Section 5.4.

## 5.2 Modelling Procedure

As in Chapter 4, the line of interest is the  $H\alpha$  emission line. Again care was taken when dealing with  $H\alpha$  (Section 4.4.1). The best first estimate structure for modelling here was decided from visual inspection of the synthetic spectra from Chapter 4. This allowed initial constraints to be placed on the overall structure.

### 5.2.1 Initial information

Gaussian fitting was performed using the IRAF task `SPECFIT` on days 2.34 through 8.33 after outburst. As before, this allows the decomposition of different Gaussian components of the  $H\alpha$  line to retrieve information such as the FWHM of likely components and their radial velocity displacements (Table 5.1). The presence of the diffuse interstellar band (DIB) at  $6614 \text{ \AA}$  (see Figure 5.4) is not important during detailed modelling given its small equivalent width.

The values derived in Table 5.1 were used to determine the displacement of the system from the rest wavelength of the  $H\alpha$  line and to determine a first approximation to the size of the remnant using the values for the FWHM and radial velocity displacement of component 1.

### 5.2.2 Modelling

Munari et al. (2011a) showed evidence of significant  $H\alpha$  optical depth at early

Table 5.1: Results of Gaussian fitting to observed spectra. Shown are the observation dates, including time since outburst, and individual components' FWHM and radial velocity displacement in  $\text{km s}^{-1}$ . Components 1 and 4 relate to the polar blobs, Component 2 to the equatorial ring and Component 3 to the prolate structure described in Section 5.2.2.

day	Component 1		Component 2		Component 3		Component 4	
	FWHM	Radial	FWHM	Radial	FWHM	Radial	FWHM	Radial
+2.34	2128±38	-3406±23	982±33	-193±8	3791±160	-193±8	2258±38	3245±24
+3.34	2152±53	-3469±32	844±29	-222±7	3717±300	-222±7	2172±62	3137±37
+5.31	2310±130	-3414±78	528±27	-216±9	3083±710	-216±9	2319±120	3094±75
+8.33	2283±120	-3363±79	334±14	-252±6	3598±1200	-252±6	2314±130	2957±80

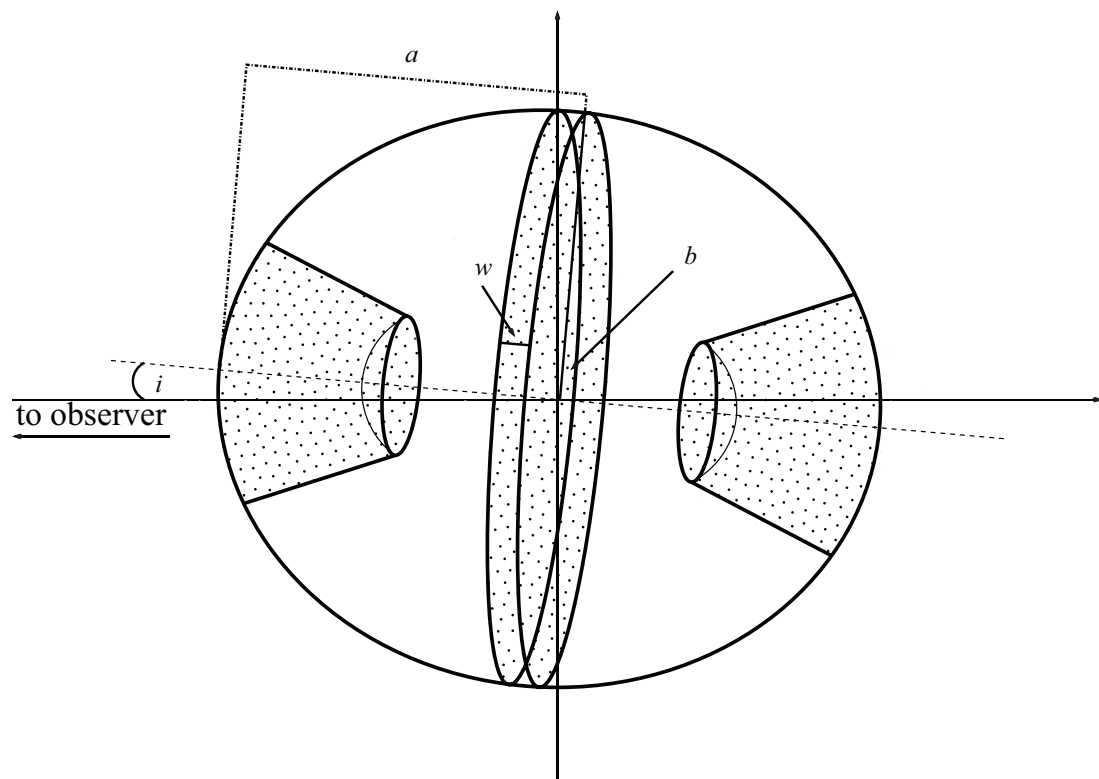


Figure 5.2: Two-dimensional representation of the three-dimensional expanding structure of the V2672 Oph remnant. The overall structure is that of a prolate system with polar blobs and an equatorial ring. The shaded areas represent regions of high density. The semi-major axis ( $a$ ) is larger than the semi-minor axis ( $b$ ) by 15%. The width of the ring is designated  $w$ . The inclination of the system ( $i$ ) is defined as the angle between the line of sight to the observer and the semi-major axis (see also Figure 1.6).

time. The modelling of the V2672 Oph spectra thus initially focused on day 8.33 after outburst because at this time the  $H\alpha$  line can be assumed least optically thick. Furthermore, the symmetry of the line is compatible with being optically thin at this time. The assumed physical size of the object was taken only from component 1 in Table 5.1 because it is assumed that the blue side of the line suffers less self-absorption than the red.

The suggested structure for the remnant was that of polar blobs and an equatorial ring with a low density prolate structure surrounding these two. A ratio of 1.15 for the semi-major axis versus semi-minor axis was taken as an estimate from the nova's speed class (Slavin et al. 1995). The low density prolate structure is used to account for some of the lower velocities observed in the spectra. The parameter space was sampled for inclinations of the system from 0 to 90° (in 1° steps). A realistic velocity range for nova explosions from 100 to 8000  $\text{km s}^{-1}$  (in 100  $\text{km s}^{-1}$  steps) was also sampled, assuming a Hubble-flow like velocity field.

### 5.3 Results

The observed spectrum and the model spectra for each of the inclinations and velocities were compared to find the best-fit via a  $\chi^2$  test (Figure 5.3, top). The best-fit inclination and maximum expansion velocity (at the poles) were derived as  $0 \pm 6$  degrees and  $4800_{-800}^{+900}$   $\text{km s}^{-1}$  respectively ( $1\sigma$  confidence intervals).

The radial thickness of the polar blobs and equatorial ring was determined by the FWHM shown in Table 5.1. Figure 5.3 also shows the best-fit model spectra and the contribution of each individual component to the overall model spectrum. Just considering a model with polar blobs and an equatorial ring did not match the overall line profile. Even by adjusting the densities in each component the model spectrum would not fully replicate the observed spectrum. Therefore a filled prolate structure was introduced as an additional component (see Figure 5.2). This would be associated with material ejected more isotropically than that

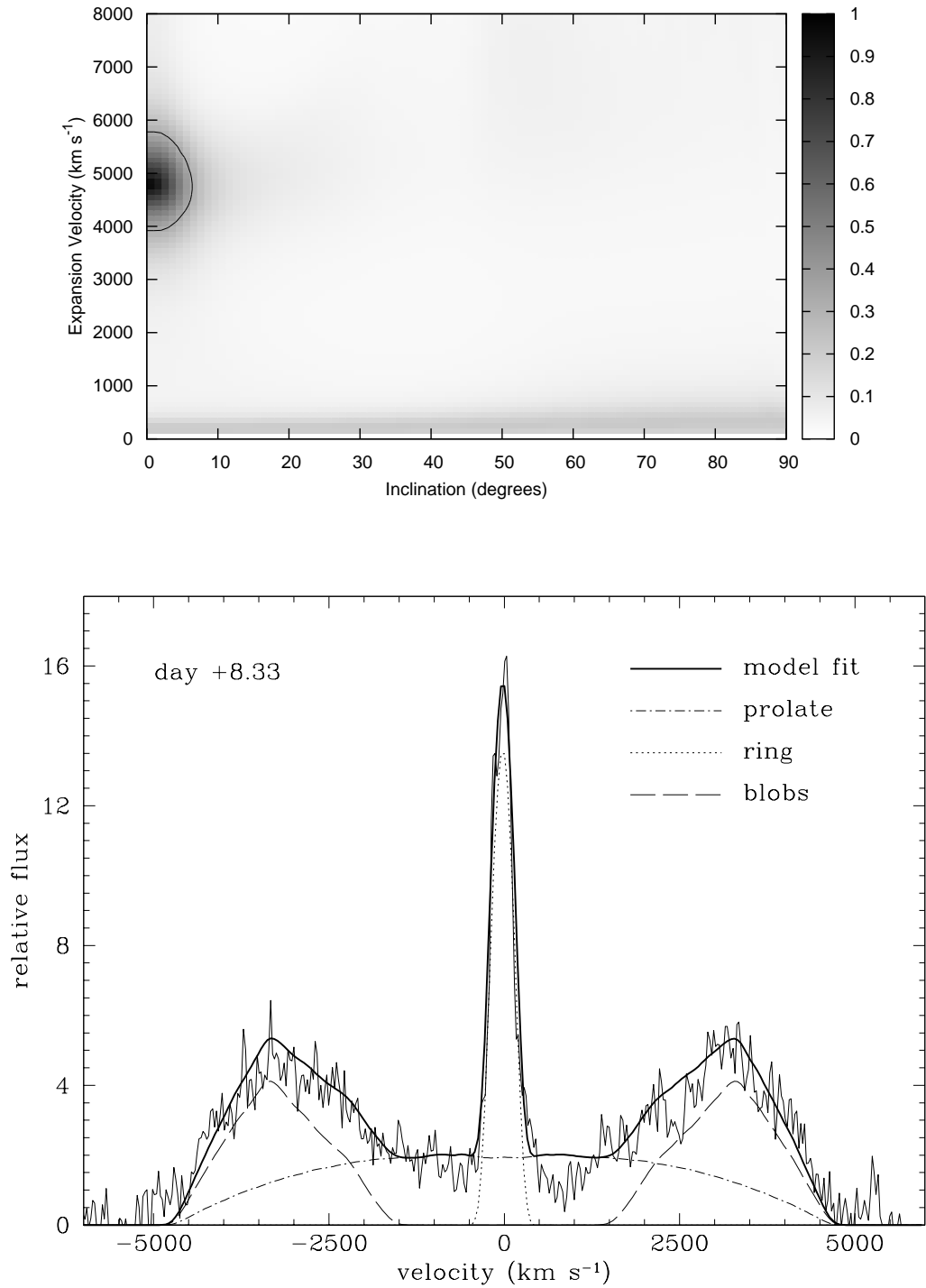


Figure 5.3: *Top* – image displaying results of a  $\chi^2$  fit comparing the observed spectrum with the model spectrum for different inclinations and velocities. The grey scale represents the probability that the observed  $\chi^2$  value is correct. Also shown is the  $1\sigma$  level contour (black). *Bottom* – the observed spectrum for day 8.33 and the best-fit model spectrum. The components of the model fit (prolate region, polar blobs and equatorial ring) are also shown.

Table 5.2: Evolution of the implied density ratios for the different model components.

day	Blob/Prolate	Blob/Ring	Prolate/Ring
+2.34	0.80	0.89	1.11
+3.34	2.36	1.60	0.69
+5.31	4.00	1.08	0.27
+8.33	6.40	0.84	0.13

in the ring or blobs. Furthermore, a filled structure can be reconciled with the assumption that at this stage the post-outburst wind phase and the ejection of the envelope are still ongoing (e.g., della Valle et al. 2002, Chapter 4).

The overall structure fitted on day 8.33 was then evolved to earlier times assuming a linear expansion and keeping the inclination and expansion velocity constant. As demonstrated in Figure 5.4, and Table 5.1, the observed spectrum shows the central component has higher velocities at earlier times, implying that some deceleration has occurred as the ejecta expanded.

The earlier epoch data were modelled (Figure 5.4) so that the polar blobs and prolate structure expanded linearly but the ring width ( $w$ ) was derived from the values in Table 5.1 for component 2 (with the ratio of the semi-major to semi-minor axes kept always as 1.15).

The assumption of a decelerating ring replicates the spectra well (Figure 5.4). The fact that the ring shows a smooth flat top structure compared to the observed spectra is because small scale structures are not included in the model. There is also some higher velocity material associated with the wings of the central component that is not reproduced. Furthermore, to better replicate the line profiles it was required that a change in density ratios of the components occurred with time (Table 5.2). What is evident from the ratio of the densities is that the prolate structure appears to reduce in density compared with the other structures while the blobs initially increase in density compared with the ring, then this ratio reduces again at a later time.

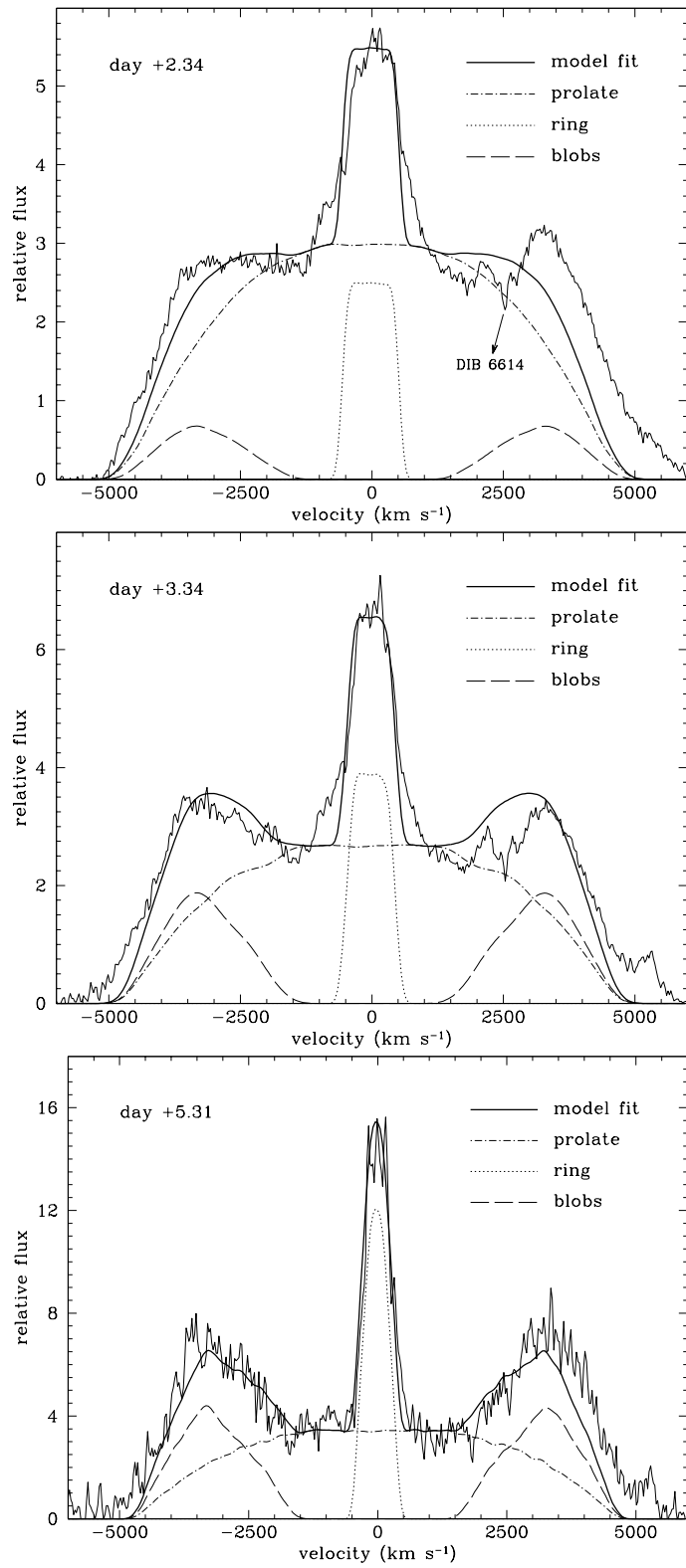


Figure 5.4: Early evolution of the H $\alpha$  profile and fitting by model spectra (see Figure 5.3 for further information).

## 5.4 Discussion

The overall structure of V2671 Oph has been constrained, as well as the inclination and expansion velocity for the expanding remnant, from modelling the H $\alpha$  emission line. The inclination and maximum expansion velocity have been derived as  $0 \pm 6^\circ$  and  $4800_{-800}^{+900}$  km s $^{-1}$ , respectively. A structure with polar blobs and an equatorial ring sitting within a prolate morphology replicates the spectra well. In CNe however, a structure with polar blobs and an equatorial ring originates in systems with low ejecta expansion velocity associated with slow speed class (e.g., Lloyd et al. 1997) while V2672 Oph is a very fast nova. This may call into question its CN nature.

The density variations in Table 5.2 indicate that the prolate structure quickly reduces in relative density. While for example, the blobs initially have lower density than the ring, this ratio then increases, possibly due to the interaction of the ring material with any pre-existing equatorial material, only to decrease again later. Some caution should be exercised here in over interpretation of these results as more detailed models, incorporating changes in line optical depths and ionisation structures are required.

Munari et al. (2011a) found no 2MASS counterpart to V2672 Oph which suggested the progenitor is not of the RS Oph type but more like a U Sco type recurrent. Further similarities to U Sco are apparent from the very fast decline from maximum, a plateau phase and “He/N” spectrum. The very high expansion velocities derived here are comparable to U Sco although the inclinations are very different. In U Sco, an eclipsing system, the inclination is around  $80^\circ$  which implies that any fast moving material would arise from an equatorial ring perpendicular to the plane of the sky. Here the inclination is suggested to be  $0^\circ$  and the fast material arises from the polar blobs. The discrepancy between the inclination and the photometric and spectral similarities may be solved if eclipses are found in V2672 Oph and these should be searched for in the next observing season.

Another way to explain this discrepancy in the inclination angle is by comparing the quiescent magnitudes of the two systems. U Sco has  $B = 18.55$  mag,  $E(B - V) = 0.2$  and a distance of 12 kpc. For V2672 Oph,  $B = 22.50$  mag,  $E(B - V) = 1.6$  and distance  $d = 19$  kpc. This translates to  $M_B = 1.69$  and  $-0.49$  for U Sco and V2672 Oph, respectively. Warner (1987) showed that a system with  $0^\circ$  inclination is 2.65 mags brighter than a system with an inclination of  $80^\circ$ . The apparent observed brightness difference for the two systems is  $\Delta m = 2.18$  which is comparable to that derived by Warner (1987). This difference could be due to a combination of accretion rate and WD mass.

In the next chapter, lessons learned in the previous two chapters are carried forward to do morpho-kinematical modelling of nova KT Eri. However, a new technique will also be introduced which greatly aids the decisions on parameters of interest. Furthermore, comparison between the evolution of the optical spectra and X-ray observations are performed for this object.

# Chapter 6

## Optical and X-ray Observations and Modelling of Nova

### KT Eridani

#### 6.1 Introduction

Nova Eridani 2009 (hereafter, KT Eri) was discovered on 2009 November 26.36 UT in outburst by Guido et al. (2009). Low resolution optical spectra obtained on 2009 November 26.56 showed broad Balmer series, He I 5016Å and N III 4640Å emission lines with FWHM of H $\alpha$  emission around 3400 km s<sup>-1</sup> (Guido et al. 2009). This object was confirmed later as a “He/N” nova (Rudy et al. 2009).

The discovery date is actually not the date of outburst. Other authors suggested the nova was clearly seen in outburst on 2009 November 18 and that the outburst occurred after 2009 November 10.41 (Drake et al. 2009). Hounsell et al. (2010) looked at the SMEI archive and LT SkyCamT (Sections 1.6.1 and 1.6.2) observations showing KT Eri in clear outburst on 2009 November 13.12 UT with a pre-maximum halt occurring on 2009 November 13.83. They derive the peak of the outburst to have occurred on 2009 November 14.67  $\pm$  0.04 UT (which is

taken as  $t = 0$ ) with  $m_{\text{SMEI}} = 5.42 \pm 0.02$ . Furthermore, they confirm the very fast nature of KT Eri, with a  $t_2 = 6.6$  days (Figure 6.1). A distance to the system has been derived by Ragan et al. (2009) as 6.5 kpc. However, it is noteworthy that this was assuming  $t_2 = 8$  days which is slightly different from that described above (although the SMEI magnitudes are white light effectively and  $t_2$  would be expected to differ from that in V for example).

KT Eri has also been detected at radio wavelengths (O’Brien et al. 2010) and as an X-ray source (Bode et al. 2010). The *Swift* satellite’s first detection of KT Eri with the X-ray Telescope (XRT; Gehrels et al. 2004) was on day 39.8 after outburst as a hard source (Bode et al. 2010). This was also the case on day 47.5. However, by day 55.4 the SSS had emerged (the dates here are slightly different from those quoted in Bode et al. (2010) because the dates have been corrected to the  $t = 0$  given above). On day 65.6 the SSS softened dramatically. Bode et al. (2010) also noted that the time scale for emergence of the SSS was very similar to that in the RN LMC 2009a (Bode et al. 2009c).

This Chapter discusses the optical spectroscopic observations in Section 6.2. The results of the optical spectroscopy are presented and their features related to the X-ray observations in Section 6.3. In Section 6.4 the modelling procedures are presented and the modelling results shown in Section 6.5. In Section 6.6 the overall results are discussed.

## 6.2 Observations

Optical spectra of KT Eri were obtained with the Fibre-fed Robotic Dual-beam Optical Spectrograph (FRODOSpec, Morales-Rueda et al. 2004), a multi-purpose integral-field input spectrograph on the LT. The dual beam provides wavelength coverage from 3900–5700Å (blue arm) and 5800–9400Å (red arm) for the low resolution ( $R = 2600$  and 2200, respectively) and 3900–5100Å (blue arm) and 5900–8000Å (red arm) for the high resolution ( $R = 5500$  and 5300, respectively).

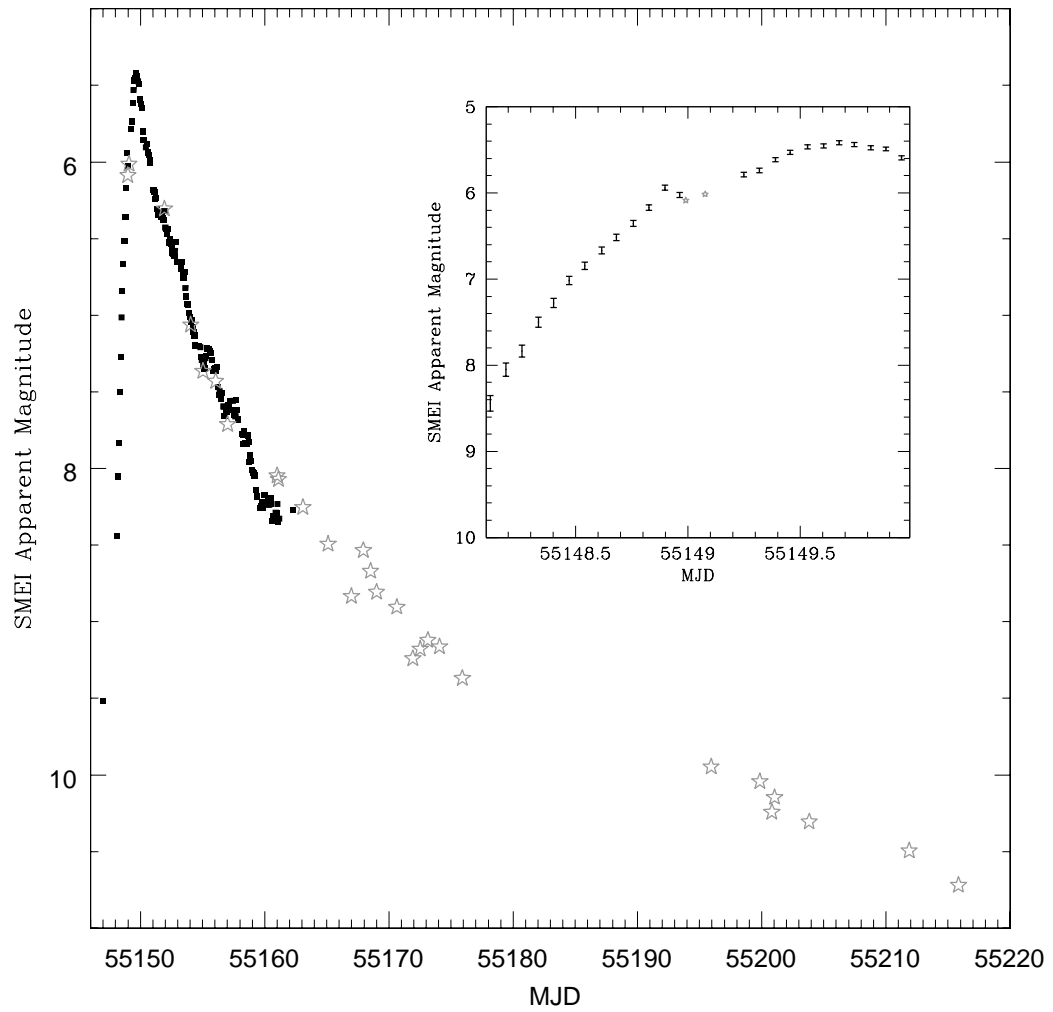


Figure 6.1: KT Eri SEMI (black squares) and LT SkyCamT (stars) light curve (from Hounsell et al. 2010).

Collaborators also provided spectroscopic observations from the 0.6m telescope of the Shiaparelli observatory in Varese, Italy equipped with a multi-mode spectrograph and various reflection gratings. The log of spectroscopic observations is shown in Table 6.1

Data reduction for FRODOSpec was performed through two pipelines. The first pipeline reduces the raw data. This includes bias subtraction, trimming of the overscan regions and flat fielding. Then the second pipeline performs a series of operations on the data, including flux extraction, arc fitting, throughput correction, linear wavelength rebinning and also sky-subtraction. The initial observations did not include a standard star. However, as of 2009 December 26 spectra were taken with the standard star HD19445. Any absorption features were patched over and then using the STARLINK Figaro IRFLUX task, correction for the instrumental efficiency/atmospheric transmission and relative flux calibration was performed on the KT Eri spectra. Although standard star observations were not available for observations taken before 2009 December 26, and since the main interest is to recover the intrinsic spectral shape, the standard star spectrum of 2009 December 26 was used on the previous dates spectra. The results of these procedures are shown in Figures 6.2 and 6.3, where the blueward end of the spectra, below 4040 and 6020Å respectively, have been removed due to high noise levels.

## 6.3 Observational Results

Figures 6.2 and 6.3 shows the observed emission lines in the FRODOSpec data. These present very wide profiles, with Balmer lines clearly observed, as well as He I 6678 and 7065Å, N II 5001Å and N III 4640Å, confirming KT Eri’s “He/N” nova spectral classification as described by Williams (1992). On day 48.16 the He II 4686Å emission line starts to emerge – it is certainly not as evident on day 47.20 (Figure 6.4). The He II 4200Å emission line is much harder to identify as to when it emerged because towards the blue end of the spectra the signal-to-noise

Table 6.1: Log of optical spectral observations of KT Eri with the FRODOSpec instrument on the Liverpool Telescope and the 0.6m telescope at the Schiaparelli observatory. The exposure times on FRODOSpec are for the blue/red arms, respectively.

Date	Days after outburst	Exposure time (s)	Telescope
2009 Nov 27	13.42	180/60	LT
2009 Nov 29	15.42	180/60	LT
2009 Dec 01	17.25	600	0.6m
2009 Dec 02	18.39	180/60	LT
2009 Dec 03	19.33	180/60	LT
2009 Dec 04	20.32	180/60	LT
2009 Dec 05	21.17	1800	0.6m
2009 Dec 05	21.24	180/60	LT
2009 Dec 06	22.34	180/60	LT
2009 Dec 07	23.32	180/60	LT
2009 Dec 08	24.40	180/60	LT
2009 Dec 10	26.21	180/60	LT
2009 Dec 15	31.14	600	0.6m
2009 Dec 18	33.21	1800	0.6m
2009 Dec 26	42.29	180/60	LT
2009 Dec 30	46.25	180/60	LT
2009 Dec 31	47.20	180/60	LT
2010 Jan 01	48.16	180/60	LT
2010 Jan 02	49.15	180/60	LT
2010 Jan 03	50.15	180/60	LT
2010 Jan 04	51.15	180/60	LT
2010 Jan 06	53.09	1200	0.6m
2010 Jan 07	54.20	180/60	LT
2010 Jan 11	58.16	180/60	LT
2010 Jan 12	59.14	180/60	LT
2010 Jan 14	61.14	180/60	LT
2010 Jan 16	63.13	180/60	LT
2010 Jan 18	65.21	1800	0.6m
2010 Jan 20	67.26	180/60	LT
2010 Jan 24	71.11	1800	0.6m
2010 Jan 24	71.20	3600	0.6m
2010 Jan 25	72.20	180/60	LT
2010 Jan 26	73.13	180/60	LT
2010 Jan 28	75.13	3600	0.6m
2010 Feb 02	80.16	3600	0.6m
2010 Feb 06	84.19	2700	0.6m
2010 Feb 13	91.22	6300	0.6m
2010 Feb 20	98.15	7200	0.6m
2010 Mar 16	122.14	1800	0.6m

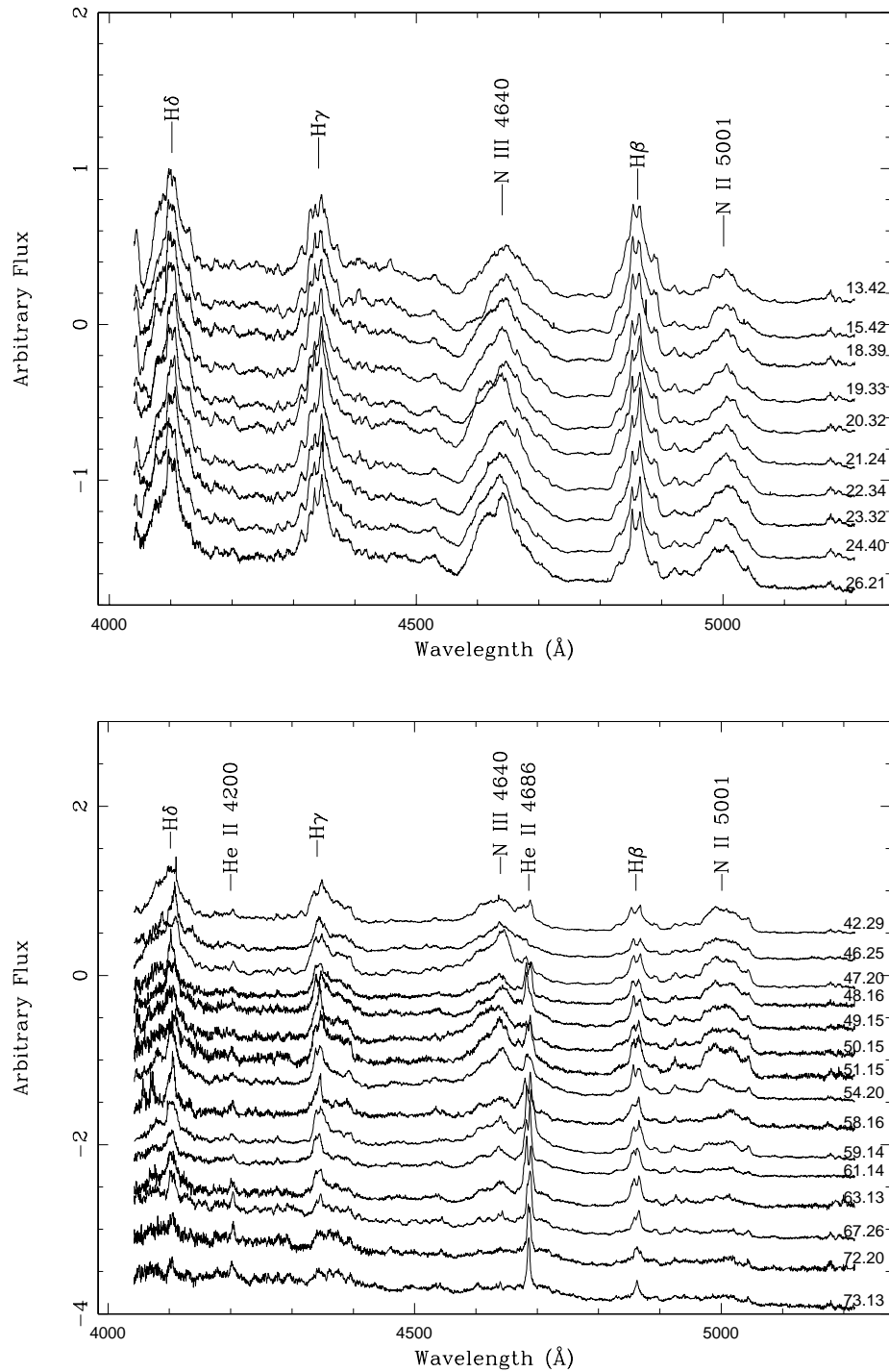


Figure 6.2: Blue arm FRODOSpec spectra. Dates after outburst are shown on the right hand side of each window. *Top* – spectra with the instrumental efficiency/atmospheric transmission removed using the standard star HD19445 from 2009 December 26. *Bottom* – spectra with standard stars applied at each epoch.

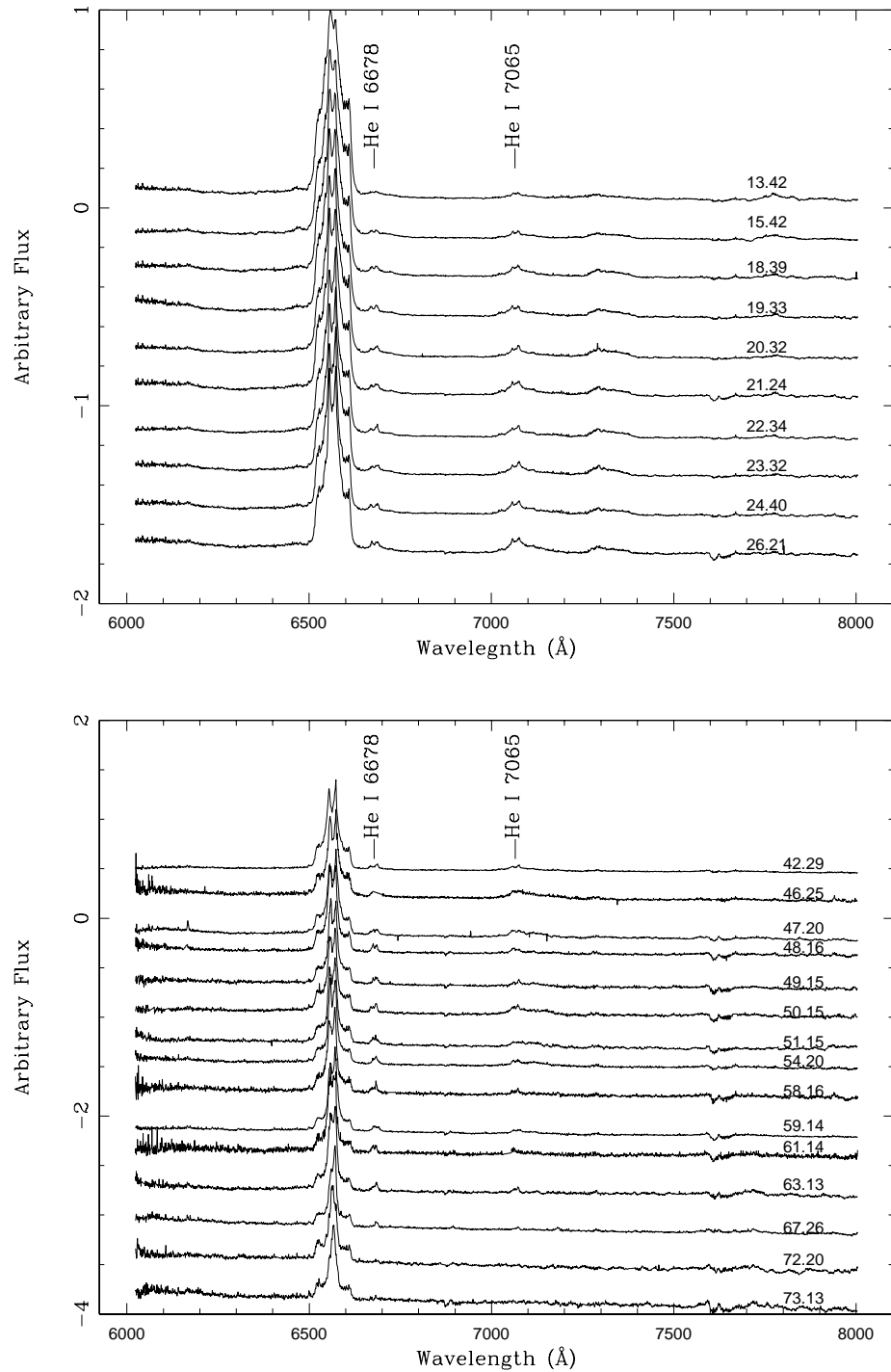


Figure 6.3: As Figure 6.2 but for the red arm.

is reduced significantly (Figure 6.2). However, it is evidently present by the time of the last observation on day 73.13. Furthermore, the He II line profile shown in Figure 6.4 is very complicated with a highly variable profile shape.

It is interesting to relate some of the features discussed above with the X-ray behaviour. Figure 6.5 compares the X-ray data from *Swift* with the evolution of the H $\alpha$  and He II 4684Å lines. The X-ray data were provided by collaborators at Leicester and some of the time bins in the hardness ratio (HR), defined as the ratio between counts in the 1–10 keV/0.3–1 keV energy bands, have been binned to increase the signal-to-noise ratio.

On day 47.5 the X-ray emission was still hard. However, by the next observation on day 55.4, the SSS had emerged. Since the SSS samples the nuclear burning on the WD surface this means that the ejecta had become optically thin so that material can be seen close to the surface of the WD. It is interesting to note that the He II 4686Å emission line arises from a region of high ionisation probably in the inner regions of the ejecta close to the WD surface. In the optical spectra of Figure 6.4 the He II emission line is already visible on day 48.16 it is probable that the line emerged between days 47.5 and 48.16. Examination of the individual X-ray spectra on day 47.5 (exposure coverage day 47.46 – 47.54) only showed 16 counts and a single count below 1 keV, which puts a tight constraint that the SSS had not emerged by day 47.54.

On day 48.16, when the He II line had emerged, the apparent V magnitude of KT Eri was around 10 mags. This was about 4.5 mags below maximum. Using the Bath & Harkness (1989) relationship for the effective temperature ( $T_{\text{eff}}$ ) of the photosphere as

$$T_{\text{eff}} = T_0 \times 10^{\Delta V/2.5} \text{K}, \quad (6.1)$$

where  $T_0 = 8000$  K (Evans et al. 2005, and references therein). Thus,  $T_{\text{eff}} \approx 5.1 \times 10^5$  K ( $\sim 43$  eV) although, this is only an approximation and does not take account of for example the contribution of nebular emission in the V band. Therefore, the derived value of  $T_{\text{eff}}$  is in line with the ionisation levels for He II

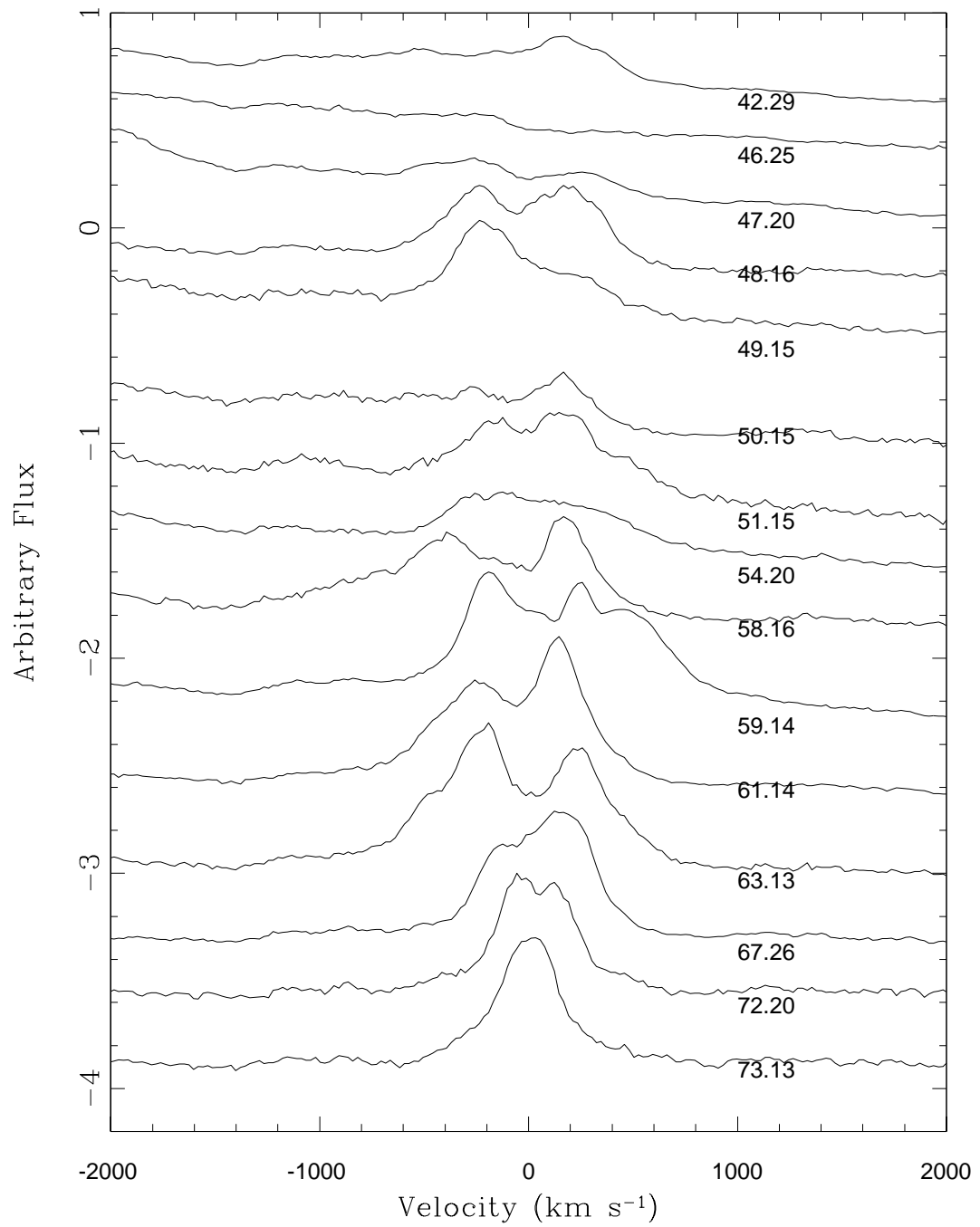


Figure 6.4: Spectral evolution of the He II 4686 Å emission line with days after outburst marked on each spectrum.

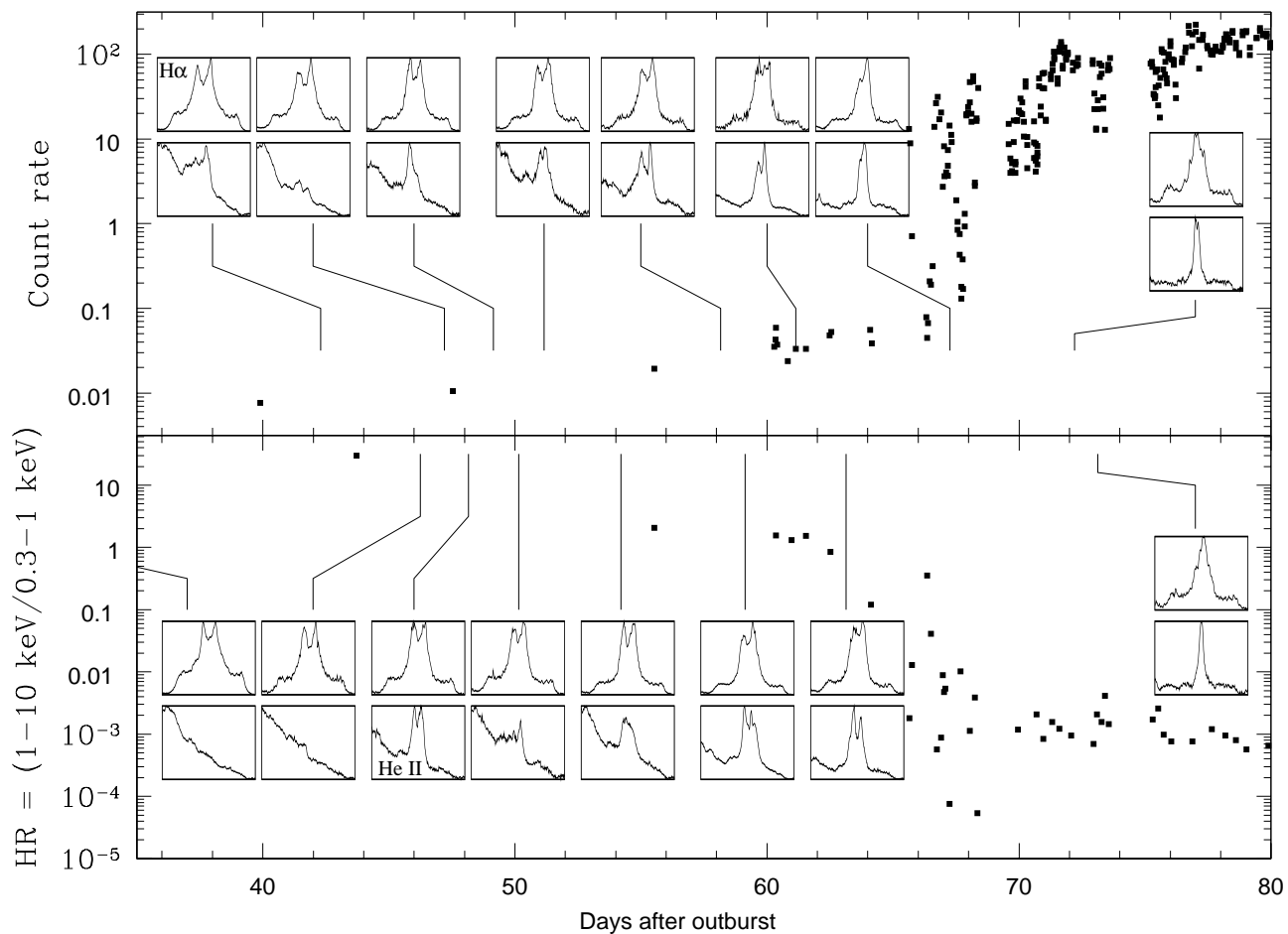


Figure 6.5: X-ray and optical spectral evolution. The X-ray count rate (top) and hardness ratio (bottom) are shown as the main image. Superimposed are the FRODOSpec line profiles for  $H\alpha$  (top) and  $He\ II\ 4686\text{\AA}$  (bottom). The vertical lines show at which days the observations were taken after outburst.

confirming the general picture of the emergence of this line as the effective photospheric temperature rises and eventually reaches that sufficient to ionise He.

Also noteworthy is the fact that on day 65.6 KT Eri's X-ray emission softened dramatically which is also coincident with the change in the shape of the H $\alpha$  line profile from double-peaked on day 63.13 to a single peak on day 72.20. Figure 6.6 is an expansion of Figure 6.5 on days 60 to 80 after outburst. The line profile on day 67.26 still appears as a double peak with an absorption feature. It is also around this time that the He II 4686Å emission line becomes single peaked.

The change from double peak to single peak structure may be explored further from the evolution of the integrated flux ( $\text{erg s}^{-1} \text{cm}^{-2}$ ) of this line. Table 6.2 shows the integrated flux for the whole line profile, the integrated flux of just the core component, and their ratio. In Figure 6.7 the ratio of the H $\alpha$  components' integrated flux is compared with the evolution of the X-ray count rate.

What is evident from the ratio of the integrated fluxes is that it reduces with time up to day 65.2. Following this day there is an increase in the flux ratio, which then stays constant afterwards, around the same time the SSS softens dramatically. As the SSS is sampling the nuclear burning perhaps this increase in the ratio is due to material closer to the WD surface which has become visible since the ejecta become more optically thin. Therefore, the change in line profile may be associated with material nearer the WD becoming the dominant contributor to the line profile shape.

The strongest emission line is H $\alpha$  which is the one of interest for these studies for reasons noted in Chapters 4 and 5. As shown in Figure 6.8, and discussed extensively before, the line profile is double-peaked with broad wings. There appears little evolution of the line shape over time until day 67.26 when the profile appears to suffer some absorption on the blue side and by day 72.20 the line profile is single peaked although still with broad wings.

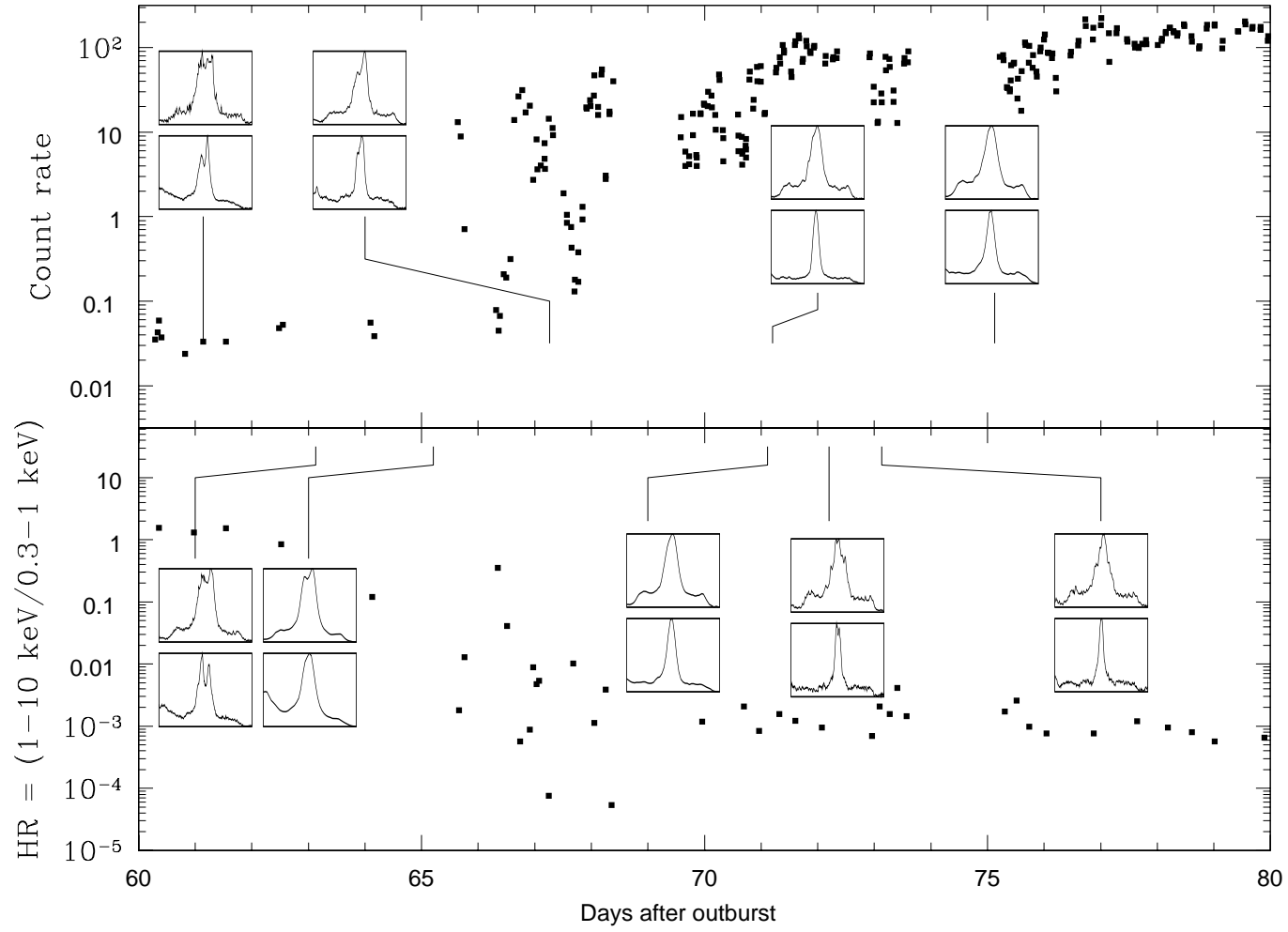


Figure 6.6: As Figure 6.5 for the region between days 60 and 80 after outburst.

Table 6.2: H $\alpha$  emission line integrated flux ( $\text{erg s}^{-1} \text{cm}^{-2}$ ) compared with solely core integrated flux and their ratio. The blank spaces are due to the fact that the FRODOSpec data are not flux calibrated so only the relative flux is taken.

days after outburst	Whole H $\alpha$	Core H $\alpha$	Ratio Whole/Core
17.25	5.063E-10	1.568E-10	3.23
21.17	4.359E-10	1.507E-10	2.89
31.14	1.703E-10	6.989E-11	2.44
33.21	1.426E-10	5.860E-11	2.43
42.29			2.01
46.25			2.04
47.20			1.88
48.16			1.90
49.15			1.83
50.15			2.03
51.15			1.87
53.09	4.866E-11	2.609E-11	1.87
54.20			1.74
58.16			1.67
59.14			1.62
61.14			1.53
63.13			1.62
65.21	2.784E-11	1.878E-11	1.48
67.26			1.90
71.11	9.432E-12	4.726E-12	2.00
71.20	9.435E-12	4.870E-12	1.94
72.20			1.96
73.13			1.96
75.13	7.193E-12	3.330E-12	2.16
80.16	3.947E-12	1.817E-12	2.17
84.18	4.797E-12	2.248E-12	2.13
91.22	4.757E-12	2.638E-12	1.80
98.15	3.075E-12	1.455E-12	2.11
122.14	3.057E-12	1.327E-12	2.30

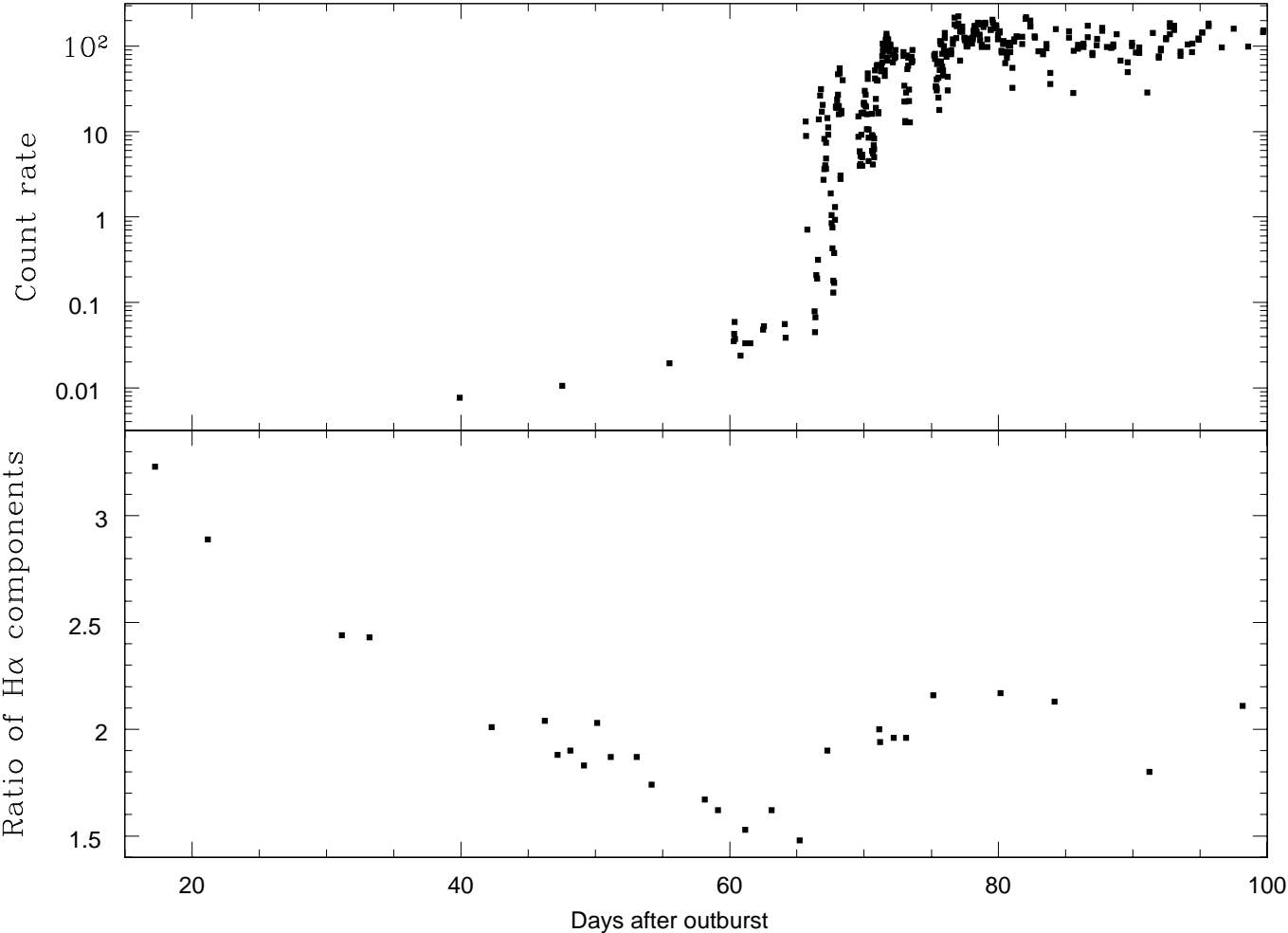
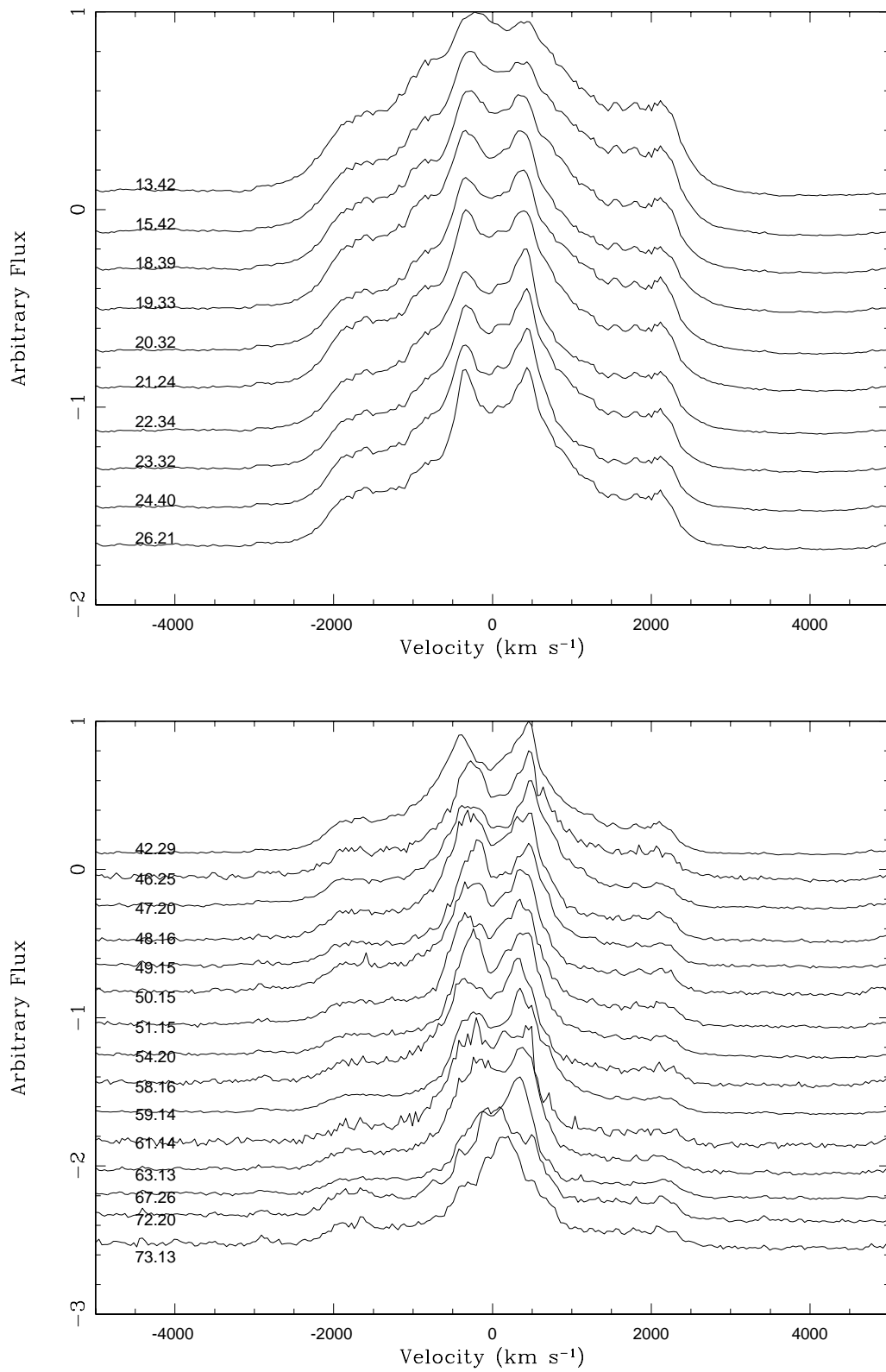


Figure 6.7: Comparison of the ratio of the H $\alpha$  components in Table 6.2 with the X-ray count rate.

Figure 6.8: As Figure 6.2 for the H $\alpha$  emission line.

## 6.4 Modelling Procedures

The previous Chapters have dealt with the issues surrounding modelling of emission lines. With continued development of SHAPE (see Chapter 2) different techniques were now implemented to see if similar results are achieved. Therefore, this Chapter uses the techniques already developed in the previous Chapters but with the addition of a new technique: the Optimizer Module (see Section 2.2.5 for a discussion).

Applying the previous geometry results to KT Eri, by comparing the observed spectra with the synthetic spectra of Chapters 4 and 5, did not provide a fit to the observations of the line profile shown in Figure 6.8. Therefore, it was realised that the structure had to be re-thought. The central double peak suggests extra emission and due to its associated low velocity this provides a handle on how prolate the structure is.

The apparent ratio of the wing width to the peak separation is 4:1 (Figure 6.8), therefore this is the size ratio taken between the major to minor axes and this is in essence the same as the dumbbell models described in previous chapters (Figure 6.9). The density was assumed to scale as  $1/r$ . The assumption of a  $1/r$  density profile was primarily driven due to the poor fits of the synthetic spectra from models described in of Chapters 4 and 5, and, as mentioned before, the central double peak suggested extra emission from material towards the centre of the remnant.

The first spectrum explored was that of day 42.29 after outburst and then the model was allowed to evolve to day 63.13 after outburst, always keeping the parameters for the inclination and maximum expansion velocity the same.

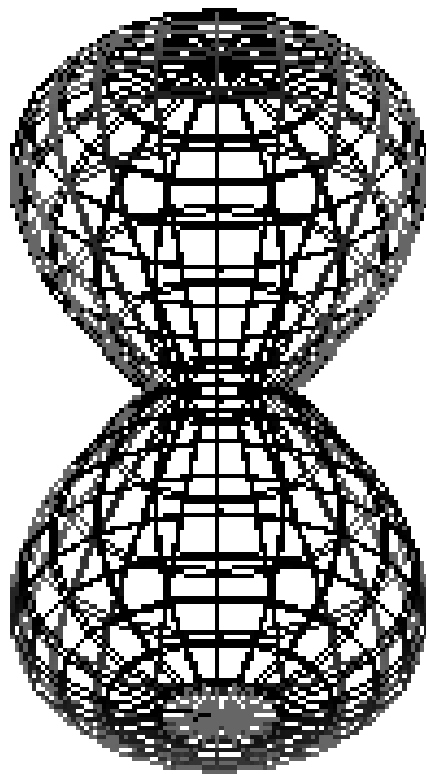


Figure 6.9: KT Eri's model mesh, as the input geometry, as visualised in SHAPE.

### 6.4.1 Previous techniques

As with the previous modelling the whole of the parameter space from  $0\text{--}90^\circ$  and  $V_{\text{exp}}$  ranging from  $100\text{--}8000\text{ km s}^{-1}$  (in steps of  $1^\circ$  and  $100\text{ km s}^{-1}$ , respectively) was explored. The models were run several times to produce a well sampled model spectrum. Then the model spectra were compared to the observed spectra and flux matched via  $\chi^2$  minimisation, using techniques from Press et al. (1992), to derive the best fitting inclination and maximum expansion velocity.

### 6.4.2 Optimizer module technique

This technique involved allowing SHAPE to find the best fit results for the structure described above. The parameters that were allowed to be optimized were the inclination and maximum expansion velocity. Allowing for more parameters to vary is not advisable and might produce unrealistic models. Therefore, when using this technique it is best to minimise the parameters by already assuming a physical model. Furthermore, this technique does not provide errors on the parameters and this has been requested to the developers for their next version.

## 6.5 Modelling Results

### 6.5.1 Early epoch observations ( $t = 42.29$ days)

The results of applying the previous techniques are shown in Figure 6.10. The best-fit result implies an inclination of  $i = 58_{-7}^{+6}$  degrees and a maximum expansion velocity  $V_{\text{exp}} = 2800 \pm 200\text{ km s}^{-1}$ . In comparison, adopting the optimizer technique, the best-fit result suggests an inclination  $i = 55^\circ$  and  $V_{\text{exp}} = 2800\text{ km s}^{-1}$  (Figure 6.11), i.e. well within the errors of the previous modelling technique.

With these fits, the optimizer module allows for a much reduced computational

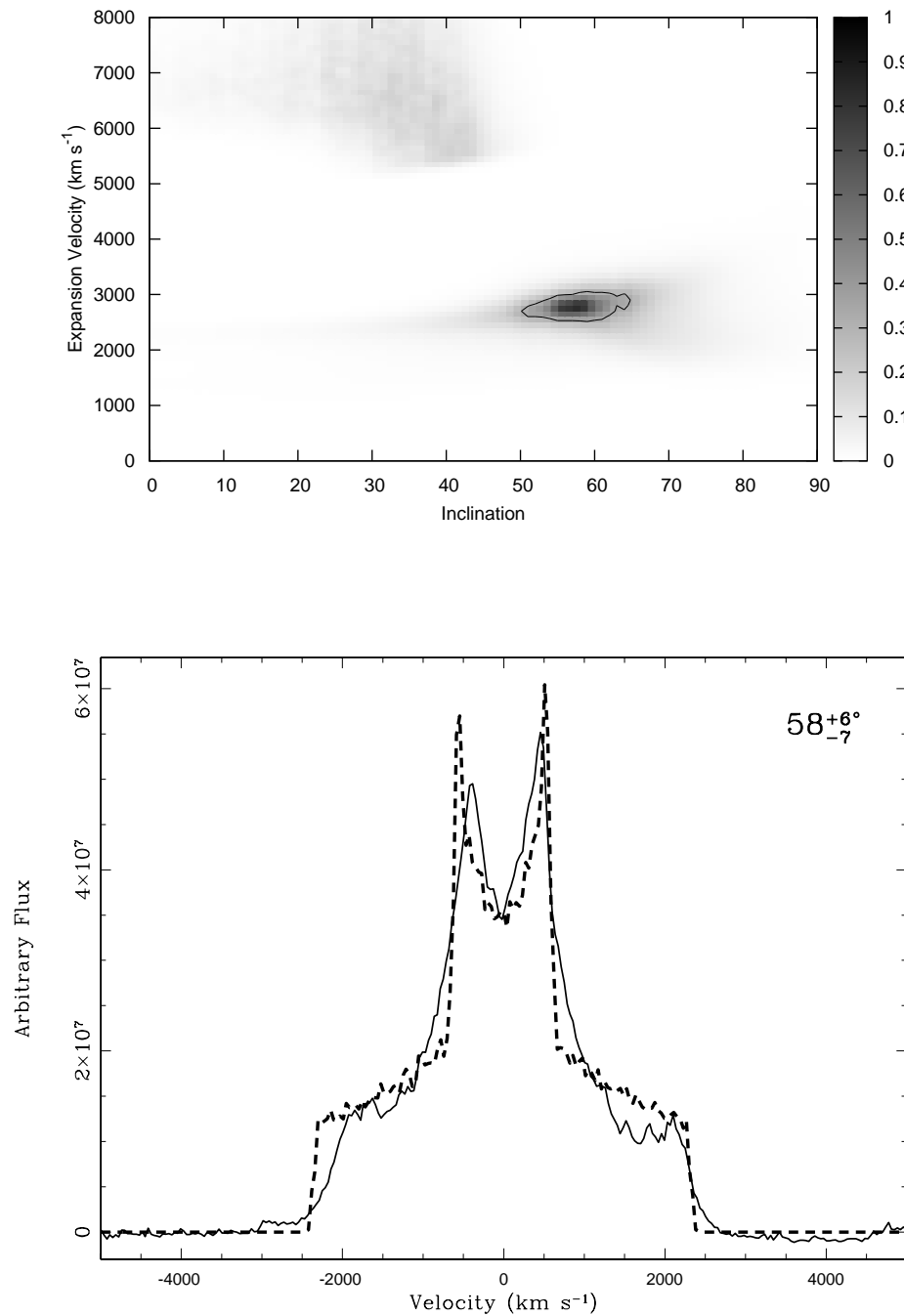


Figure 6.10: Best-fit model results of comparison between the observed and model spectrum using the techniques described in previous chapters. *Top* – the most likely result for the structure, where the grey scale represents the probability that the observed  $\chi^2$  value is correct. The solid line represents the one sigma boundary. Furthermore, the island at the high velocity end is due to the finite resolution (see Section 2.2.2). *Bottom* – The observed (solid black) and synthetic (dash black) spectra for the best-fit inclination, shown in the top right hand corner, with its respective one sigma errors.

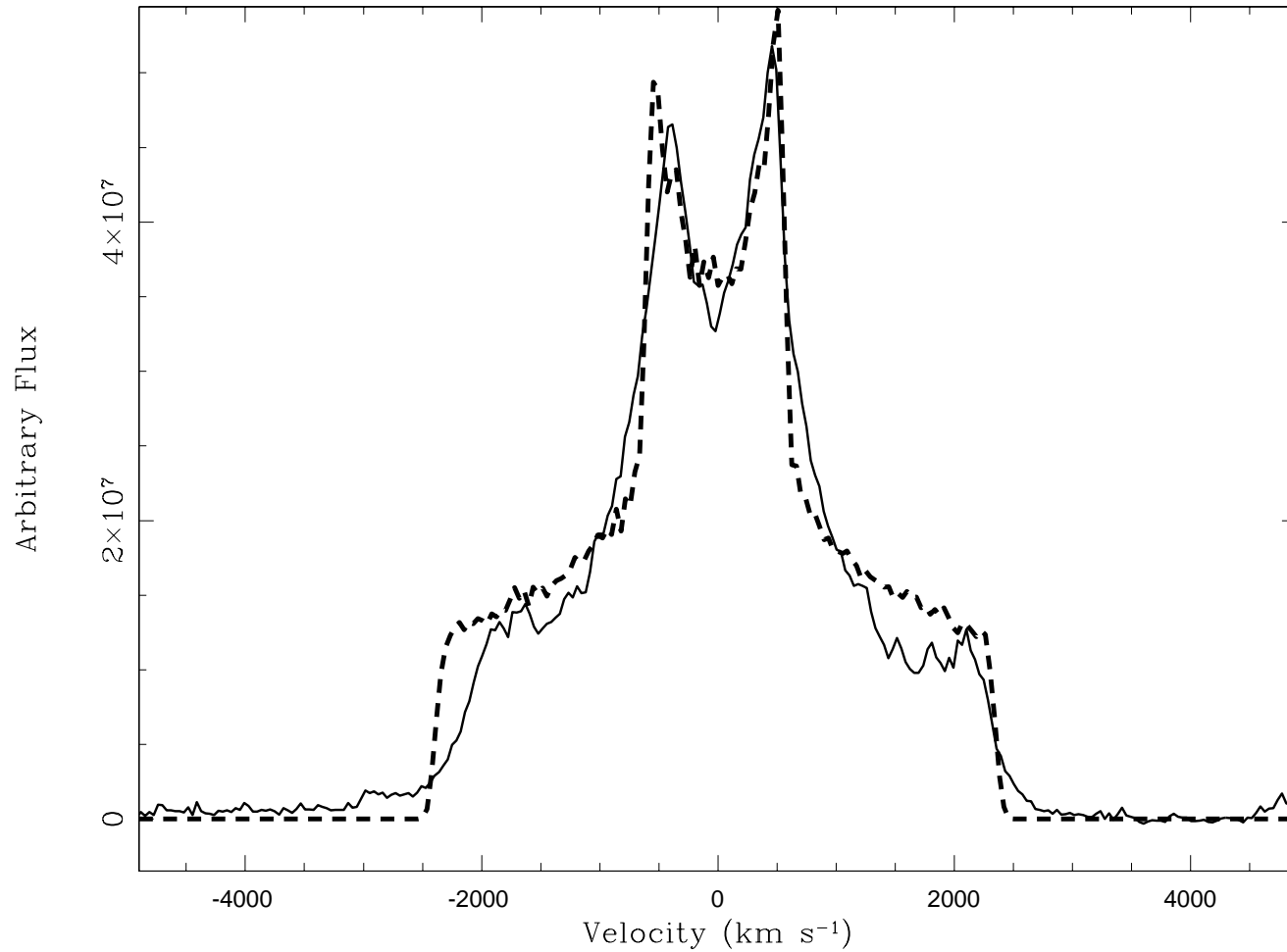


Figure 6.11: Best-fit result for the Optimizer module technique assuming a  $1/r$  density distribution. The observed (solid black) and synthetic (dashed black) spectra are compared. The results suggest an inclination of  $55^\circ$  and  $V_{\text{exp}} = 2800 \text{ km s}^{-1}$ .

time, and different parameters can be changed efficiently to see the effects on the spectrum. Therefore, a density distribution which varied as  $1/r^2$  was also considered (Figure 6.12). The result for this model suggests an inclination of  $51^\circ$  and  $V_{\text{exp}} = 3000 \text{ km s}^{-1}$ . Furthermore, for completeness a system with a constant density distribution was included (Figure 6.12). The best-fit result suggests an inclination of  $64^\circ$  and  $V_{\text{exp}} = 2600 \text{ km s}^{-1}$ . Figure 6.12 shows that these two are not very good fits and therefore, the derived best-fit density profile is that of a  $1/r$  distribution.

### 6.5.2 Later observations ( $t = 63.13$ days)

Taking the values for the inclination and maximum expansion velocity from the previous section, both  $1/r$  and  $1/r^2$  models were evolved to the later epoch observations (Figure 6.13).

Inspection of Figure 6.13 would suggest that the the profile results from a  $1/r^2$  density distribution to be the better fit. However, the modelling of this line is complicated by the fact that there is an evolution of the line profile shape as discussed in Section 6.3 (see also Figure 6.8).

## 6.6 Discussion

The results found in Section 6.3 for the emergence of the SSS are comparable with those found in the RN LMC 2009a with a marginal detection on day 63 after outburst (Bode et al. 2009c). This late emergence of the SSS in LMC 2009a was suggested to be due a higher mass loss rate and/or the ejection velocities were lower than in RS Oph and U Sco. In Section 6.5 KT Eri's expansion velocity was indeed shown to be much lower than both RS Oph and U Sco and the close similarities with LMC 2009a might lend support to a recurrent nature for KT Eri.

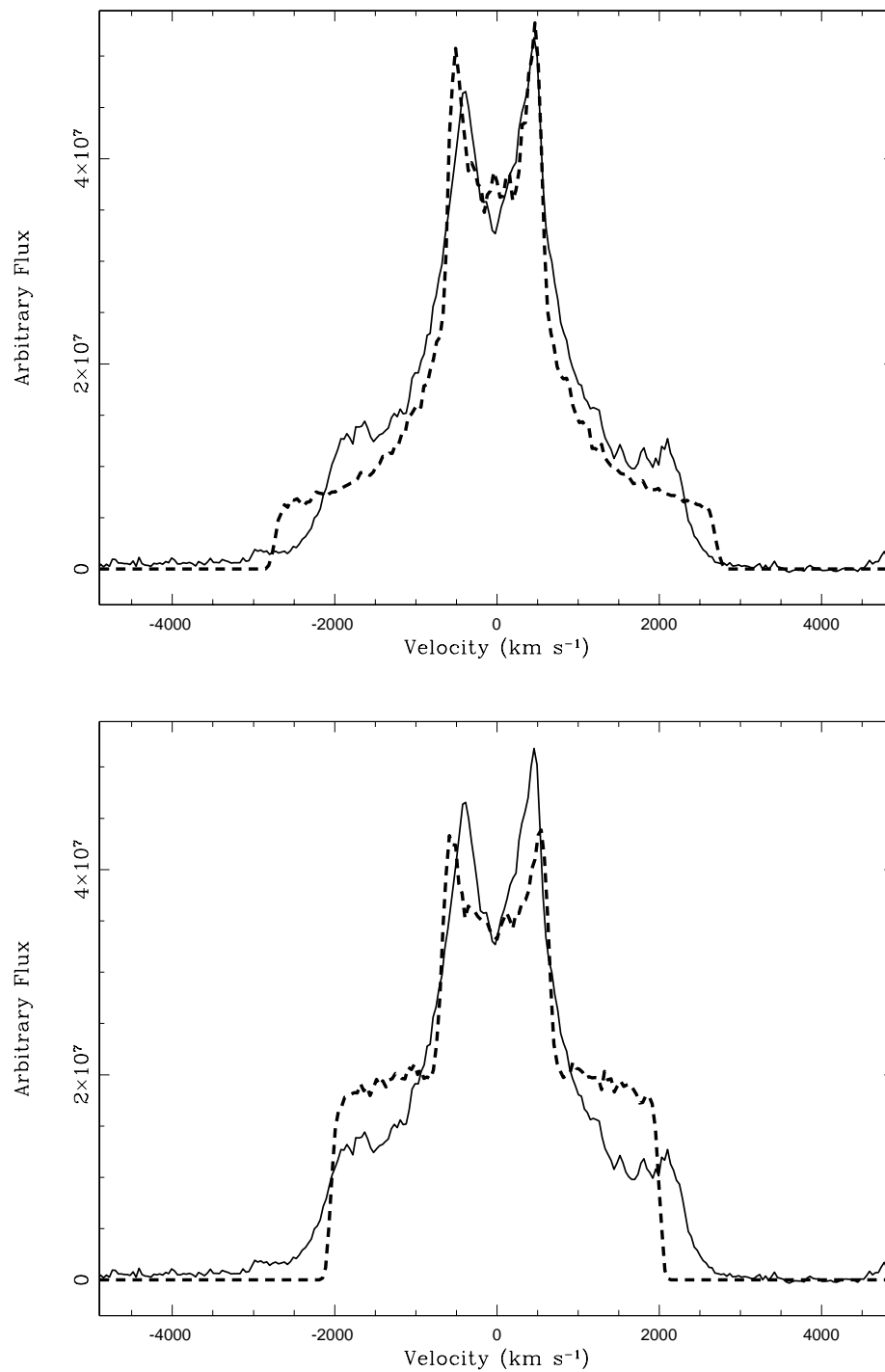


Figure 6.12: Best-fit result for the Optimizer module technique for the earlier epoch observations ( $t = 42.29$  days). *Top* – assuming a  $1/r^2$  density distribution, the results suggest an inclination of  $51^\circ$  and  $V_{\text{exp}} = 3000$  km s<sup>-1</sup>. *Bottom* – assuming a constant density distribution, the results suggest an inclination of  $64^\circ$  and  $V_{\text{exp}} = 2600$  km s<sup>-1</sup>. The observed (solid black) and synthetic (dashed black) spectra are compared.

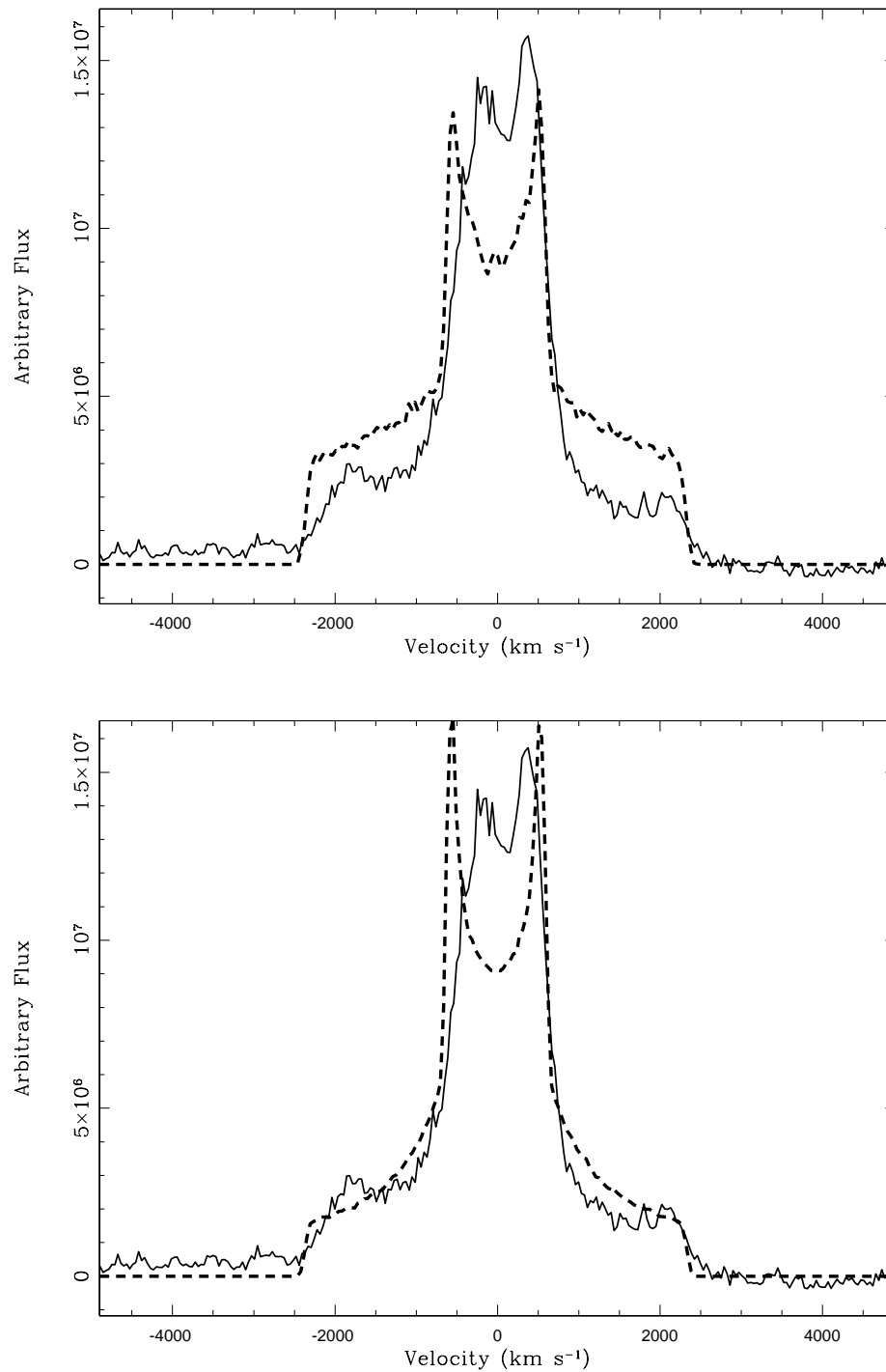


Figure 6.13: Best-fit results using the later epoch observations ( $t = 63.13$ ) using the Optimizer module technique assuming a  $1/r$  (top) and  $1/r^2$  (bottom) density distribution. The observed (solid black) and synthetic (dashed black) spectra are compared

The emergence of the He II 4684Å line is suggested to immediately precede the emergence of the SSS phase, which can be used in future observations of novae as a trigger for X-ray observations. Furthermore, the development of H $\alpha$  was very interesting and most likely related to the evolution of the X-ray behaviour. For example, it was suggested that the change in the line ratio between the different H $\alpha$  components was evidence for the emergence of emitting material closer to the WD surface which becomes visible as the ejecta become more optically thin.

Using the observed H $\alpha$  line profile on day 42.29, KT Eri was modelled with a dumbbell shape (Figure 6.9) with a  $1/r$  density profile,  $V_{\text{exp}} = 2800 \pm 200$  km s $^{-1}$  and inclination angle of  $58_{-7}^{+6}$  degrees. This was also confirmed using the Optimizer technique which significantly improves computing time.

The later epoch line profile (day 63.13) was modelled with a  $1/r^2$  density profile however, although caution should be exercised here following the discussion in Section 6.3 on the evolution of the line profile. As Figure 6.6 shows the central regions of the line gain in intensity compared with the whole profile. This is interpreted as arising from material closer to the WD as the ejecta become optically thin.

In the next Chapter a summary of the results found in this work and suggestions for future work are presented.

# Chapter 7

## Summary and Future Work

### 7.1 Summary

Work in this thesis has predominantly involved morpho-kinematical modelling of novae after outburst to derive important parameters, including the geometry, of the nova outburst. Initially the work considered *HST* resolved imaging which combined with ground-based spectroscopic observations provided important parameters of the RS Oph remnant. The structure found for RS Oph, along with other structures proposed from previous published literature, was then used on different novae to derive their 3D geometries from which information including the remnant inclination and expansion velocity were derived using solely spectroscopic observations. Caution was exercised due to the nature of the  $H\alpha$  emission line which in some of the cases was very early after outburst and therefore possibly optically thick, although the symmetry of the line in some objects suggested that at the time of the observations it was optically thin. Over all, this work also demonstrates that the 3D geometry of nova shells is not simply spherically expanding and therefore this should be accounted for in other more detailed work.

In this Chapter a brief summary of the main results are presented and related to the wider community and then future work to enhance the results are proposed.

### 7.1.1 RS Ophiuchi

The results of the studies of the RN RS Oph remnant are summarised as:

1. The remnant of RS Oph can be understood as a bipolar structure with two co-aligned components. These components are found to be an outer dumbbell structure and an inner, denser, hour glass, both required to satisfactorily model the observed *HST* image and the spectrum at the first epoch. This morphology is in agreement with that inferred from observations in the radio and at X-ray wavelengths, plus infrared interferometry at early times.
2. The asymmetry observed in the first epoch *HST* image was shown to be due to the finite width and offset in the central wavelength of the *HST* filter. This in turn implies that the west lobe is approaching the observer, in agreement with the results from infrared interferometry at early times.
3. The inclination of the system was derived to be  $39_{-10}^{+1}$  degrees, comparable with estimates of the inclination of the central binary and thus emphasising the link between the central system and evolving geometry of the remnant.
4. The second epoch observations and modelling suggested that the outer dumbbell structure expanded linearly. However, there was evidence for deceleration in the inner hour glass.
5. X-ray imaging with *Chandra* around 1.5 years after outburst showed an extended feature which appeared to lie on top of an optical artifact observed on the second epoch *HST* observations. It was demonstrated that the scale sizes were not in line with a linear expansion in the optical however, although a much later *Chandra* observation is in line with the optical expansion.

### 7.1.2 V2491 Cygni

By investigating four potential morphologies for V2491 Cyg it was found that two of the structures presented similar probabilities of being correct at early times. By fitting to two different epochs it was possible to determine the most likely morphology as that of polar blobs and an equatorial ring, with an implied inclination of the system of  $80_{-12}^{+3}$  degrees and a maximum expansion velocity of the polar blobs of  $3100_{-100}^{+200}$  km s<sup>-1</sup> and for the equatorial ring  $2700_{-100}^{+200}$  km s<sup>-1</sup>. Multi epoch fitting showed that the line profile at later times consisted of a combination of H $\alpha$  and [N II] emission. A search for eclipses is now underway, which if found will enable us to determine more precisely important parameters of the central binary. Furthermore, the outburst amplitude versus  $t_2$  suggest that this system may be a recurrent nova.

### 7.1.3 V2672 Ophiuchi

Applying the techniques used from V2491 Cyg, the 3D geometry of V2672 Oph was constrained as a combination of polar blobs and an equatorial ring with an underlying prolate morphology which seemed to reduce in relative density with time compared to the other components. The inclination of the system was suggested to be  $0 \pm 6^\circ$  and a maximum expansion velocity  $V_{\text{exp}} = 4800_{-800}^{+900}$  km s<sup>-1</sup>.

The fact that no 2MASS counterpart was found at the position of the nova suggested a system similar to the U Sco-type Recurrent Nova. Other similarities to U Sco included V2672 Oph's very fast decline from maximum, a plateau phase and "He/N" spectral classification. The velocities derived are also comparable to U Sco although the inclinations derived very somewhat different.

### 7.1.4 KT Eridani

The optical spectral evolution of KT Eri was explored. The emergence of the He II 4686Å line appears related to that of the SSS phase in the X-ray. This might be a useful tool as a trigger for future X-ray observations. Line profile evolution was also explored. The H $\alpha$  line profile was reasonably constant until the X-ray source softened dramatically and then became single peaked. This change in line profile was suggested to be due to more material closer to the WD becoming observable as the ejecta become optically thin.

The morphology of the expanding remnant was also constrained. Here the best-fit geometry was as a dumbbell with a ratio between the major to minor axis of 4:1 and a 1/r density distribution. The remnant inclination was suggested to be  $58_{-7}^{+6}$  degrees and a maximum expansion velocity  $V_{\text{exp}} = 2800 \pm 200 \text{ km s}^{-1}$ . The morphology, which is reminiscent of the RN RS Oph, and photometric similarities to the RN LMC 2009a, could lend support to KT Eri's recurrent nova nature.

## 7.2 Conclusions

The work described here applied morpho-kinematical modelling to observations of the early stages of the expanding morphology of several novae. The results were related to the nature of the central binary and was found that the supposed CNe had aspects which may suggest they are more akin to RNe. The investigation of RNe is in turn important for work on progenitors of Type Ia SNe.

Furthermore, these studies are important for the understanding of pPNe where morphologies may arise from binary interactions. However, in novae, the timescale of evolution is much less than that of pPNe and can be studied in “real time”.

## 7.3 Future work

### 7.3.1 RS Ophiuchi

Although detailed modelling was performed as described in Chapter 3, this only concentrated on the [O III] 5007Å emission line primarily due to the availability of two epochs of *HST* imaging. One of the open questions this work has left is what really happens at the second epoch? Are we for example indeed observing a deceleration of the central component?

A search of the archive of the Isaac Newton Group of Telescopes proved fruitful in finding some spectra on 2007 March 8 (day 390 after outburst). This observation was taken with the ISIS instrument on the William Herschel Telescope. ISIS is a high-efficiency, double-armed, medium-resolution (8-120 Å/mm) spectrograph. The observations of interest are those of the blue arm (grating R300B) with a dispersion of 0.86 Å/pix which equates to around 52 km s<sup>-1</sup> at 5007Å. This is a reasonable resolution to enable modelling of the system.

A further literature search showed some published material that included spectra of the [Ne v] 3426Å line 201 days after the 1986 outburst (Bohigas et al. 1989). Considering that the two outbursts occurred at similar phase (Brandi et al. 2009) and had shown similar behaviour (Evans et al. 2008) the 1986 observations can be used to help model the [Ne v] *HST* image and compare this to the results found in Chapter 3. The observations were taken at the Observatorio Astronómico Nacional at San Pedro Mártir, Baja California, México with the Mepsicron detector at the 2.12m telescope. The observations were taken with a resolution of about 9Å which equates to around 800 km s<sup>-1</sup> at 3426Å, which is rather low resolution. However, some structure to the line is observed.

### 7.3.2 V2672 Ophiuchi

V2672 Oph presented many spectral and photometric similarities to the RN U Sco. In this work it was interpreted as a pole-on system. However, other authors, although also interpreting as a U Sco type, suggest that it is edge on (F. Walter, private communication). If this is a system similar to U Sco, then the orbital period should be of order days and eclipses should be observed. Such observations will be a stringent test of the competing models of this object's orientation.

### 7.3.3 KT Eridani

One of the interesting outcomes of Chapter 6 is the probe of the SSS phase. Some further work should be done on this to explore other CNe, and RNe, to see if the changes observed in the spectrum are also common in these systems. The spectra provided by collaborators are of good quality to observe other emission lines. These might be useful in connecting to the observed changes. Furthermore, additional detailed comparison of KT Eri's X-ray behaviour with that of the RN LMC 2009a could prove valuable to determine the likely nature of the nova.

A search of the 2MASS catalog showed a bright source at the position of KT Eri. Exploring this further could also prove fruitful to determine the likely nature of the progenitor system.

### 7.3.4 Further user suggestions to enhance SHAPE

SHAPE was extensively used for this work with much communication between the user and developers. Some developments that would have improved the computational time of the work presented here would have included the possibility of more automation and parallelisation. For example, several of the figures showing results in Chapters 4 and 5 arose from 36000 model runs for each model. Most of

the time this was achieved by running the code on several machines. Therefore, if the code had been able to take advantage of parallel cores, which it does now, the run time could have been drastically reduced. Although, parallelisation only affects the renderer module and not yet the animation module, this would be a feature to be requested for future development.

Another development closely tied to this would be the ability to remove the graphical interface and run the model on the command line, this would therefore take advantage of cluster machines.

However, it should be noted that the optimizer module should take care of some of the above issues. Furthermore, the requirements of the wider community using SHAPE probably do not generally need this to be fully automated.

### 7.3.5 Spatially resolving remnants

As demonstrated in Chapter 3 the best way to constrain any model is by spatially resolving the remnants. However, this is hindered by several factors for example, the distance to the nova and surface brightness.

KT Eri currently is around 15th mag in  $V$ . Assuming the distance of 6.5 kpc, expansion velocity of  $2800 \text{ km s}^{-1}$  and resolvable size of around 0.1 arcsec, and using Equation 1.5, KT Eri would be resolved around 1.1 years after outburst. For example, the WFP3/UVIS has a pixel size of 0.04 arcsec. This means the nova remnant could be observed now. This would also allow the determination of the distance via expansion parallax.

Taking into account the time since the last detailed *HST* imaging of novae and the additional knowledge gained on several objects (including that derived in this thesis), there is sufficient scientific motivation to justify a renewed program of *HST* observations of nova remnants. This would ideally be a combination of imaging and spatially resolved spectroscopy.

# References

- Anupama, G. C. 2002, in American Institute of Physics Conference Series, Vol. 637, Classical Nova Explosions, ed. M. Hernanz & J. José, 32
- Anupama, G. C. & Dewangan, G. C. 2000, *AJ*, 119, 1359
- Anupama, G. C. & Mikolajewska, J. 1999, *A&A*, 344, 177
- Ayani, K. & Matsumoto, K. 2008, Central Bureau Electronic Telegrams, 1334
- Ayani, K., Murakami, N., Hata, K., Tanaka, A., Tachibana, M., & Kanda, A. 2009, Central Bureau Electronic Telegrams, 1911
- Baklanov, A., Pavlenko, E., & Berezina, E. 2008, *The Astronomer's Telegram*, 1514
- Banerjee, D. P. K., Das, R. K., & Ashok, N. M. 2009, *MNRAS*, 399, 357
- Barry, R. K., Mukai, K., Sokoloski, J. L., Danchi, W. C., Hachisu, I., Evans, A., Gehrz, R., & Mikolajewska, J. 2008, in *Astronomical Society of the Pacific Conference Series*, Vol. 401, *Astronomical Society of the Pacific Conference Series*, ed. A. Evans, M. F. Bode, T. J. O'Brien, & M. J. Darnley, 52
- Bath, G. T. & Harkness, R. P. 1989, in *Classical Novae*, ed. M. F. Bode & A. Evans, p. 61
- Bianchini, A., Mastrantonio, E., Canterna, R., Stute, J., & Cantrell, K. 2004, *A&A*, 426, 669

- Bode, M. F. 1987, in RS Ophiuchi (1985) and the Recurrent Nova Phenomenon, ed. M. F. Bode, p. 241
- Bode, M. F. 2002, in American Institute of Physics Conference Series, Vol. 637, Classical Nova Explosions, ed. M. Hernanz & J. José, 497
- Bode, M. F., Darnley, M. J., Shafter, A. W., Page, K. L., Smirnova, O., Anupama, G. C., & Hilton, T. 2009a, *ApJ*, 705, 1056
- Bode, M. F. & Evans, A. 2008, editors *Classical Novae*, 2nd Edition (Cambridge University Press)
- Bode, M. F., Harman, D. J., O'Brien, T. J., Bond, H. E., Starrfield, S., Darnley, M. J., Evans, A., & Eyres, S. P. S. 2007, *ApJL*, 665, L63
- Bode, M. F., O'Brien, T. J., Osborne, J. P., Page, K. L., Senziani, F., Skinner, G. K., Starrfield, S., Ness, J.-U., Drake, J. J., Schwarz, G., Beardmore, A. P., Darnley, M. J., Eyres, S. P. S., Evans, A., Gehrels, N., Goad, M. R., Jean, P., Krautter, J., & Novara, G. 2006, *ApJ*, 652, 629
- Bode, M. F., Osborne, J. P., Page, K. L., Beardmore, A. P., Ness, J.-U., Walter, F. M., Darnley, M. J., Evans, A., Eyres, S. P. S., Krautter, J., O'Brien, T. J., Orío, M., Schwarz, G., Starrfield, S., & Truran, J. 2009b, *The Astronomer's Telegram*, 2001
- . 2009c, *The Astronomer's Telegram*, 2025
- Bode, M. F., Osborne, J. P., Page, K. L., Beardmore, A. P., Walter, F. M., Ness, J.-U., Schwarz, G., Starrfield, S., Kuulkers, E., O'Brien, T. J., Balman, S., Darnley, M. J., Evans, A., Evans, P., Eyres, S. P. S., & Krautter, J. 2010, *The Astronomer's Telegram*, 2392
- Boehm-Vitense, E. 1981, *ARA&A*, 19, 295
- Bohigas, J., Echevarria, J., Diego, F., & Sarmiento, J. A. 1989, *MNRAS*, 238, 1395

- Brandi, E., Quiroga, C., Mikołajewska, J., Ferrer, O. E., & García, L. G. 2009, *A&A*, 497, 815
- Buil, C. 2006, *Central Bureau Electronic Telegrams*, 403
- Cassisi, S., Iben, I. J., & Tornambe, A. 1998, *ApJ*, 496, 376
- Chesneau, O. 2008, in *Astronomical Society of the Pacific Conference Series*, Vol. 401, *Astronomical Society of the Pacific Conference Series*, ed. A. Evans, M. F. Bode, T. J. O'Brien, & M. J. Darnley, 231
- Chesneau, O., Nardetto, N., Millour, F., Hummel, C., Domiciano de Souza, A., Bonneau, D., Vannier, M., Rantakyrö, F., Spang, A., Malbet, F., Mourard, D., Bode, M. F., O'Brien, T. J., Skinner, G., Petrov, R. G., Stee, P., Tatulli, E., & Vakili, F. 2007, *A&A*, 464, 119
- Cohen, J. G. 1985, *ApJ*, 292, 90
- Crawford, J. A. & Kraft, R. P. 1956, *ApJ*, 123, 44
- della Valle, M., Pasquini, L., Daou, D., & Williams, R. E. 2002, *A&A*, 390, 155
- Dobrzycka, D. & Kenyon, S. J. 1994, *AJ*, 108, 2259
- Downes, R. A. & Duerbeck, H. W. 2000, *AJ*, 120, 2007
- Drake, A. J., Djorgovski, S. G., Graham, M. J., Mahabal, A. A., Williams, R., Wils, P., Greaves, J., Catelan, M., Prieto, J., Beshore, E. C., Larson, S. M., Boattini, A., Gibbs, A., Grauer, A., Hill, R., Kowalski, R., & Christensen, E. 2009, *The Astronomer's Telegram*, 2331
- Drake, J. J. & Orlando, S. 2010, *ApJL*, 720, L195
- Duerbeck, H. W. 2008, in *Classical Novae*, 2nd Edition, ed. M. F. Bode & A. Evans (Cambridge University Press), p. 1
- Dumm, T. & Schild, H. 1998, *New Astron.*, 3, 137

- Evans, A., Bode, M. F., O'Brien, T. J., & Darnley, M. J., eds. 2008, *Astronomical Society of the Pacific Conference Series*, Vol. 401, RS Ophiuchi (2006) and the Recurrent Nova Phenomenon
- Evans, A., Tyne, V. H., Smith, O., Geballe, T. R., Rawlings, J. M. C., & Eyres, S. P. S. 2005, *MNRAS*, 360, 1483
- Eyres, S. P. S., O'Brien, T. J., Beswick, R., Muxlow, T. W. B., Anupama, G. C., Kantharia, N. G., Bode, M. F., Gawroński, M. P., Feiler, R., Evans, A., Rush-ton, M. T., Davis, R. J., Prabhu, T., Porcas, R., & Hassall, B. J. M. 2009, *MNRAS*, 395, 1533
- Fekel, F. C., Joyce, R. R., Hinkle, K. H., & Skrutskie, M. F. 2000, *AJ*, 119, 1375
- Fruchter, A. & Hook, R. N. 1997, in *Society of Photo-Optical Instrumentation Engineers (SPIE) Conference Series*, Vol. 3164, *Society of Photo-Optical Instrumentation Engineers (SPIE) Conference Series*, ed. A. G. Tescher, 120
- Gallagher, J. S. & Starrfield, S. 1978, *ARA&A*, 16, 171
- Gehrels, N., Chincarini, G., Giommi, P., Mason, K. O., Nousek, J. A., Wells, A. A., White, N. E., Barthelmy, S. D., Burrows, D. N., Cominsky, L. R., Hurley, K. C., Marshall, F. E., Mészáros, P., Roming, P. W. A., Angelini, L., Barbier, L. M., Belloni, T., Campana, S., Caraveo, P. A., Chester, M. M., Citterio, O., Cline, T. L., Cropper, M. S., Cummings, J. R., Dean, A. J., Feigelson, E. D., Fenimore, E. E., Frail, D. A., Fruchter, A. S., Garmire, G. P., Gendreau, K., Ghisellini, G., Greiner, J., Hill, J. E., Hunsberger, S. D., Krimm, H. A., Kulkarni, S. R., Kumar, P., Lebrun, F., Lloyd-Ronning, N. M., Markwardt, C. B., Mattson, B. J., Mushotzky, R. F., Norris, J. P., Osborne, J., Paczynski, B., Palmer, D. M., Park, H., Parsons, A. M., Paul, J., Rees, M. J., Reynolds, C. S., Rhoads, J. E., Sasseen, T. P., Schaefer, B. E., Short, A. T., Smale, A. P., Smith, I. A., Stella, L., Tagliaferri, G., Takahashi, T., Tashiro, M., Townsley, L. K., Tueller, J., Turner, M. J. L., Vietri, M., Voges, W., Ward, M. J., Willingale, R., Zerbi, F. M., & Zhang, W. W. 2004, *ApJ*, 611, 1005

- Gill, C. D. & O'Brien, T. J. 1998, *MNRAS*, 300, 221
- . 1999, *MNRAS*, 307, 677
- . 2000, *MNRAS*, 314, 175
- Guido, E., Sostero, G., Maehara, H., & Fujii, M. 2009, Central Bureau Electronic Telegrams, 2053
- Hachisu, I. & Kato, M. 2009, *ApJL*, 694, L103
- Hachisu, I., Kato, M., Kato, T., & Matsumoto, K. 2002, in *Astronomical Society of the Pacific Conference Series*, Vol. 261, *The Physics of Cataclysmic Variables and Related Objects*, ed. B. T. Gänsicke, K. Beuermann, & K. Reinsch, 629
- Harman, D. J. 2001, PhD thesis, The University of Manchester
- Harman, D. J. & O'Brien, T. J. 2003, *MNRAS*, 344, 1219
- Henden, A. & Munari, U. 2008, *Information Bulletin on Variable Stars*, 5834
- Hernanz, M. & Sala, G. 2002, *Science*, 298, 393
- Hick, P., Buffington, A., & Jackson, B. V. 2007, *Solar Physics and Space Weather Instrumentation II*, 6689, 66890C
- Högbom, J. A. 1974, *A&AS*, 15, 417
- Holloway, A. J., Steffen, W., Pedlar, A., Axon, D. J., Dyson, J. E., Meaburn, J., & Tadhunter, C. N. 1996, *MNRAS*, 279, 171
- Horne, K. & Marsh, T. R. 1986, *MNRAS*, 218, 761
- Hounsell, R., Bode, M. F., Hick, P. P., Buffington, A., Jackson, B. V., Clover, J. M., Shafter, A. W., Darnley, M. J., Mawson, N. R., Steele, I. A., Evans, A., Eyres, S. P. S., & O'Brien, T. J. 2010, *ApJ*, 724, 480
- Hubble, E. P. 1929, *ApJ*, 69, 103

- Hutchings, J. B. 1972a, Publications of the Dominion Astrophysical Observatory Victoria, 14, 59
- . 1972b, MNRAS, 158, 177
- Hyland, A. R. & Neugebauer, G. 1970, ApJL, 160, L177
- Ibarra, A. & Kuulkers, E. 2008, The Astronomer's Telegram, 1473
- Ibarra, A., Kuulkers, E., Beardmore, A., Evans, P., Mukai, K., Ness, J.-U., Orío, M., Osborne, J. P., Page, K. L., Saxton, R., Starrfield, S., & Tueller, J. 2008, The Astronomer's Telegram, 1478
- Ibarra, A., Kuulkers, E., Osborne, J. P., Page, K., Ness, J.-U., Saxton, R. D., Baumgartner, W., Beckmann, V., Bode, M. F., Hernanz, M., Mukai, K., Orío, M., Sala, G., Starrfield, S., & Wynn, G. A. 2009, A&A, 497, L5
- Jurdana-Sepic, R. & Munari, U. 2008, Information Bulletin on Variable Stars, 5839
- Kenyon, S. J. 1986, The symbiotic stars (Cambridge University Press), p. 295
- Kenyon, S. J. 1988, in Astrophysics and Space Science Library, Vol. 145, IAU Colloq. 103: The Symbiotic Phenomenon, ed. J. Mikolajewska, M. Friedjung, S. J. Kenyon, & R. Viotti, 11
- Kenyon, S. J. & Truran, J. W. 1983, ApJ, 273, 280
- King, A. R. & Watson, M. G. 1987, MNRAS, 227, 205
- King, A. R., Whitehurst, R., & Frank, J. 1990, MNRAS, 244, 731
- Kiss, L. L., Thomson, J. R., Ogloza, W., Furész, G., & Sziládi, K. 2001, A&A, 366, 858
- Knigge, C., King, A. R., & Patterson, J. 2000, A&A, 364, L75
- Kraft, R. P. 1964, ApJ, 139, 457

- Krauss Hartman, M. I., Rupen, M. P., & Mioduszewski, A. J. 2009, *The Astronomer's Telegram*, 2195
- Krist, J. 1995, in *Astronomical Society of the Pacific Conference Series*, Vol. 77, *Astronomical Data Analysis Software and Systems IV*, ed. R. A. Shaw, H. E. Payne, & J. J. E. Hayes, 349
- Kwok, S. 1997, in *Astronomical Society of the Pacific Conference Series*, Vol. 130, *The Third Pacific Rim Conference on Recent Development on Binary Star Research*, ed. K.-C. Leung, 163
- Liller, W. 2009, *IAU Circ.*, 9019
- Livio, M. 2000, in *Type Ia Supernovae, Theory and Cosmology*, ed. J. C. Niemeyer & J. W. Truran (Cambridge University Press), p. 33
- Livio, M., Shankar, A., Burkert, A., & Truran, J. W. 1990, *ApJ*, 356, 250
- Lloyd, H. M., Bode, M. F., O'Brien, T. J., & Kahn, F. D. 1993, *MNRAS*, 265, 457
- Lloyd, H. M., O'Brien, T. J., & Bode, M. F. 1997, *MNRAS*, 284, 137
- Lucy, L. B. 1974, *AJ*, 79, 745
- Luna, G. J. M., Montez, R., Sokoloski, J. L., Mukai, K., & Kastner, J. H. 2009, *ApJ*, 707, 1168
- Luthardt, R. 1992, in *Reviews in Modern Astronomy*, Vol. 5, *Reviews in Modern Astronomy*, ed. G. Klare, 38
- Mastrodemos, N. & Morris, M. 1999, *ApJ*, 523, 357
- McLaughlin, D. B. 1939, *Popular Astronomy*, 47, 410
- . 1945, *PASP*, 57, 69
- McLaughlin, D. B. 1960, in *Stellar Atmospheres*, ed. J. L. Greenstein (University of Chicago Press), p. 585

- Mennickent, R. E. & Honeycutt, R. K. 1995, *Informational Bulletin on Variable Stars*, 4232
- Morales-Rueda, L., Carter, D., Steele, I. A., Charles, P. A., & Worswick, S. 2004, *Astronomische Nachrichten*, 325, 215
- Munari, U., Dallaporta, S., & Castellani, F. 2010, *Information Bulletin on Variable Stars*, 5930
- Munari, U., Ribeiro, V. A. R. M., Bode, M. F., & Saguner, T. 2011a, *MNRAS*, 410, 525
- Munari, U., Saguner, T., Ochner, P., Siviero, A., Maitan, A., Valisa, P., Dallaporta, S., & Moretti, S. 2009, *Central Bureau Electronic Telegrams*, 1912
- Munari, U., Siviero, A., Dallaporta, S., Cherini, G., Valisa, P., & Tomasella, L. 2011b, *New Astron.*, 16, 209
- Munari, U. & Whitelock, P. A. 1989, *MNRAS*, 239, 273
- Munari, U., Zwitter, T., Tomov, T., Bonifacio, P., Molaro, P., Selvelli, P., Tomasella, L., Niedzielski, A., & Pearce, A. 1999, *A&A*, 347, L39
- Nakano, S., Beize, J., Jin, Z.-W., Gao, X., Yamaoka, H., Haseda, K., Guido, E., Sostero, G., Klingenberg, G., & Kadota, K. 2008, *IAU Circ.*, 8934
- Nakano, S., Yamaoka, H., & Kadota, K. 2009, *Central Bureau Electronic Telegrams*, 1910
- Narumi, H., Hirosawa, K., Kanai, K., Renz, W., Pereira, A., Nakano, S., Nakamura, Y., & Pojmanski, G. 2006, *IAU Circ.*, 8671
- O'Brien, T. J., Beswick, R. J., Bode, M. F., Eyres, S. P. S., Muxlow, T. W. B., Garrington, S. T., Porcas, R. W., Evans, A., & Davis, R. J. 2008, in *Astronomical Society of the Pacific Conference Series*, Vol. 401, *Astronomical Society of the Pacific Conference Series*, ed. A. Evans, M. F. Bode, T. J. O'Brien, & M. J. Darnley, 239

- O'Brien, T. J. & Bode, M. F. 2008, in *Classical Novae*, 2nd Edition, ed. M. F. Bode & A. Evans, Cambridge: Cambridge University Press, p. 285
- O'Brien, T. J., Bode, M. F., Porcas, R. W., Muxlow, T. W. B., Eyres, S. P. S., Beswick, R. J., Garrington, S. T., Davis, R. J., & Evans, A. 2006, *Nature*, 442, 279
- O'Brien, T. J., Lloyd, H. M., & Bode, M. F. 1994, *MNRAS*, 271, 155
- O'Brien, T. J., Muxlow, T. W. B., Stevens, J., Datta, A., Roy, N., Eyres, S. P. S., & Bode, M. F. 2010, *The Astronomer's Telegram*, 2434
- Oppenheimer, B. D. & Mattei, J. A. 1993, *Journal of the American Association of Variable Star Observers (JAAVSO)*, 22, 105
- Orlando, S., Drake, J. J., & Laming, J. M. 2009, *A&A*, 493, 1049
- Padin, S., Davis, R. J., & Bode, M. F. 1985, *Nature*, 315, 306
- Page, K. L., Osborne, J. P., Evans, P. A., Wynn, G. A., Beardmore, A. P., Starling, R. L. C., Bode, M. F., Ibarra, A., Kuulkers, E., Ness, J., & Schwarz, G. J. 2010, *MNRAS*, 401, 121
- Pagnotta, A., Schaefer, B. E., Xiao, L., Collazzi, A. C., & Kroll, P. 2009, *AJ*, 138, 1230
- Payne-Gaposchkin, C. H. 1957, *The galactic novae* (Amsterdam, North-Holland Pub. Co.; New York, Interscience Publishers)
- Porcas, R. W., Davis, R. J., & Graham, D. A. 1987, in *RS Ophiuchi (1985) and the Recurrent Nova Phenomenon*, ed. M. F. Bode (Utrecht: VNU Science Press), p. 203
- Porter, J. M., O'Brien, T. J., & Bode, M. F. 1998, *MNRAS*, 296, 943
- Press, W. H., Teukolsky, S. A., Vetterling, W. T., & Flannery, B. P. 1992, *Numerical recipes in C. The art of scientific computing* (Cambridge University Press)

- Ragan, E., Brozek, T., Suchomska, K., Skalbania, A., Konorski, P., Galan, C., Swierczynski, E., Tomov, T., Mikolajewski, M., & Wychudzki, P. 2009, *The Astronomer's Telegram*, 2327
- Ribeiro, V. A. R. M., Bode, M. F., Darnley, M. J., Harman, D. J., Newsam, A. M., O'Brien, T. J., Bohigas, J., Echevarría, J. M., Bond, H. E., Chavushyan, V. H., Costero, R., Coziol, R., Evans, A., Eyres, S. P. S., León-Tavares, J., Richer, M. G., Tovmassian, G., Starrfield, S., & Zharikov, S. V. 2009, *ApJ*, 703, 1955
- Ribeiro, V. A. R. M., Darnley, M. J., Bode, M. F., Munari, U., Harman, D. J., Steele, I. A., & Meaburn, J. 2010, arXiv 1011.2045
- Richardson, W. H. 1972, *Journal of the Optical Society of America (1917-1983)*, 62, 55
- Rosino, L. 1987, in *RS Ophiuchi (1985) and the Recurrent Nova Phenomenon*, ed. M. F. Bode (Utrecht: VNU Science Press), p. 1
- Rosino, L. & Iijima, T. 1987, in *RS Ophiuchi (1985) and the Recurrent Nova Phenomenon*, ed. M. F. Bode (Utrecht: VNU Science Press), p. 27
- Rudy, R. J., Prater, T. R., Russell, R. W., Puetter, R. C., & Perry, R. B. 2009, *Central Bureau Electronic Telegrams*, 2055
- Rupen, M. P., Mioduszewski, A. J., & Sokoloski, J. L. 2008, *ApJ*, 688, 559
- Schaefer, B. E. 2004, *IAU Circ.*, 8396
- . 2010, *ApJS*, 187, 275
- Schaefer, B. E., Pagnotta, A., Xiao, L., Darnley, M. J., Bode, M. F., Harris, B. G., Dvorak, S., Menke, J., Linnolt, M., Templeton, M., Henden, A. A., Pojmański, G., Pilecki, B., Szczygieł, D. M., & Watanabe, Y. 2010, *AJ*, 140, 925
- Schaefer, B. E. & Ringwald, F. A. 1995, *ApJL*, 447, L45

- Schwarz, G. J., Osborne, J. P., Page, K., Beardmore, A., Walter, F., Ness, J., Mukai, K., Bode, M. F., Darnley, M. J., Kuulkers, E., Saxton, R. D., Starrfield, S., Drake, J., Takei, D., Balman, S., O'Brien, T., Wagner, R. M., & Orío, M. 2009, *The Astronomer's Telegram*, 2173
- Schwarz, G. J., Shore, S. N., Starrfield, S., & Vanlandingham, K. M. 2007, *ApJ*, 657, 453
- Shore, S. N., Kenyon, S. J., Starrfield, S., & Sonneborn, G. 1996, *ApJ*, 456, 717
- Shore, S. N., Sonneborn, G., Starrfield, S. G., Hamuy, M., Williams, R. E., Cassatella, A., & Drechsel, H. 1991, *ApJ*, 370, 193
- Skopal, A., Pribulla, T., Buil, C., Vittone, A., & Errico, L. 2008, in *Astronomical Society of the Pacific Conference Series*, Vol. 401, *Astronomical Society of the Pacific Conference Series*, ed. A. Evans, M. F. Bode, T. J. O'Brien, & M. J. Darnley, 227
- Slavin, A. J., O'Brien, T. J., & Dunlop, J. S. 1995, *MNRAS*, 276, 353
- Sokoloski, J. L., Rupen, M. P., & Mioduszewski, A. J. 2008, *ApJL*, 685, L137
- Solf, J. 1983, *ApJ*, 273, 647
- Starrfield, S., Iliadis, C., & Hix, W. R. 2008, in *Classical Novae*, 2nd Edition, ed. M. F. Bode & A. Evans (Cambridge University Press), p. 77
- Starrfield, S., Sparks, W. M., & Truran, J. W. 1985, *ApJ*, 291, 136
- Steele, I. A., Smith, R. J., Rees, P. C., Baker, I. P., Bates, S. D., Bode, M. F., Bowman, M. K., Carter, D., Etherton, J., Ford, M. J., Fraser, S. N., Gomboc, A., Lett, R. D. J., Mansfield, A. G., Marchant, J. M., Medrano-Cerda, G. A., Mottram, C. J., Raback, D., Scott, A. B., Tomlinson, M. D., & Zamanov, R. 2004, in *Society of Photo-Optical Instrumentation Engineers (SPIE) Conference Series*, Vol. 5489, *Society of Photo-Optical Instrumentation Engineers (SPIE) Conference Series*, ed. J. M. Oschmann Jr., 679

- Steffen, W., Koning, N., Wenger, S., Morisset, C., & Magnor, M. 2010, arXiv 1003.2012
- Steffen, W. & López, J. A. 2006, *Revista Mexicana de Astronomia y Astrofisica*, 42, 99
- Taylor, A. R., Davis, R. J., Porcas, R. W., & Bode, M. F. 1989, *MNRAS*, 237, 81
- Vaytet, N. M. H., O'Brien, T. J., Page, K. L., Bode, M. F., Lloyd, M., & Beardmore, A. P. 2010, *ApJ*, submitted
- Vaytet, N. M. H., O'Brien, T. J., & Rushton, A. P. 2007, *MNRAS*, 380, 175
- Walker, M. F. 1954, *PASP*, 66, 230
- Wallerstein, G. 1958, *PASP*, 70, 537
- Warner, B. 1987, *MNRAS*, 227, 23
- . 1995a, *Cataclysmic variable stars* (Cambridge University Press)
- . 1995b, *Ap&SS*, 232, 89
- Warner, B. 2008, in *Classical Novae*, 2nd Edition, ed. M. F. Bode & A. Evans (Cambridge University Press), p. 16
- Williams, R. E. 1990, in *Lecture Notes in Physics*, Berlin Springer Verlag, Vol. 369, IAU Colloq. 122: *Physics of Classical Novae*, ed. A. Cassatella & R. Viotti, 215
- Williams, R. E. 1992, *AJ*, 104, 725
- Williams, R. E., Hamuy, M., Phillips, M. M., Heathcote, S. R., Wells, L., & Navarrete, M. 1991, *ApJ*, 376, 721
- Woudt, P. A., Steeghs, D., Karovska, M., Warner, B., Groot, P. J., Nelemans, G., Roelofs, G. H. A., Marsh, T. R., Nagayama, T., Smits, D. P., & O'Brien, T. 2009, *ApJ*, 706, 738

Wu, N. 1993, *News. STScI's Image Restoration Proj.*, 1, 72

Yaron, O., Prialnik, D., Shara, M. M., & Kovetz, A. 2005, *ApJ*, 623, 398

Young, P. J., Corwin, Jr., H. G., Bryan, J., & de Vaucouleurs, G. 1976, *ApJ*, 209, 882

Zhang, E., Robinson, E. L., Stiening, R. F., & Horne, K. 1995, *ApJ*, 454, 447